Data-Driven Model-Free Electromagnetic Simulation

Zur Erlangung des akademischen Grades Doktor-Ingenieur (Dr.-Ing.)
Genehmigte Dissertation von Armin Herbert Galetzka aus Erlenbach am Main
Tag der Einreichung: June 13, 2023, Tag der Prüfung: November 10, 2023

1. Gutachten: Prof. Dr.-Ing. Herbert De Gersem
2. Gutachten: Prof. Dr.-Ing. Ulrich Römer
Darmstadt, Technische Universität Darmstadt

TECHNISCHE UNIVERSITÄT DARMSTADT

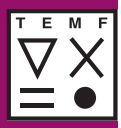

Electrical Engineering and Information Technology Department

Institute for Accelerator Science and Electromagnetic Fields (TEMF)

Electromagnetic Field Theory

Data-Driven Model-Free Electromagnetic Simulation

Accepted doctoral thesis by Armin Herbert Galetzka

Date of submission: June 13, 2023
Date of thesis defense: November 10, 2023

Darmstadt, Technische Universität Darmstadt

Bitte zitieren Sie dieses Dokument als:
URN: urn:nbn:de:tuda-tuprints-275325
URL: https://tuprints.ulb.tu-darmstadt.de/27532
Jahr der Veröffentlichung auf TUprints: 2024

Dieses Dokument wird bereitgestellt von tuprints,
E-Publishing-Service der TU Darmstadt
https://tuprints.ulb.tu-darmstadt.de
tuprints@ulb.tu-darmstadt.de

Erklärungen laut Promotionsordnung

§ 8 Abs. 1 lit. d PromO

Ich versichere hiermit, dass zu einem vorherigen Zeitpunkt noch keine Promotion versucht wurde. In diesem Fall sind nähere Angaben über Zeitpunkt, Hochschule, Dissertationsthema und Ergebnis dieses Versuchs mitzuteilen.

§ 9 Abs. 1 PromO

Ich versichere hiermit, dass die vorliegende Dissertation – abgesehen von den in ihr ausdrücklich genannten Hilfen – selbstständig verfasst wurde und dass die „Grundsätze zur Sicherung guter wissenschaftlicher Praxis an der Technischen Universität Darmstadt“ und die „Leitlinien zum Umgang mit digitalen Forschungsdaten an der TU Darmstadt“ in den jeweils aktuellen Versionen bei der Verfassung der Dissertation beachtet wurden.

§ 9 Abs. 2 PromO

Die Arbeit hat bisher noch nicht zu Prüfungszwecken gedient.

Darmstadt, June 13, 2023

Armin Herbert Galetzka

Zusammenfassung

Gegenstand der vorliegenden Arbeit ist die Simulation von magnetostatischen Feldproblemen unter ausschließlicher Verwendung gemessener Materialdaten anstelle von Materialmodellen, die aus den Daten konstruiert wurden. Die Arbeit führt ein datengetriebenes Framework für Feldprobleme ein und passt dessen Formulierung auf den Fall der Magnetostatik an. Das datengetriebene Feldproblem wird mithilfe der Euler-Lagrange-Gleichungen in kontinuierlicher Form hergeleitet und anschließend mit der Finite-Elemente-Methode gelöst. Ein hybrider Lösungsansatz wird vorgestellt, der es erlaubt Feldprobleme zu lösen, die sowohl Gebiete umfassen, in denen das Material lediglich durch Daten beschrieben ist, als auch Gebiete mit bekannter Materialbeziehung. Adaptiv angepasste Gewichtungsfaktoren werden eingeführt, um die Norm im Materialphasenraum an sich ändernde Arbeitspunkte anzupassen. Anschließend werden die Eigenschaften des datengetriebenen Problems sowie die Rechenkomplexität des Lösers diskutiert. Die Ergebnisse werden anhand mehrerer numerischer Experimente veranschaulicht, die sowohl akademische als auch realitätsnahe Probleme umfassen. Darüber hinaus wird ein numerisches Beispiel diskutiert, welches ausschließlich reale Messdaten verwendet.

Abstract

This work addresses the simulation of magnetostatic field problems using measured material data exclusively, rather than using material models constructed from the data. The work introduces a data-driven computing framework for field problems and adapts its formulation to the case of magnetostatics. The data-driven field problem is developed in continuous form utilizing the Euler-Lagrange equations and subsequently solved with the finite element method. A hybrid solver is introduced to handle magnetostatic problems that involve domains with known material relations in combination with domains where solely data are available. Adaptively adjusted weighting factors are introduced to adapt the norm in the material phase space to changing operating points. The properties of the data-driven problem and the computational complexity of the solver are discussed. The findings are illustrated with several numerical experiments covering both academic and real-world problems, including an example that is solved with real-world measurement data only.

Contents

1 Introduction

This introductory chapter gives general information about the presented work. Section 1.1 discusses the motivation behind the work's topic, while Section 1.2 provides an overview of related works within this topic. The specific contributions of the work in this research field are highlighted in Section 1.3. The chapter concludes with an outline of the work in Section 1.4.

1.1 Motivation

The modeling and simulation of electromagnetic field problems using advanced computer-aided design (CAD) tools are essential and integral to the design process for electrical devices. Over the past decades, limitations in terms of computational power and memory availability in computers have been continuously overcome, enabling accurate simulation of complex problems - a trend that is ongoing uninterruptedly [24]. The improvements, however, are not limited to hardware alone. Numerical methods for solving engineering problems are also becoming increasingly sophisticated while simultaneously reducing the computational demand. In the context of this work, we are considering the finite element (FE) method, which has become the method of choice in many disciplines [81]. However, in the development and improvement of electrical devices, this is only one part of the story. To improve and tailor electrical devices to customer specifications, enhanced or new materials with specific properties are in demand. For instance, magnetic materials, such as electrical steel, also referred to as silicon steel, are widely used in the cores of electrical devices such as inductors, motors or transformers. This material has been constantly improved and further developed over the past 70 years [121]. Thus, novel and updated descriptions of the material behavior must be found and introduced in the FE field simulation.

Computers and numerical methods constantly improve

Tailored materials for specialized electrical devices

In this work, we deal with the problem of solving partial differential equations (PDEs) arising from boundary value problems (BVPs). The class of BVPs that we are addressing encompasses a set of equations which can be classified into physical laws and constitutive equations. The physical laws comprise a compatibility law and an equilibrium law, which

are of topological nature and are derived from first principles, thus are accepted to be exactly known [76]. In the literature, these laws are also referred to as universal laws, as they are valid in any situation and are independent of the material [111]. On the other hand, constitutive equations encode the material properties and establish the link between the field quantities of the BVP. Unlike the physical laws, constitutive equations are built upon experimental data, giving them an empirical origin and classifying them as phenomenological models [111]. Moreover, constitutive equations must be continuously adjusted and enhanced to suit new materials and to account for new experimental data.

Physical laws are exactly known

To construct constitutive equations from experimental data, assumption must be made about the true underlying material response, which remains unknown. Therefore, biases, uncontrolled modeling errors, and epistemic uncertainties are inevitably introduced. The uncertainties arise among other sources, for instance, from simplification (e.g., dimension reduction), numerical approximation (e.g., polynomial truncation), and subjectivity (e.g., lack of knowledge or model preference) [117]. Moreover, once a modeling assumption has been made, fitting techniques are utilized to determine the model parameters. This is, for instance, done with regression algorithms, which can become sophisticated and cumbersome, especially when accounting for uncertainties related to finite measurement precision [100, 9] or when high-dimensional constitutive equations are considered [51, 46]. Moreover, the constitutive equation additionally needs to guarantee a certain level of (physical) compatibility, such as numerical differentiability or monotonicity when integrated into a field solver [93]. Finally, the aforementioned points are further reinforced when considering multi-physics constitutive equations.

Constitutive eqs. are empirically known

The material behavior can also be obtained through ab initio techniques, which originate from solid-state physics [52]. Ab initio techniques, in their most fundamental form, are based on first principles and consequently do not rely on fitting techniques, nor on experimental data. Instead, they directly solve the fundamental equation of the considered problem. However, even though some of the methods are exact in principle, approximations and assumptions are necessary to keep the computational demand at a manageable level [113]. In the case of ferromagnetic materials, the Landau-Lifschitz-Gilbert equation is commonly solved [114]. However, ab initio methods provide only models on a microscopic scale, limiting the size of the considered domains to reduce computational costs [108]. This makes them impracticable for engineering tasks where entire devices are simulated. A potential solution is offered through the utilization of multi-scale models, where microscopic and macroscopic constitutive equations are combined. This is particularly interesting when considering multi-physics phenomena such as magnetostriction, respectively, magneto-elasticity [34, 114]. However, lifting the microscopic equations to the macroscopic level involves approximations and assumptions, leading to a similar bottleneck as in the case of directly modeling macroscopic models

from experimental data.

BVPs involving complicated domains cannot be solved directly. Hence, numerical approximations must be introduced. The FE method allows to easily discretize the physical laws. Thereby, errors due to the discretization can be quantified with a priori, respectively a posteriori estimators [1, 21]. However, as stated in [32], "*the quality of the simulation is linked to the quality of the material description*". The quality of the constitutive equations refers to how closely the modeled equations match the true material response. This directly impacts the accuracy of the solution. In this context, George Box's famous quote "*all models are wrong*" [18] serves as a reminder that models are simply approximations of reality and are inherently limited. Moreover, the accuracy of the constitutive equations is fixed, unlike the approximation accuracy of the topological equations, which is directly linked to the numerical scheme and can be improved by refining the spatial and/or time scales. However, at a certain point, further refinement of the discretization may not improve the actual solution accuracy, as the overall error may be dominated by the error of the constitutive equation.

Quality of solution linked to constitutive eq.

Within the FE method, discrete spaces that conform with the physical laws, are introduced. Nonetheless, on the discrete level, only two of the three equations characterizing the BVP can be approximated conformally [14]. This gives the engineer the choice which equations should be fulfilled exactly. Historically seen, solutions were first calculated with the so-called primal approach or dual approach [94]. In the primal approach, the compatibility law and the constitutive equation are fulfilled exactly and the approximation error is shifted to the equilibrium law, whereas in the dual approach the equilibrium law and constitutive equation are fulfilled exactly and the approximation error is shifted to the compatibility law. Bearing in mind that the constitutive equation is in any case victim of uncertainties and errors, it seems to be natural to solve the topological equations exactly and to shift the approximation error entirely into the constitutive equation. To the knowledge of the author, this was first proposed in [104] in the field of magnetostatics and called the "error based energy approach". In this context, both Maxwell equations for magnetostatics as well as continuity and boundary conditions are enforced. The minimization then takes place in the constitutive equation. The idea was further pursued in [22] in terms of a mixed FE formulation. A similar approach was proposed in computational mechanics under the term "error in constitutive relation", see e.g., [77, 28].

Shifting the FE approx. error to constitutive eq.

Nowadays, the availability of data is steadily increasing and for many materials, the amount of behavioral data is at an unprecedentedly high level. This raises the opportunity for data-driven modeling and data-driven simulation methods. In this context, the field of computational mechanics has recently introduced a new approach called "data-driven computing" [69]. This approach presents an alternative and distinct paradigm for integrating material relations into numerical computations. Instead of relying on phenomenological

Data-driven model-free computing: avoid modeling errors

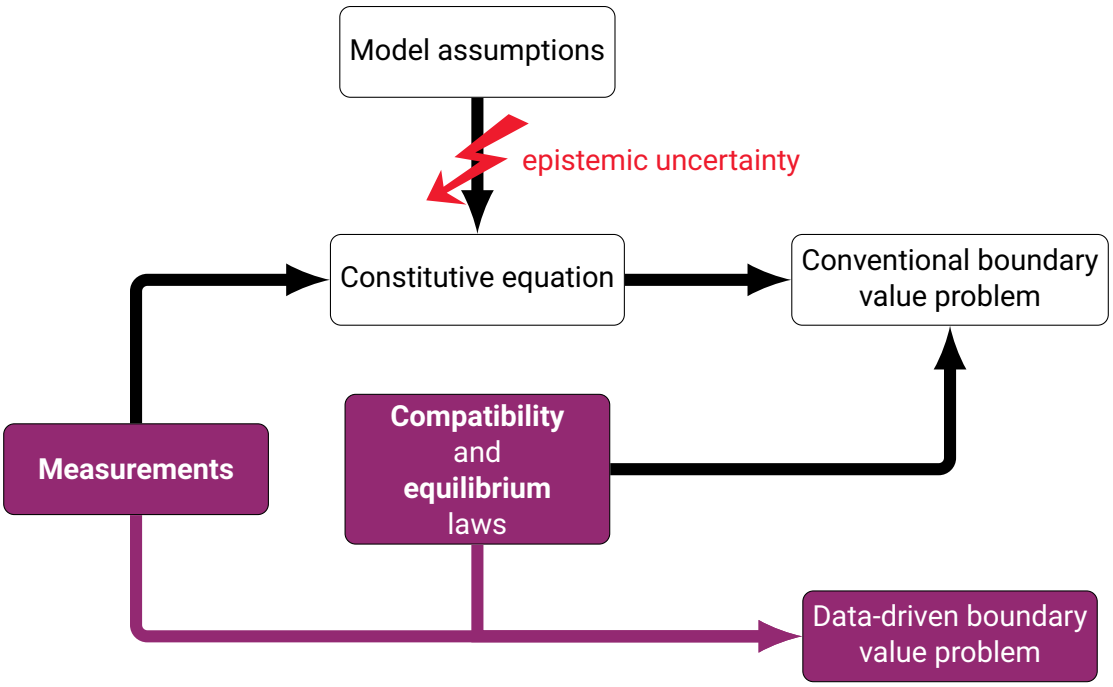

Figure 1.1: “Ingredients” for the conventional and the data-driven boundary value problem.

models, the data-driven solver embeds the measurement data directly into the solver, bypassing the material modeling step altogether. This eliminates the associated epistemic uncertainty and modeling errors. Within this framework, the numerical solver operates directly on raw material data, without relying on a specific constitutive equation. Hence, the data-driven method treats the error associated with the constitutive equation even more stringently than the error based energy approach [104]. Specifically, the solver aims to minimize the distance between the field states in phase space that adhere to the exactly known physical laws and the field states in phase space that reflect the material relation presented solely as a set of measurement data. Obviously, the availability of measurement data is limited, which means that the data-driven solver is still subject to epistemic uncertainties resulting from the lack of information. Nonetheless, the data-driven approach eliminates the introduction of additional uncertainties that may arise from the constitutive modeling process and provides a solution free from assumptions. Furthermore, increasing the amount of measurement data naturally reduces the epistemic uncertainty in the data-driven solution. In contrast, the uncertainty in the conventional

solution most likely remains at a certain level, as the chosen model assumptions do not recover the true, hidden constitutive equation. Finally, from a practical point of view, the data-driven solver significantly reduces the workflow for field simulations as the modeling process is bypassed. This allows the engineer to directly perform simulations for new and complicated material relations right after the experimental data has been obtained. It is worth mentioning that the data-driven solver is not limited to experimental data only. Instead, it can also incorporate (old) simulated data. Figure 1.1 illustrates the differences in the formulation of the data-driven approach to the conventional approach.

Directly perform simulations with data

1.2 Related works

In this work and also in the original work [69], the term "data-driven computing" refers to performing simulation directly with experimental material data. It is therefore a constitutive and material model-free approach. This demarcates the approach from other data-driven approaches, which are often associated to the field of data science. In those cases, experimental data are employed to either identify parameters or enhance the solution, without the goal to explicitly replace the constitutive equation.

Examples of works closely related to [69], but not explicitly avoiding constitutive equations, can be found in [58, 57], where manifold learning techniques are used to identify the material response locally. Global manifold learning was proposed in [67] based on kernel regression. Furthermore, constitutive equations have been successfully corrected with experimental data in [59].

The data-driven computing framework has been successfully applied to several fields in engineering, including linear and nonlinear elasticity [69, 89], finite strain elasticity [97], dynamics [71], inelasticity [41], fracture mechanics [25], poroelasticity [7], viscoelasticity in the frequency domain [106], thin composite materials [8], and multiphysics [82]. This list is not meant to be exhaustive.

A rigorous mathematical analysis has been carried out in [30, 31] and provides the conditions under which the data-driven solution converges to the conventional solution by means of the size of the data set. In particular, these works generalize BVPs, treating the conventional approaches, i.e., when the constitutive equation is considered, as a special case. It was found that the conventional solution is recovered when the experimental data set follows locally a graph. The convergence analysis with respect to the mesh size and the size of the data set has been investigated in [85].

The authors of the seminal paper [69] extended the distance-minimizing framework also to the very important case of noisy measurement data [70]. There, the distance-minimization scheme has been modified such that the data are first organized in clusters

based on the maximum entropy principle. Subsequently, the solver minimizes the free energy in the phase space. A prior-free data-driven inference approach was presented in the works [29, 98]. Here, the phase spaces associated with the two fields of the BVP are equipped with likelihood measures. Subsequently, a likelihood of the system outcome is obtained by the inference. In particular, this approach allows the incorporation of aleatory uncertainty. Another heuristic approach that robustly handles outliers was proposed in [65].

The concept of data-driven computing has been further expanded to the identification of material response, wherein the data-driven solver is effectively "inverted" to locate states that represent the mechanical response of elastic materials [78]. A data-driven solver which incorporates the material response identification approach, has been developed and has demonstrated notable improvements in accuracy and efficiency [110]. Further improvements to lower the computational demand of the method have been proposed in [42], where approximate nearest neighbor algorithms and efficient data structures have been employed to accelerate the search algorithm. Additional enhancements in the computational efficiency have been achieved in [43] through tensor voting. A multi-level method was introduced in [74], where hierarchical data sets are utilized to reduce the computational demand of the nearest neighbor problem. An approach that handles materials with regimes featuring a linear and nonlinear response has been proposed in [118]. The approach switches locally from a conventional solver with a linear constitutive equation to a data-driven solver if a certain threshold to the nonlinear part is triggered. A mixed-integer quadratic programming formulation has been suggested in [66] to globally solve the data-driven problem.

This summary was only a glimpse of the works that have been published since the original work [69]. The field of data-driven computing is constantly evolving, and there is still a large potential for further research in this area.

1.3 Contribution

The aim of the present work is a first application of the data-driven computing techniques in the field of magnetostatic field simulation. The challenges encountered in this area have led to several contributions to the field of data-driven computing. The main contributions of this work are:

- The development of a hybrid data-driven solver in which known constitutive equations and solely measurement data coexist. We proposed three different approaches to address this problem, which have been published in [36].

- The derivation of the data-driven problem in a strong, respectively continuous formulation has been presented in [47]. This formulation offers a fresh perspective and provides valuable insights into the problem. It is distinct from the data-driven variational formulation derived in [90].
- The introduction of adaptively adjusted weighting factors within the norm of the considered phase space has been published in [47]. This approach allows for the handling of strongly nonlinear material responses and leads to faster convergence rates, a higher solution accuracy, and less statistical dispersion.
- A case study for a computational demanding three-dimensional model of a DC-current electromagnet, considering real-world measurement data, has been presented in [48].
- The implementation, verification and validation of the data-driven computing framework for electromagnetic field problems into the python FE method library PYRIT [23].

1.4 Outline

The remaining of this work is structured as follows. In Chapter 2, the magnetostatic field problem and the solution strategy are presented for the conventional case, i.e., with constitutive equation, and for the data-driven case, i.e., solely using measurement data. Both formulations are derived in the continuous form. Subsequently, in Chapter 3, the numerical scheme for the discretization of the magnetostatic problem is introduced. The hybrid data-driven solver and its various formulations are discussed in Chapter 4, followed by Chapter 5 where the adaptively adjusted weighting factors are motivated and introduced. In Chapter 6, the computational complexity of the data-driven solver is analyzed and main contributors are identified. General properties of the data-driven formulation are briefly discussed in Chapter 7. Chapter 8 presents numerical results for the introduced improvements of the method, computed on a two-dimensional quadrupole magnet and a three-dimensional DC-current electromagnet. The work concludes with Chapter **??**, where our findings are summarized, and an outlook for further research in the addressed field is given.

2 Magnetostatic field problems

In the subsequent section, we consider electromagnetic (EM) field problems where the magnetic energy dominates. Consequently, wave propagation can be neglected. Following this assumption, the magneto(quasi)-static problem can be described by a reduced set of Maxwell's equations. Furthermore, considering only material that is non-conductive and assuming that temporal changes occur slowly, the magnetostatic approximation of Maxwell's equations is appropriate. The remaining equations are the static approximation of Ampère's law and Gauss's law for magnetism, which respectively read

$$\mathbf{curl}\,\mathbf{H} = \mathbf{J}, \qquad \text{in } \Omega, \tag{2.1a}$$
$$\operatorname{div}\mathbf{B} = 0, \qquad \text{in } \Omega, \tag{2.1b}$$
$$\mathbf{B}\cdot\mathbf{n} = g, \qquad \text{on } \Gamma_{\mathrm{D}}, \tag{2.1c}$$
$$\mathbf{H}\times\mathbf{n} = \mathbf{f}, \qquad \text{on } \Gamma_{\mathrm{N}}. \tag{2.1d}$$

Herein, Ω denotes the considered bounded computational domain, $\mathbf{H}$ the magnetic field strength, $\mathbf{B}$ the magnetic flux density, $\mathbf{n}$ the exterior unit normal, Γ_{D} the Dirichlet boundary with imposed flux density g, Γ_{N} the Neumann boundary with imposed surface current density $\mathbf{f}$ and $\mathbf{J}$ the source current density which has compact support on Ω_{J}, see Figure 2.1. Throughout this work, we assume that Ω is a simply connected domain with Lipschitz continuous boundary $\partial\Omega$. Furthermore, the boundary of the computational domain is decomposed such that $\partial\Omega = \Gamma = \overline{\Gamma_{\mathrm{D}}} \cup \overline{\Gamma_{\mathrm{N}}}$, where $\Gamma_{\mathrm{D}} \cap \Gamma_{\mathrm{N}} = \emptyset$. In the context of magnetostatics, the compatibility law can thus be identified with Gauss's law (2.1b), whereas Ampère's law (2.1a) defines the equilibrium law [95]. However, the problem cannot be fully resolved until the relation between the magnetic field strength $\mathbf{H}$ and the magnetic flux density $\mathbf{B}$ is characterized. In the conventional approach, this is done by introducing a constitutive equation. The constitutive equation, also referred to as material law[1], establishes the relation between $\mathbf{H}$ and $\mathbf{B}$. Typically, both fields are connected through the magnetic permeability tensor $\boldsymbol{\mu}$, respectively, the reluctivity tensor $\boldsymbol{\nu} = \boldsymbol{\mu}^{-1}$, in the

[1] We avoid the term *law* in this work, as the material relation is only available as a phenomenological model and not derived from first principle.

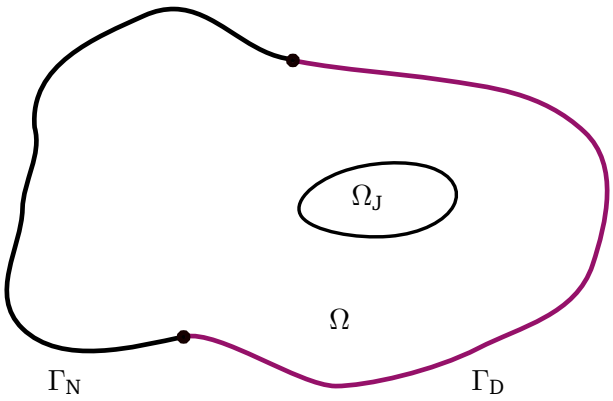

Figure 2.1: Illustration of the computational domain for the magnetostatic problem.

form $\mathbf{B} = \boldsymbol{\mu}(\mathbf{H})\mathbf{H}$. As discussed in Section 1, Maxwell's equations are derived from first principles and thus considered to be exactly known. In contrast, the constitutive equation for the permeability $\boldsymbol{\mu}$ is only empirically known and is subject to uncertainties, model assumptions, and modeling errors. Although some materials, such as the permeability of free space, are accepted to be known with a certain degree of accuracy, the lack of precise and trustworthy material models is particularly evident for novel and complex materials, such as strongly nonlinear soft-magnetic materials. The data-driven solver offers an alternative approach by completely bypassing the modeling process, thereby eliminating the need for a constitutive equation. Additionally, this approach avoids introducing modeling errors and uncertainties, and reduces the simulation workflow as there is no need to deduce the underlying (hidden) constitutive equations. Instead, the simulation can be carried out directly, utilizing the available measurement data.

The remaining of this chapter is dedicated to the data-driven formulation for magnetostatics. Therefore, we first recall the conventional problem formulation, followed by the derivation of the data-driven counterpart.

2.1 Conventional magnetostatic problem formulation

In the conventional approach, the set of equations (2.1) has to be supplemented by the material constitutive relation

$$\mathbf{B} = \boldsymbol{\mu}(\mathbf{x}, \mathbf{H})\mathbf{H}, \tag{2.2a}$$

$$\mathbf{H} = \boldsymbol{\nu}(\mathbf{x}, \mathbf{B})\mathbf{B}, \tag{2.2b}$$

where the permeability and its inverse, the reluctivity, are now spatial and field dependent. The characteristic property of the material is thus encoded in the permeability tensor. For materials with a linear response, the constitutive equation is of the form $\mathbf{B} = \mu_0\mu_\mathrm{r}\mathbf{H}$, where μ_r refers to the relative permeability and μ_0 to the permeability of free space, resulting in aligned fields $\mathbf{B}$ and $\mathbf{H}$ inside the material. This does not necessarily hold for the fields inside magnetic materials [37]. In addition to linear materials, we also consider nonlinear ferromagnetic materials in this work. Hereby, we neglect temperature dependency and hysteresis, i.e., we consider the initial magnetization curve without any remanent magnetization. Ferromagnetic materials, such as electrical steel, exhibit a strongly nonlinear and additionally anisotropic behavior. Thereby, the field quantities $\mathbf{B}$ and $\mathbf{H}$ are aligned along the rolling direction and its transversal [109], which are called the principle axes. Thus, in this principle coordinate system, the permeability tensor $\boldsymbol{\mu}$ of a ferromagnetic material contains only entries on the diagonal [107]. In the case that the global coordinate system does not coincide with the principle axes, the permeability tensor can be transformed with rotation operators [91]. Similarly, the global coordinate system can be locally rotated such that the rotated coordinate system and the principle axes of the material align. Then, a diagonal tensor can be obtained and the field components of $\mathbf{H}$ and $\mathbf{B}$ are decoupled. Throughout this work, we assume that the principle coordinate system is aligned with the global coordinate system. The permeability tensor then reads

$$\boldsymbol{\mu}(\mathbf{x}, H) = \begin{bmatrix} \mu_x(\mathbf{x}, H_x) & 0 & 0 \\ 0 & \mu_y(\mathbf{x}, H_y) & 0 \\ 0 & 0 & \mu_z(\mathbf{x}, H_z) \end{bmatrix}. \tag{2.3}$$

The material models $\boldsymbol{\mu}(\mathbf{H})$ and $\boldsymbol{\nu}(\mathbf{B})$ themselves are constructed along the available measurement data. However, considering the physical background, the models have to fulfill certain criteria, see e.g., [101]. Significant effort has been spent in the physically correct modeling of BH-curves over the past decades. Various methods have been proposed, including monotonic spline interpolation of noise-free data [54], monotonicity-preserving approximation with smoothing splines [93], closed-form models where the coefficients are

determined through regression techniques [20, 120, 56], and sophisticated machine learning algorithms [115, 72]. Stochastic modeling of BH-curves has also been investigated, for instance in [61, 99]. It should be noted that this list is not exhaustive.

To solve the magnetostatic problem, we introduce the vector potential $\mathbf{A}$, such that $\mathbf{B} = \mathbf{curl}\,\mathbf{A}$. By that, the divergence-free property, also known as solenoidal property, of the magnetic flux density is guaranteed by construction. Now, starting from (2.1a), we obtain

$$\mathbf{curl}\left(\boldsymbol{\nu}(\mathbf{x}, \mathbf{curl}\,\mathbf{A})\mathbf{curl}\,\mathbf{A}\right)) = \mathbf{J}, \qquad \text{in } \Omega, \tag{2.4a}$$

$$\mathbf{curl}\,\mathbf{A} \cdot \mathbf{n} = g, \qquad \text{on } \Gamma_{\mathrm{D}}, \tag{2.4b}$$

$$\boldsymbol{\nu}(\mathbf{x}, \mathbf{curl}\,\mathbf{A})\mathbf{curl}\,\mathbf{A} \times \mathbf{n} = \mathbf{f}, \qquad \text{on } \Gamma_{\mathrm{N}}. \tag{2.4c}$$

Note that the solution to (2.4) is not yet unique as an arbitrary gradient field can be added to $\mathbf{A}$ without having an effect on $\mathbf{B}$. To ensure uniqueness, a gauging condition in the vector potential is necessary, which we will address in a later stage of this work. The set of equations (2.4) constitutes an elliptic BVP.

2.2 Data-driven magnetostatic problem formulation

Section 2.1 showed that the constitutive equation is an essential ingredient to solve the BVP. In the following section, we present an alternative approach to (2.4) that does not rely on constitutive equations and instead works directly with the measurement data. The method is illustrated in Section 2.2.1 on a one-dimensional problem and is afterwards generalized for magnetostatic problems in Section 2.2.2.

2.2.1 Introductory example

The following is mainly based on [47]. To illustrate the data-driven framework, we start with an academic example. Figure 2.2a depicts a C-shaped iron yoke with an air gap. The magnetic flux Φ is excited by the current I which flows through a coil with N_{coil} turns. We assume that there are no fringe fields at the outside of the iron core and that the magnetic path has a constant cross-section S_{Fe}. As a result, both the magnetic flux Φ and the magnetic flux density $\mathbf{B}$ are constant along the magnetic path. These assumptions allow us to approximate the magnetic field problem using an equivalent magnetic circuit, as shown in Figure 2.2a. Additionally, we assume that the magnetic field pairs $(\mathbf{H}_{\text{air}}, \mathbf{B})$ in the air part and $(\mathbf{H}_{\text{Fe}}, \mathbf{B})$ in the iron part are homogeneously distributed. Therefore, on a circuit level, it holds that $B = |\mathbf{B}|$ and $H = |\mathbf{H}|$. The exciting current I gives rise to the

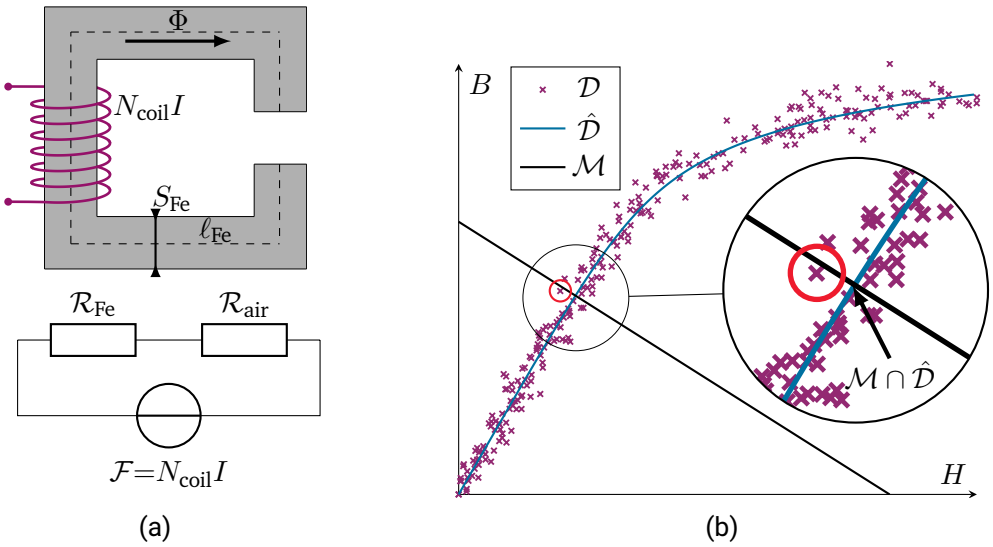

Figure 2.2: (a) C-shaped iron yoke, excited by the current flowing through a coil. The equivalent magnetic circuit is shown below. (b) HB phase space with the constraint set $\mathcal{M}$ containing all states that fulfill the circuit law (black line). The blue line shows the material model. The conventional solution is found at the intersection of both lines. The measurement data are shown by the crosses. The data-driven solution is defined by the state in the measurement data that is closest to $\mathcal{M}$ (red circle).

magnetomotive force $\mathcal{F}$ which is given as

$$\mathcal{F} = \oint \mathbf{H} \cdot \mathrm{d}\mathbf{s} = N_{\text{coil}} I = \mathcal{F}_{\text{Fe}} + \mathcal{F}_{\text{air}}, \tag{2.5}$$

where $\mathcal{F}_{\text{Fe}}$, respectively $\mathcal{F}_{\text{air}}$ denote the magnetomotive forces in the iron yoke and in the air gap. Taking the assumptions into account, $\Phi = BS_{\text{Fe}}$ and hence

$$\Phi = \frac{\mathcal{F}}{\mathcal{R}_{\text{Fe}} + \mathcal{R}_{\text{air}}} = \frac{\mathcal{F}_{\text{air}}}{\mathcal{R}_{\text{air}}} = \frac{\mathcal{F}_{\text{Fe}}}{\mathcal{R}_{\text{Fe}}}, \tag{2.6}$$

with $\mathcal{R}_{\text{air}}$ and $\mathcal{R}_{\text{Fe}}$ being the reluctances of the iron yoke and the air gap, respectively. Furthermore, let ℓ_{Fe} denote the average length in the iron yoke (see dashed line in Figure 2.2a) and H_{Fe} the unknown magnetic field strength in the iron yoke. Then,

combining equations (2.5) and (2.6) yields

$$BS_{\text{Fe}} = -\frac{H_{\text{Fe}}\ell_{\text{Fe}}}{\mathcal{R}_{\text{air}}} + \frac{N_{\text{coil}}I}{\mathcal{R}_{\text{air}}}. \tag{2.7}$$

Note that (2.7) is known up to the field state (H_{Fe}, B). For the sake of completeness, the reluctance of the air gap is given by

$$\mathcal{R}_{\text{air}} = \frac{\ell_{\text{air}}}{\mu_0 S_{\text{Fe}}}, \tag{2.8}$$

where ℓ_{air} refers to the length of the air gap and μ_0 to the permeability in vacuum. Let $\mathcal{Z} \subset \mathbb{R} \times \mathbb{R}$ denote the space of all possible (H_{Fe}, B) pairs. Then, the constraint (2.7) gives rise to a reduced space $\mathcal{M} \subset \mathcal{Z}$, where we find all states (H_{Fe}, B) that fulfill the circuit equation (2.7), i.e.,

$$\mathcal{M} = \left\{ (H_{\text{Fe}}, B) \in \mathcal{Z} : BS_{\text{Fe}} = -\frac{H_{\text{Fe}}\ell_{\text{Fe}}}{\mathcal{R}_{\text{air}}} + \frac{N_{\text{coil}}I}{\mathcal{R}_{\text{air}}} \right\}. \tag{2.9}$$

However, the constrained set $\mathcal{M}$ contains an infinite number of solutions. To solve (2.7), additional information on the material in the iron yoke must be provided.

For a conventional solver, a material model for the iron part is necessary, which defines the material set $\hat{\mathcal{D}}$ as

$$\hat{\mathcal{D}} = \left\{ (H_{\text{Fe}}, B) \in \mathcal{Z} : B = \mu(H_{\text{Fe}}) H_{\text{Fe}} \right\}, \tag{2.10}$$

where $\mu : \mathbb{R}_0^+ \to \mathbb{R}^+$. The conventional solution is then found as the intersection of the constrained set (2.9) and the material set, i.e.,

$$(H_{\text{Fe}}, B)^\star = \mathcal{M} \cap \hat{\mathcal{D}}. \tag{2.11}$$

The solution to (2.11) can be obtained by replacing the magnetic flux density B in (2.7) with the material model given in (2.10). Thereafter, the resulting (nonlinear) equation can be solved for H_{Fe} and subsequently B is computed with the material model. The measurement set $\hat{\mathcal{D}}$ and the set of states fulfilling the circuit equation $\mathcal{M}$ are illustrated in Figure 2.2b. The intersection of circuit equation (solid black line) and the material relation (blue line) shows the conventional solution (2.11).

In the data-driven setting, a model representation as in (2.10) is not necessary. Instead, only discrete measurement data are utilized to solve the electromagnetic problem for

(H_{Fe}, B). The discrete measurement data are collected in the measurement set

$$\mathcal{D} = \{(H_{\mathrm{Fe}}, B)_i\}_{i=1}^{N}, \tag{2.12}$$

where N denotes the total amount of employed measurement data. Following (2.11), a solution is sought with the discrete measurement set (2.12). Given that only a finite amount of measurement data are available, the intersection is most likely empty, thereby necessitating a relaxation of the formulation. Therefore, we search for a state that fulfills the constraints given by the circuit equation, i.e., a state $\zeta \in \mathcal{M}$, while at the same time the state needs to be closest to a state in the measurement set $\mathcal{D}$. Accordingly, we seek the state that minimizes the distance between the circuit equation and the given data set, i.e.,

$$(H_{\mathrm{Fe}}, B)^{\star} = \underset{(H_{\mathrm{Fe}}, B) \in \mathcal{M}}{\operatorname{argmin}} \left\{ F((H_{\mathrm{Fe}}, B), \mathcal{D}) \right\}, \tag{2.13}$$

where $F((H_{\mathrm{Fe}}, B), \mathcal{D})$ is a distance function in the HB phase space that returns the smallest distance from a state (H_{Fe}, B) to the available measurement data. Figure 2.2b shows the data-driven solution highlighted by the red circle, where the discrete measurement data are represented by crosses. The relaxation in (2.13) is the core idea of the data-driven paradigm and allows to employ discrete measurement data instead of model representations for the constitutive relation.

2.2.2 Data-driven framework in continuous form

Next, we want to generalize the data-driven formulation to magnetostatic problems. Building upon the introductory example outlined in Section 2.2.1, we first define the phase space $\mathcal{M}$ that covers the equations for magnetostatics (2.1).

Before we define the set $\mathcal{M}$, we recall some standard function spaces. Let $L^2(\Omega)^3$ denote the space of real and square-integrable functions, that is,

$$L^2(\Omega)^3 = \left\{ \mathbf{u} : \|\mathbf{u}\|_{L^2(\Omega)} < \infty \right\}. \tag{2.14}$$

where $\|\mathbf{u}\|^2_{L^2(\Omega)} = (\mathbf{u}, \mathbf{u})_\Omega$ with the inner product

$$(\mathbf{u}, \mathbf{v})_\Omega = \int_\Omega \mathbf{u} \cdot \mathbf{v} \, \mathrm{d}\Omega. \tag{2.15}$$

Moreover, due to the requirement of Maxwell's equations for a space with reduced smooth-

ness properties [44, 86], we introduce the Hilbert spaces

$$\begin{aligned} \mathrm{H}(\mathbf{grad};\Omega) &= \left\{u \in L^2(\Omega) : \|\mathbf{grad}\, u\|_{L^2(\Omega)} < \infty\right\}, \\ \mathrm{H}(\mathbf{curl};\Omega) &= \left\{\mathbf{u} \in L^2(\Omega)^3 : \|\mathbf{curl}\, \mathbf{u}\|_{L^2(\Omega)} < \infty\right\}, \\ \mathrm{H}(\mathrm{div};\Omega) &= \left\{\mathbf{u} \in L^2(\Omega)^3 : \|\mathrm{div}\, \mathbf{u}\|_{L^2(\Omega)} < \infty\right\}. \end{aligned} \tag{2.16}$$

For brevity of notation, we introduce the state variable $\zeta = (\mathbf{H}, \mathbf{B})$. Then, we find states ζ fulfilling (2.1) in

$$\begin{aligned} \mathcal{M} = \{\zeta \in \mathrm{H}(\mathbf{curl};\Omega) \times \mathrm{H}(\mathrm{div};\Omega) : &\mathbf{curl}\, \mathbf{H} = \mathbf{J},\ \mathrm{div}\, \mathbf{B} = 0, \\ &\mathbf{B} \cdot \mathbf{n} = g,\ \mathbf{H} \times \mathbf{n} = \mathbf{f},\ \text{a.e. in } \Omega\}. \end{aligned} \tag{2.17}$$

Next, we need to define the measurement set $\mathcal{D}$, where we find functions $(\mathbf{H}, \mathbf{B})$ that are compatible with the measurement data. As already pointed out in Section 1, the data-driven formulation is a generalization of classical BVPs, "*since the local material data sets, even if they define a curve in phase space, need not be a graph*" [30]. In a first step, the measurement set $\mathcal{D}$ can thus be defined by a given material relation. Consequently, conditions under which the classical solution is recovered can be derived. For the case of linear elasticity, a detailed analysis has been carried out in [30], which has been further extended to finite elasticity in [31]. We therefore omit the case of describing the measurement set $\mathcal{D}$ by a given material relation and start our derivation of the magnetostatic data-driven formulation directly with discrete measurement data.

For electromagnetic problems, it is common to have a heterogeneous material distribution over the domain Ω. For instance, in the case of an inductor, the domain can be typically decomposed into three parts: an iron part, an air part, and the coil. Hence, each subdomain requires its own measurement set, which we denote by $\tilde{\mathcal{D}}_{\Omega_i}$, where i refers to the considered subdomain. Furthermore, the material may exhibit anisotropic behavior, i.e., the material behaves differently in different directions. The local measurement set per dimension is thus defined as

$$\tilde{\mathcal{D}}_{\Omega_i,r} = \left\{(h_r, b_r)_1, (h_r, b_r)_2, \ldots, (h_r, b_r)_{N_{\Omega_i,r}}\right\}, \tag{2.18}$$

where $r \in \{x, y, z\}$, $(h_r, b_r)_j \in \mathbb{R} \times \mathbb{R}$, $j = 1, \ldots, N_{\Omega_i,r}$ and $N_{\Omega_i,r}$ refers to the number of measurement points in the considered domain and spatial direction. The local measurement set containing all dimensions is obtained with the Cartesian product

$$\tilde{\mathcal{D}}_{\Omega_i} = \tilde{\mathcal{D}}_{\Omega_i,x} \times \tilde{\mathcal{D}}_{\Omega_i,y} \times \tilde{\mathcal{D}}_{\Omega_i,z}. \tag{2.19}$$

In the same manner, the global measurement set containing the discrete measurement data is defined by

$$\tilde{\mathcal{D}} = \bigtimes_i \tilde{\mathcal{D}}_{\Omega_i}. \tag{2.20}$$

The total amount of employed measurement data is thus $N = \sum_{\Omega_i} \sum_{r\in\{x,y,z\}} N_{\Omega_i,r}$. However, in order to minimize the distance between states from (2.17) and the measurement set, a spatial-dependent representation, i.e., an appropriate function space is necessary [30]. Therefore, we define the global set of material states as

$$\mathcal{D} = \left\{ \zeta \in L^2(\Omega)^3 \times L^2(\Omega)^3 : \zeta(\mathbf{x}) \in \tilde{\mathcal{D}}_{\Omega_i}, \forall \mathbf{x} \in \Omega_i, \forall i, \text{ a.e. in } \Omega \right\}. \tag{2.21}$$

Thus, evaluating a function $\zeta \in \mathcal{D}$ at a certain spatial coordinate gives access to the discrete measurement data in $\tilde{\mathcal{D}}$, i.e., $\zeta(\mathbf{x}) \in \tilde{\mathcal{D}}$.

To perform the distance-minimization in the data-driven formulation, a suitable norm in the phase space must be defined. Therefore, for $\mathbf{u}, \mathbf{v} \in L^2(\Omega)^3$, we introduce the weighted inner product

$$(\mathbf{u}, \mathbf{v})_{\Omega,\tilde{\boldsymbol{X}}} = \int_\Omega \frac{1}{2} \tilde{\boldsymbol{X}} \mathbf{u} \cdot \mathbf{v} \, \mathrm{d}\Omega, \tag{2.22}$$

with corresponding norm

$$\|\mathbf{u}\|^2_{L^2_{\tilde{\boldsymbol{X}}}(\Omega)} = (\mathbf{u}, \mathbf{u})_{\Omega,\tilde{\boldsymbol{X}}}. \tag{2.23}$$

Herein, $\tilde{\boldsymbol{X}}$ refers to the so-called weighting factor, which we will discuss in greater detail in the following. The norm in the HB phase space is then defined by

$$\|\zeta\|^2_{L^2_{\tilde{\boldsymbol{\mu}},\tilde{\boldsymbol{\nu}}}(\Omega)} = \|(\mathbf{H}, \mathbf{B})\|^2_{L^2_{\tilde{\boldsymbol{\mu}},\tilde{\boldsymbol{\nu}}}(\Omega)} := \|\mathbf{H}\|^2_{L^2_{\tilde{\boldsymbol{\mu}}}(\Omega)} + \|\mathbf{B}\|^2_{L^2_{\tilde{\boldsymbol{\nu}}}(\Omega)}, \tag{2.24}$$

where $\tilde{\boldsymbol{\mu}}$ and $\tilde{\boldsymbol{\nu}}$ are weighting factors. The tensorial and space-dependent weighting factors are of computational nature only [69], however, they share units with the permeability and the reluctivity, respectively, which explains the notation. Their choice can improve the convergence rate of the data-driven solver as we will see later. For completeness, it should be noted that other metrics, e.g., the Mahalanobis distance, can be employed as well [6]. Utilizing the norm (2.24), the distance function minimizing the distance of a state ζ to the entire measurement set $\mathcal{D}$ can be written as

$$F(\zeta, \mathcal{D}) = \inf_{\zeta^\times \in \mathcal{D}} \left\{ \left\| \zeta - \zeta^\times \right\|^2_{L^2_{\tilde{\boldsymbol{\mu}},\tilde{\boldsymbol{\nu}}}(\Omega)} \right\}, \quad \text{with } \zeta \in L^2(\Omega)^3 \times L^2(\Omega)^3. \tag{2.25}$$

Note that since the weighting factors share the same unit as the permeability, respectively

the reluctivity, the distance function returns the minimum magnetic energy mismatch between a state and the available measurement data. This implies that the data-driven solver seeks the state that minimizes the energy difference between states that conform with the equations for magnetostatics to states that describe the material response. Now, the data-driven minimization problem reads

$$\text{minimize } F(\zeta, \mathcal{D}), \tag{2.26a}$$

$$\text{subject to } \begin{cases} \mathbf{curl}\,\mathbf{H} &= \mathbf{J}, & \text{in } \Omega, \\ \operatorname{div}\mathbf{B} &= 0, & \text{in } \Omega, \\ \mathbf{B}\cdot\mathbf{n} &= g, & \text{on } \Gamma_{\mathrm{D}}, \\ \mathbf{H}\times\mathbf{n} &= \mathbf{f}, & \text{on } \Gamma_{\mathrm{N}}. \end{cases} \tag{2.26b}$$

The data-driven problem formulation is thus a constrained double-minimization problem and can be rewritten as

$$\zeta^\star \in \underset{\zeta\in\mathcal{M}}{\operatorname{argmin}} \left\{ \inf_{\zeta^\times\in\mathcal{D}} \left\| \zeta - \zeta^\times \right\|^2_{L^2_{\tilde{\boldsymbol{\mu}},\tilde{\boldsymbol{\nu}}}(\Omega)} \right\}, \tag{2.27}$$

if the desired solution $\zeta^\star$ should conform with the equations for magnetostatics, while being closest to the available measurement states. Note that once the data-driven problem has been discretized, it is straightforward to interchange the two sets in (2.27), i.e., to solve for a state that is in the set of measurement states, while being closest to states fulfilling the equations for magnetostatics [41]. However, in the continuous formulation, the interchanged double-minimization problem is not well-defined for arbitrary sets $\mathcal{D}$. For the rest of this work, we consider the first case.

The existence and properties of the solution to (2.27) has been extensively discussed in [30, 31]. To solve the problem numerically, the double minimization problem (2.27) is formulated as a fixed-point iteration [69, 110]. In the following, we want to derive the fixed-point iteration in a continuous manner, which will later be solved numerically with the FE method. We begin by selecting a starting point, e.g., $\zeta^\times \in \mathcal{D}$, and subsequently, we split the double minimization problem into two separate minimization problems.

1. **Projection on magnetostatic state:** The idea is to start with a randomly chosen state $\zeta^\times \in \mathcal{D}$. Subsequently, we search for a state $\zeta^\circ \in \mathcal{M}$ that is closest to $\zeta^\times$, which we denote by the closest point projection

$$\zeta^\circ = \mathcal{P}_{\mathcal{M}}\left(\zeta^\times\right). \tag{2.28}$$

   Here, we assumed that (2.28) has a unique solution. Note that this is an additional

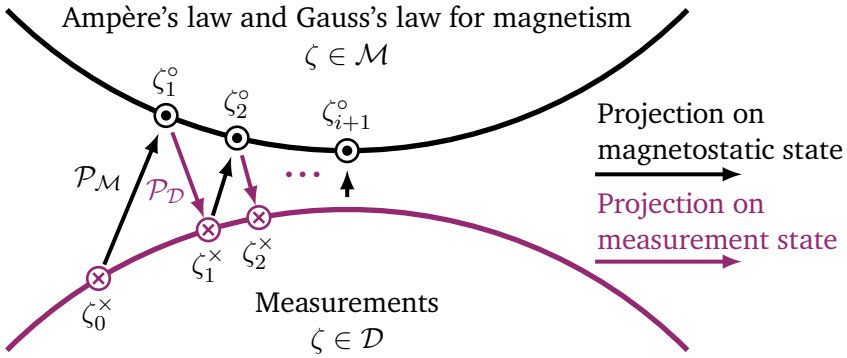

Figure 2.3: Illustration of the fixed-point iteration.

assumption, since $\mathcal{M}$ is generally not a subspace.

2. **Projection on measurement state:** Given a state $\zeta^\circ \in \mathcal{M}$, that is, a state compatible with the equations for magnetostatics, we search for a state in the measurement set that is closest to ζ°. Again, we introduce the closest point projection

$$\zeta^\times = \mathcal{P}_\mathcal{D}(\zeta^\circ). \tag{2.29}$$

Again, we assumed that (2.29) has a unique solution.

Therefore, for each data-driven iteration, two minimization problems, i.e., equation (2.28) and (2.29), must be solved. The iterative scheme can thus be defined as

$$\zeta_{i+1}^\circ = \left(\mathcal{P}_\mathcal{M} \circ \mathcal{P}_\mathcal{D}\right)\left(\zeta_i^\circ\right), \tag{2.30}$$

which follows the typical form of a fixed-point iteration. The scheme is visually illustrated in Figure 2.3. Note that it is also possible to directly solve the double-minimization problem using mixed-integer programming [66], once the problem has been discretized. The fixed-point iteration is carried out until ζ_i° remains unchanged in two consecutive iteration steps. Another criterion that can be used to assess convergence is derived from the energy mismatch between the measurement state and the state compatible with the equations for magnetostatics. The energy mismatch then reads

$$\Delta_{\mathrm{em},i} = \|\zeta_i^\circ - \zeta_i^\times\|_{L^2_{\tilde{\boldsymbol{\mu}},\tilde{\boldsymbol{\nu}}}(\Omega)}, \quad \text{with } \zeta_i^\circ \in \mathcal{M},\ \zeta_i^\times \in \mathcal{D}. \tag{2.31}$$

For a given amount of measurement data N, the data-driven solver reaches a certain energy mismatch (2.31). This energy mismatch is of course reduced if more measurement data at the desired states in the HB phase space are available. Consequently, if the energy mismatch does not significantly change between two consecutive iteration steps, convergence is reached. Introducing the user-defined constant $\delta_{\Delta_{\mathrm{em}}}$, the data-driven solver stops once $|\Delta_{\mathrm{em},i} - \Delta_{\mathrm{em},i-1}| < \delta_{\Delta_{\mathrm{em}}}$. In the following, we derive the two projection operators and provide further details on the problem structure.

Projection on magnetostatic state

Given a state $\zeta^{\times} \in \mathcal{D}$, i.e., a state from the measurement set, a new state $\zeta^{\circ} \in \mathcal{M}$ which is compatible with the equations for magnetostatics and closest to the measurement state $\zeta^{\times}$ is found by solving

$$\zeta^{\circ} \in \underset{\zeta \in \mathcal{M}}{\operatorname{argmin}} \left\| \zeta - \zeta^{\times} \right\|^2_{L^2_{\tilde{\boldsymbol{\mu}},\tilde{\boldsymbol{\nu}}}(\Omega)} . \tag{2.32}$$

Note that the minimization problem (2.32) is a constrained minimization problem as ζ belongs to the states that fulfill the equations for magnetostatics. To fulfill Gauss's law (2.1b), we employ the magnetic vector potential formulation, i.e., $\mathbf{B} = \mathbf{curl}\,\mathbf{A}$. Once again, the gauging conditions for the vector potential $\mathbf{A}$ will be postponed to the upcoming section. Additionally, the boundary conditions (BCs) (2.1c), respectively (2.1d), are disregarded and will be incorporated at a later stage. Thus, the minimization is carried out on

$$\begin{aligned} \min_{(\mathbf{H},\mathbf{A})} \mathcal{L} = \min_{(\mathbf{H},\mathbf{A})} & \left\{ \left\| \mathbf{H} - \mathbf{H}^{\times} \right\|^2_{L^2_{\tilde{\boldsymbol{\mu}}}(\Omega)} + \left\| \mathbf{curl}\,\mathbf{A} - \mathbf{B}^{\times} \right\|^2_{L^2_{\tilde{\boldsymbol{\nu}}}(\Omega)} \right\}, \\ \text{subject to :} \quad & \mathbf{curl}\,\mathbf{H} = \mathbf{J}, \\ & (\mathbf{H},\mathbf{A}) \in \mathrm{H}(\mathbf{curl};\Omega) \times \mathrm{H}(\mathbf{curl};\Omega). \end{aligned} \tag{2.33}$$

Thus, the goal is now to find functions $\mathbf{H}$ and $\mathbf{A}$ which make the functional $\mathcal{L}$ stationary while satisfying Ampère's law. This can be achieved by applying the Euler-Lagrange equations [105, 73]. However, (2.33) is subject to Ampère's law, which represents a non-integral constraint. Therefore, a Lagrange multiplier function $\boldsymbol{\eta}(\mathbf{x})$ is needed to enforce Ampère's law in the functional (2.33) [79], which yields the augmented Lagrangian

$$\begin{aligned} \mathcal{L}(\mathbf{x}, \mathbf{curl}\,\mathbf{A}, \mathbf{H}, \mathbf{curl}\,\mathbf{H}) &= \left\| \mathbf{H}(\mathbf{x}) - \mathbf{H}^{\times}(\mathbf{x}) \right\|^2_{L^2_{\tilde{\boldsymbol{\mu}}}(\Omega)} + \left\| \mathbf{curl}\,\mathbf{A}(\mathbf{x}) - \mathbf{B}^{\times}(\mathbf{x}) \right\|^2_{L^2_{\tilde{\boldsymbol{\nu}}}(\Omega)} \\ &\quad + \left(\boldsymbol{\eta}(\mathbf{x}), \mathbf{J}(\mathbf{x}) - \mathbf{curl}\,\mathbf{H}(\mathbf{x}) \right)_{\Omega}, \\ &= \int_{\Omega} \left[\mathcal{E}\left(\mathbf{x}, \mathbf{curl}\,\mathbf{A}, \mathbf{H}\right) + \boldsymbol{\eta}(\mathbf{x}) \cdot \mathcal{C}\left(\mathbf{x}, \mathbf{curl}\,\mathbf{H}\right) \right] \mathrm{d}\Omega, \end{aligned} \tag{2.34}$$

with

$$\begin{aligned}\mathcal{E}(\mathbf{x}, \mathbf{curl}\,\mathbf{A}, \mathbf{H}) &= \frac{1}{2}\tilde{\boldsymbol{\mu}}(\mathbf{H}(\mathbf{x}) - \mathbf{H}^{\times}(\mathbf{x})) \cdot (\mathbf{H}(\mathbf{x}) - \mathbf{H}^{\times}(\mathbf{x})) \\ &\quad + \frac{1}{2}\tilde{\boldsymbol{\nu}}(\mathbf{curl}\,\mathbf{A}(\mathbf{x}) - \mathbf{B}^{\times}(\mathbf{x})) \cdot (\mathbf{curl}\,\mathbf{A}(\mathbf{x}) - \mathbf{B}^{\times}(\mathbf{x})) \\ \mathcal{C}(\mathbf{x}, \mathbf{curl}\,\mathbf{H}) &= \mathbf{J}(\mathbf{x}) - \mathbf{curl}\,\mathbf{H}(\mathbf{x}).\end{aligned} \tag{2.35}$$

The Lagrange multiplier function $\boldsymbol{\eta}$ can be understood as a pseudo potential [103]. The Euler-Lagrange equation then reads

$$\frac{\partial \mathcal{L}}{\partial y} - \mathcal{D}_{\mathbf{x}}\left\{\frac{\partial \mathcal{L}}{\partial \mathcal{D}_{\mathbf{x}} y}\right\} = 0, \tag{2.36}$$

respectively,

$$\frac{\partial \mathcal{E}}{\partial y} - \mathcal{D}_{\mathbf{x}}\left\{\frac{\partial \mathcal{E}}{\partial \mathcal{D}_{\mathbf{x}} y}\right\} + \boldsymbol{\eta}(\mathbf{x})\frac{\partial \mathcal{C}}{\partial y} - \mathcal{D}_{\mathbf{x}}\left\{\boldsymbol{\eta}(\mathbf{x})\frac{\partial \mathcal{C}}{\partial \mathcal{D}_{\mathbf{x}} y}\right\} = 0, \tag{2.37}$$

where $\mathcal{D}_{\mathbf{x}}$ denotes a first-order differential operator and y refers to the unknown function that renders $\mathcal{L}$ stationary. Applying the Euler-Lagrange equations on (2.34), yields

$$\begin{aligned}\frac{\partial}{\partial \mathbf{A}}: \quad & -\mathbf{curl}\left\{\frac{\partial \mathcal{E}}{\partial \mathbf{curl}\,\mathbf{A}}\right\} = 0, \\ \Longleftrightarrow \quad & \mathbf{curl}\,(\tilde{\boldsymbol{\nu}}\mathbf{curl}\,\mathbf{A}) = \mathbf{curl}\,(\tilde{\boldsymbol{\nu}}\mathbf{B}^{\times}), && \text{(2.38a)} \\ \frac{\partial}{\partial \mathbf{H}}: \quad & \frac{\partial \mathcal{E}}{\partial \mathbf{H}} - \mathbf{curl}\left\{\boldsymbol{\eta}(\mathbf{x})\frac{\partial \mathcal{C}}{\partial \mathbf{curl}\,\mathbf{H}}\right\} = 0, \\ \Longleftrightarrow \quad & \tilde{\boldsymbol{\mu}}\mathbf{H} - \mathbf{curl}\,\boldsymbol{\eta} = \tilde{\boldsymbol{\mu}}\mathbf{H}^{\times}, && \text{(2.38b)}\end{aligned}$$

where the magnetic field strength $\mathbf{H}$ in (2.38b) can be further eliminated by applying the curl operator on (2.38b) and inserting $\mathbf{curl}\,\mathbf{H} = \mathbf{J}$, which yields the two curl-curl equations

$$\begin{aligned}\mathbf{curl}\;(\tilde{\boldsymbol{\nu}}\mathbf{curl}\,\mathbf{A}) &= \mathbf{curl}\,(\tilde{\boldsymbol{\nu}}\mathbf{B}^{\times}), \qquad \text{in } \Omega, && \text{(2.39a)} \\ \mathbf{curl}\;(\tilde{\boldsymbol{\nu}}\mathbf{curl}\,\boldsymbol{\eta}) &= \mathbf{J} - \mathbf{curl}\,\mathbf{H}^{\times}, \qquad \text{in } \Omega, && \text{(2.39b)}\end{aligned}$$

the solution of which minimizes the Lagrangian functional (2.34). The Lagrange multiplier $\boldsymbol{\eta}$ is a vector potential representation for the magnetic field strength $\mathbf{H}$ and, following (2.38b), provides an update term for the unknown magnetic field strength. Together with

the definition of the magnetic vector potential $\mathbf{A}$, the field quantities can be retrieved with

$$\mathbf{B} = \mathbf{curl}\,\mathbf{A}, \tag{2.40a}$$

$$\mathbf{H} = \mathbf{H}^{\times} + \tilde{\boldsymbol{\nu}}\mathbf{curl}\,\boldsymbol{\eta}. \tag{2.40b}$$

Note that a gauge for the Lagrange multiplier $\boldsymbol{\eta}$, similar to the vector potential $\mathbf{A}$, is necessary to provide a well-posed problem. Additionally, be aware that the stationary solution is still subject to the BCs. Thereby, the Dirichlet BC acts on the normal component of the magnetic field density $\mathbf{B}$, respectively on the tangential component of the vector potential $\mathbf{A}$ and constrains therefore (2.39a). Contrarily, the Neumann BC is formulated with respect to the tangential component of the magnetic field strength $\mathbf{H}$ and thus constrains (2.39b).

A different treatment for solving the Lagrangian is found in [90]. Instead of applying Euler-Lagrange equations, the stationary points of the Lagrangian (2.34) can also be found by employing the Gâteaux derivative. Additionally, the BCs are added as an additional constraint to the Lagrangian. Then, one directly obtains the weak form to determine the unknown field quantities.

There exist numerous spatial discretization schemes which may be employed to discretize and solve (2.39). Those are for example the finite integration technique (FIT) [27], the boundary element method (BEM) [80, 83] and, most prominently, the FE method [16, 38]. Throughout this work, we will employ the latter one. Irrespective of the employed method, the solution of the system of equations (2.39) yields a new state $\zeta \in \mathcal{M}$ that complies with the equations for magnetostatics and simultaneously minimizes the weighted distance to the measurement state $\zeta^{\times}$.

Projection on measurement state

Given a state $\zeta^{\circ} \in \mathcal{M}$, a new state $\zeta^{\times} \in \mathcal{D}$ which is covered by the available measurement set and is closest to ζ° is found by solving

$$\zeta^{\times} \in \underset{\zeta \in \mathcal{D}}{\operatorname{argmin}} \left\| \zeta^{\circ} - \zeta \right\|^2_{L^2_{\tilde{\boldsymbol{\mu}},\tilde{\boldsymbol{\nu}}}(\Omega)}. \tag{2.41}$$

The minimization towards the measurement states (2.41) is without any further constraint. However, to solve the minimization problem (2.41), the function space defined by the measurement data in $\mathcal{D}$ needs to be constructed, which would be computationally infeasible [85]. As we will later see, a finite-dimensional subspace of admissible functions for $\mathbf{H}$ and $\mathbf{B}$ is necessary.

3 Data-driven magnetostatic finite element solver

In order to solve the two data-driven curl-curl equations (2.39) with the FE method, it is necessary to derive their weak forms. Subsequently, the FE formulations of the weak forms are presented by restricting the solution space to a finite-dimensional subspace of the original space. Afterwards, the algebraic equivalent systems of equations that correspond to the FE formulations are introduced.

3.1 Weak formulation

First, we multiply the curl-curl equations with test functions $\mathbf{A}' \in V_A$ and $\boldsymbol{\eta}' \in V_\eta$, respectively, where V_A and V_η are to be determined. Integration over the computational domain Ω results in

$$(\mathbf{curl}\,(\tilde{\boldsymbol{\nu}}\mathbf{curl}\,\mathbf{A}), \mathbf{A}')_\Omega = (\mathbf{curl}\,(\tilde{\boldsymbol{\nu}}\mathbf{B}^\times), \mathbf{A}')_\Omega, \tag{3.1a}$$

$$(\mathbf{curl}\,(\tilde{\boldsymbol{\nu}}\mathbf{curl}\,\boldsymbol{\eta}), \boldsymbol{\eta}')_\Omega = (\mathbf{J} - \mathbf{curl}\,\mathbf{H}^\times, \boldsymbol{\eta}')_\Omega. \tag{3.1b}$$

Applying Green's formula [16] yields

$$(\tilde{\boldsymbol{\nu}}\mathbf{curl}\,\mathbf{A}, \mathbf{curl}\,\mathbf{A}')_\Omega = (\tilde{\boldsymbol{\nu}}\mathbf{B}^\times, \mathbf{curl}\,\mathbf{A}')_\Omega + (\tilde{\boldsymbol{\nu}}\mathbf{curl}\,\mathbf{A} \times \mathbf{n}, \mathbf{A}')_\Gamma - (\tilde{\boldsymbol{\nu}}\mathbf{B}^\times \times \mathbf{n}, \mathbf{A}')_\Gamma, \tag{3.2a}$$

$$(\tilde{\boldsymbol{\nu}}\mathbf{curl}\,\boldsymbol{\eta}, \mathbf{curl}\,\boldsymbol{\eta}')_\Omega = (\mathbf{J}, \boldsymbol{\eta}')_\Omega - (\mathbf{H}^\times, \mathbf{curl}\,\boldsymbol{\eta}')_\Omega + (\tilde{\boldsymbol{\nu}}\mathbf{curl}\,\boldsymbol{\eta} \times \mathbf{n}, \boldsymbol{\eta}')_\Gamma + (\mathbf{H}^\times \times \mathbf{n}, \boldsymbol{\eta}')_\Gamma. \tag{3.2b}$$

The boundary terms in (3.2) are divided into a Dirichlet part Γ_D and a Neumann part Γ_N, as illustrated in Figure 2.1. The Dirichlet BC (2.1c) is an additional constraint to (3.2a) and will later be strongly enforced in the considered function space V_A. As the Neumann BC (2.1d) is related to (3.2b), the remaining boundary terms in (3.2a) vanish. Utilizing (2.40b) and the Neumann BC (2.1d), one obtains $\mathbf{H} \times \mathbf{n} = (\mathbf{H}^\times + \tilde{\boldsymbol{\nu}}\mathbf{curl}\,\boldsymbol{\eta}) \times \mathbf{n} = \mathbf{f}$, and further

$$(\tilde{\boldsymbol{\nu}}\mathbf{curl}\,\boldsymbol{\eta}, \mathbf{curl}\,\boldsymbol{\eta}')_\Omega = (\mathbf{J}, \boldsymbol{\eta}')_\Omega - (\mathbf{H}^\times, \mathbf{curl}\,\boldsymbol{\eta}')_\Omega + (\mathbf{f}, \boldsymbol{\eta}')_{\Gamma_\mathrm{N}}. \tag{3.3}$$

On the Dirichlet boundaries Γ_D in (3.2b), we strongly enforce $\boldsymbol{\eta} \times \mathbf{n} = 0$ in the function space V_η, as the Dirichlet BC (2.1c) is associated to the magnetic vector potential $\mathbf{A}$.

For brevity of notation, we also define the function spaces with vanishing trace, respectively with $u = 0$, on the boundary Γ_D as

$$\begin{aligned} \mathrm{H}_0(\mathbf{grad}; \Omega) &= \{u \in \mathrm{H}(\mathbf{grad}; \Omega) : u = 0 \text{ on } \Gamma_\mathrm{D}\}, \\ \mathrm{H}_0(\mathbf{curl}; \Omega) &= \{\mathbf{u} \in \mathrm{H}(\mathbf{curl}; \Omega) : \mathbf{u} \times \mathbf{n} = 0 \text{ on } \Gamma_\mathrm{D}\}. \end{aligned} \tag{3.4}$$

All numerical examples considered in this work feature only homogeneous Neumann and Dirichlet BCs, i.e., the Neumann parts in (3.3) are naturally fulfilled. The Dirichlet BCs are enforced in the chosen trial and test function spaces. Consequently, it holds that $V = V_A = V_\eta = \mathrm{H}_0(\mathbf{curl}; \Omega)$ and $\{\mathbf{A}', \boldsymbol{\eta}'\} \in V$, which allows us to test both weak formulations with $\mathbf{w} \in V$. Introducing the bilinear form

$$a(\mathbf{u}, \mathbf{w}) = (\tilde{\boldsymbol{\nu}} \mathbf{curl}\, \mathbf{u}, \mathbf{curl}\, \mathbf{w})_\Omega, \tag{3.5}$$

with $\mathbf{u} \in V$ and the right-hand side (RHS) functionals

$$l_A^\times(\mathbf{w}) = (\tilde{\boldsymbol{\nu}} \mathbf{B}^\times, \mathbf{curl}\, \mathbf{w})_\Omega, \tag{3.6a}$$

$$l_\eta^\times(\mathbf{w}) = (\mathbf{J}, \mathbf{w})_\Omega - (\mathbf{H}^\times, \mathbf{curl}\, \mathbf{w})_\Omega, \tag{3.6b}$$

the weak formulation reads: Find $\mathbf{A}, \boldsymbol{\eta} \in V$, such that

$$a(\mathbf{A}, \mathbf{w}) = l_A^\times(\mathbf{w}), \quad \forall \mathbf{w} \in V, \tag{3.7a}$$

$$a(\boldsymbol{\eta}, \mathbf{w}) = l_\eta^\times(\mathbf{w}), \quad \forall \mathbf{w} \in V. \tag{3.7b}$$

Again, the problem (3.7) is not uniquely defined since both vector fields are only defined up to a gradient field. That is, their function space has a large kernel comprising the gradients of functions from $\mathrm{H}(\mathbf{grad}; \Omega)$. Accordingly, the coercivity constraint on the bilinear forms is violated, i.e., $a(\mathbf{u}, \mathbf{u}) \not\geq \|\mathbf{u}\|_2^2 + \|\mathbf{curl}\, \mathbf{u}\|_2^2$. This can be directly deduced if, for instance, $\mathbf{u} = \mathbf{grad}\, \Phi$, then $a(\mathbf{u}, \mathbf{u}) = 0$, but $\|\mathbf{u}\|_2^2 = \|\mathbf{grad}\, \Phi\|_2^2$. To establish uniqueness, several approaches are available. To name but a few, those are for instance co-tree gauging [39, 33], which can be employed once (3.7) is available in its discrete counterpart. Furthermore, in [64, 102] it has been shown that non-gauged vector potential formulation in combination with a compatible RHS, i.e., $\mathrm{div}\, \mathbf{J} = 0$, can be solved with iterative solvers. Throughout this work, we consider the Coulomb gauge [60, 45] which

requires **A** to fulfill

$$\begin{aligned} \operatorname{div} \mathbf{A} &= 0, && \text{in } \Omega, \\ \mathbf{A} \times \mathbf{n} &= 0, && \text{on } \Gamma_{\mathrm{D}}. \end{aligned} \tag{3.8}$$

The gauging can be directly incorporated into the considered function space. A function $\mathbf{u} \in L^2(\Omega)^3$ satisfying

$$(\mathbf{u}, \mathbf{grad}\, \Psi)_\Omega = 0, \quad \forall \Psi \in \mathrm{H}_0(\mathbf{grad}; \Omega), \tag{3.9}$$

is said to be weakly divergence-free in Ω. Then, (3.7) remains as it is, but the function space changes to $W = \{\mathbf{v} \in \mathrm{H}_0(\mathbf{curl}; \Omega) : (\mathbf{v}, \mathbf{grad}\, \Psi)_\Omega = 0, \forall \Psi \in \mathrm{H}_0(\mathbf{grad}; \Omega)\}$. To explicitly implement the divergence-free constraint, we introduce the Lagrange multipliers λ_A, respectively λ_η, which leads to the mixed formulation, respectively to the saddle point problem. Considering (3.9), the mixed formulation reads: Find $\mathbf{A}, \boldsymbol{\eta} \in V$ and $\lambda_A, \lambda_\eta \in \mathrm{H}_0(\mathbf{grad}; \Omega)$, such that

$$a(\mathbf{A}, \mathbf{w}) + b(\mathbf{grad}\, \lambda_A, \mathbf{w}) = l_A^\times(\mathbf{w}), \quad \forall \mathbf{w} \in V, \tag{3.10a}$$

$$b(\mathbf{A}, \mathbf{grad}\, \Psi) = 0, \quad \forall \Psi \in \mathrm{H}_0(\mathbf{grad}; \Omega), \tag{3.10b}$$

$$a(\boldsymbol{\eta}, \mathbf{w}) + b(\mathbf{grad}\, \lambda_\eta, \mathbf{w}) = l_\eta^\times(\mathbf{w}), \quad \forall \mathbf{w} \in V, \tag{3.10c}$$

$$b(\boldsymbol{\eta}, \mathbf{grad}\, \Psi) = 0, \quad \forall \Psi \in \mathrm{H}_0(\mathbf{grad}; \Omega), \tag{3.10d}$$

where the bilinear form $b(\cdot, \cdot)$ for $\mathbf{u}, \mathbf{v} \in L^2(\Omega)^3$ is given by

$$b(\mathbf{u}, \mathbf{v}) = (\mathbf{u}, \mathbf{v})_\Omega \,. \tag{3.11}$$

3.1.1 Cartesian translational symmetry

To reduce the complexity of the considered BVP, it is customary to exploit symmetry conditions. In particular we want to mention translational symmetry which allows us to reduce a 3D problem into a 2D problem. Consider for example a dipole magnet, which is used in particle accelerators to bend the beam on a desired circular trajectory. Those magnets are typically very long. Therefore, in a preliminary design state, a 2D analysis might be sufficiently accurate. Furthermore, one is typically first interested in the field quality inside the magnet, that is, fringe fields at the front and at the back of the magnet can be neglected. Assuming translational symmetry for the excitation in the z-direction, implies $\mathbf{A}(x, y, z) = A_z(x, y)\, \mathbf{e}_z$, where $\mathbf{e}_z$ denotes the unit vector in z-direction. Then, the curl operator reduces to $\mathbf{curl}\, \mathbf{A} = \mathbf{curl}\, (0, 0, A_z) = (\partial_y A_z, -\partial_x A_z, 0)$. In $\mathbb{R}^2$, let $\mathbf{grad}^\perp = (-\partial_y, \partial_x)$ denote the perpendicular gradient operator. Then the weak

formulation reads: Find $A_z \in V_{2\mathrm{D}} = \{v \in \mathrm{H}(\mathbf{grad}; \Omega) : v = 0 \text{ on } \Gamma_D\}$, such that

$$a_{2\mathrm{D}}(A_z, w) = l^{\times}_{2\mathrm{D},A}(w), \quad \forall w \in V_{2\mathrm{D}}, \tag{3.12}$$

with

$$\begin{aligned} a_{2\mathrm{D}}(A_z, w) &= (\tilde{\boldsymbol{\nu}}\mathbf{grad}^{\perp} A_z, \mathbf{grad}^{\perp} w)_{\Omega}, \\ l^{\times}_{2\mathrm{D},A}(w) &= -(\tilde{\boldsymbol{\nu}}\mathbf{B}^{\times}, \mathbf{grad}^{\perp} w)_{\Omega}. \end{aligned} \tag{3.13}$$

In this case, no additional gauging is necessary as $A_z \in V_{2\mathrm{D}} \subset \mathrm{H}(\mathbf{grad}; \Omega)$. The 2D approximation for the weak form associated with the Lagrange multiplier η_z is derived in a similar fashion.

3.2 Finite element formulation

In order to solve the weak forms (3.10), respectively (3.12), a finite-dimensional function space needs to be introduced. However, topological properties of the vector calculus need to be preserved on the discrete level, e.g., the identities $\mathbf{curl}\,\mathbf{grad} = 0$, $\mathrm{div}\,\mathbf{curl} = 0$. Those properties are typically illustrated in the de Rahm complex

$$\mathrm{H}(\mathbf{grad}; \Omega) \xrightarrow{\mathbf{grad}} \mathrm{H}(\mathbf{curl}; \Omega) \xrightarrow{\mathbf{curl}} \mathrm{H}(\mathrm{div}; \Omega) \xrightarrow{\mathrm{div}} L^2(\Omega), \tag{3.14}$$

and have to be preserved in the discrete counterpart. We consider a partitioning of the domain Ω, denoted as $\mathcal{T}_h$, where h refers to the maximum mesh size of the elements in $\mathcal{T}_h$. Given $\mathcal{T}_h$, we define the finite-dimensional subspaces of (3.14) as $\mathrm{H}_h(\mathbf{grad}; \Omega)$, $\mathrm{H}_h(\mathbf{curl}; \Omega)$, $\mathrm{H}_h(\mathrm{div}; \Omega)$ and $L^2_h(\Omega)$, respectively. A sequence of finite-dimensional function spaces complying with the de Rahm complex (3.14) was introduced by Whitney, also referred to as Whitney forms [87, 15]. Alternatively, spline based shape functions can be employed, which are used in the context of isogeometric analysis (IGA) [55]. In this work, we employ the Whitney forms, which we briefly want to recall for the case of a tetrahedral triangulation $\mathcal{T}_h$. In the following, $\mathrm{P}_q(T)$ and $\mathrm{P}_q(T)^3$ denotes the scalar, respectively vectorial, space of polynomials of maximum degree q on a domain T. The

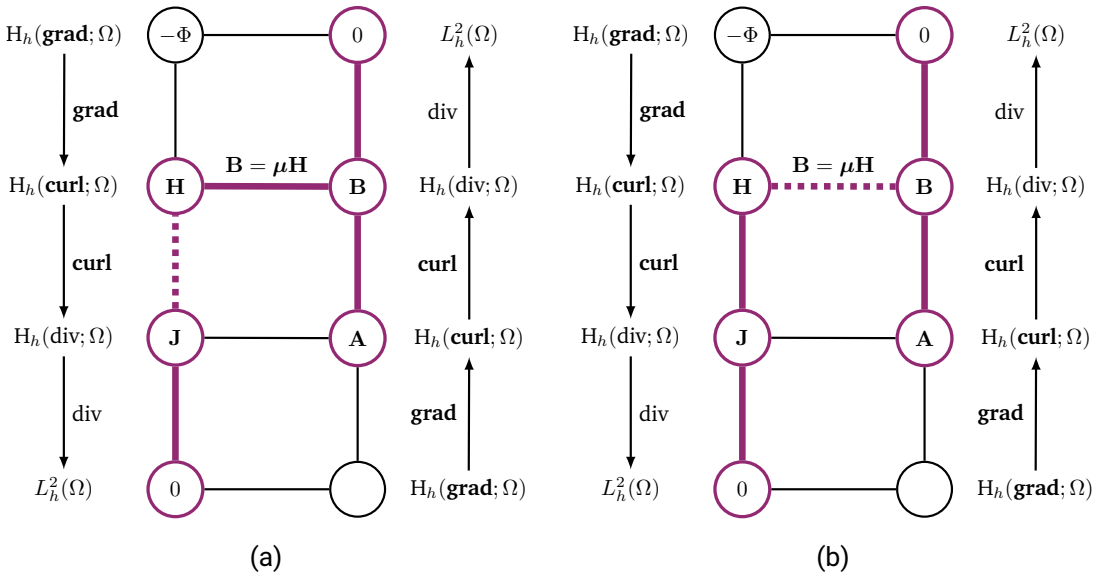

Figure 3.1: Tonti diagrams for the magnetostatic problem. The diagrams are read as follows: The operators next to the vertical lines link the variables topologically. The primal (right) and dual (left) quantities are linked through the horizontal line along the constitutive equations (phenomenological equations). The colored lines show the active equations, i.e., the equations corresponding to the chosen ansatz. Equations that are exactly fulfilled are depicted with solid lines, while those that are only weakly fulfilled or introduce approximation errors are represented by dashed lines. (a) Conventional approach with magnetic vector potential formulation . (b) Mixed-field (including the data-driven) approach. (Note that under the chosen Coulomb gauge implementation, $\mathrm{div}\,\mathbf{B}=0$ is only weakly satisfied in this work.)

discrete counterparts of (3.14), respectively (2.16) are then

$$\mathrm{H}_h(\mathbf{grad};\Omega) = \{u \in \mathrm{H}(\mathbf{grad};\Omega) : u \in \mathrm{P}_q(T_i),\ \forall T_i \in \mathcal{T}_h\}\,, \tag{3.15a}$$

$$\mathrm{H}_h(\mathbf{curl};\Omega) = \left\{\mathbf{u} \in \mathrm{H}(\mathbf{curl};\Omega) : \mathbf{u} \in \mathrm{P}_{q-1}(T_i)^3 + \mathrm{S}_q(T_i),\ \forall T_i \in \mathcal{T}_h\right\}, \tag{3.15b}$$

$$\mathrm{H}_h(\mathrm{div};\Omega) = \left\{\mathbf{u} \in \mathrm{H}(\mathrm{div};\Omega) : \mathbf{u} \in \mathrm{P}_{q-1}(T_i)^3 + \mathbf{x}\mathrm{P}_{q-1}(T_i),\ \forall T_i \in \mathcal{T}_h\right\}, \tag{3.15c}$$

$$L^2_h(\Omega) = \left\{u \in L^2(\Omega) : u \in \mathrm{P}_{q-1}(T_i),\ \forall T_i \in \mathcal{T}_h\right\}, \tag{3.15d}$$

$$L^2_h(\Omega)^3 = \left\{\mathbf{u} \in L^2(\Omega)^3 : \mathbf{u} \in \mathrm{P}_{q-1}(T_i)^3,\ \forall T_i \in \mathcal{T}_h\right\}, \tag{3.15e}$$

where $\mathrm{S}_q(T_i) = \{\mathbf{s} \in \mathrm{P}_q(T_i)^3 : \mathbf{s}(\mathbf{x}) \cdot \mathbf{x} = 0 \ \forall \mathbf{x} \in T_i\}$, see [68, 87, 86].

Ampère's and Gauss's laws give rise to two sequences characterized by (3.14). A typical way to visualize the topological properties is the so-called Tonti diagram, see Figure 3.1. The diagram is read as follows: The operators next to the vertical lines link the variables in a topological manner and are therefore called topological equations. Note that they are already the discrete version of (3.14). In the case of simply connected domains, i.e., domains without holes, the sets of the discrete sequence coincides with the ones in (3.14), see [5]. The primal (right) and dual (left) quantities are linked through the horizontal line along the constitutive equations, which belong to the so-called phenomenological equations [38]. The colored lines show the active equations, i.e., the equations corresponding to the chosen ansatz. Equations that are exactly fulfilled are depicted with solid lines, whereas equations that are only weakly satisfied or introduce approximation errors are represented by dashed lines.

In the traditional setting, the magnetostatic problem is typically solved with one of the two following approaches. In the first one, we solve for the magnetic field strength $\mathbf{H}_h \in \mathrm{H}_h(\mathbf{curl}; \Omega)$. This is achieved by either solving directly for $\mathbf{H}_h$, which leads to the $\mathbf{H} - \mathbf{A}$ [14, 40] formulation or by introducing the scalar potential $-\mathbf{grad}\,\varphi = \mathbf{H}$ [84, 13]. In any case, Ampère's law (2.1a) and the constitutive equation are exactly fulfilled by construction. However, Gauss's law (2.1b) is violated as the solenoidal property is not fulfilled at the element interfaces [17]. As the tangential properties of the magnetic field strength are exactly fulfilled, this approach is called H-conform. In the B-conform approaches, we solve for $\mathbf{B} \in \mathrm{H}_h(\mathrm{div}; \Omega)$. Again, this can be done directly, leading to the $\mathbf{B} - \Phi$ approach, or via the vector potential $\mathbf{B} = \mathbf{curl}\,\mathbf{A}$. Then, Gauss's law (2.1b) and the constitutive equation are fulfilled by construction. Yet, as in the H-conform approach, this comes at the price of introducing an error, this time however in Ampère's law (2.1a), which is only weakly satisfied. Note that when the mesh is refined, the quantity that lost the topological property will be recovered at the limit [16]. Figure 3.1a shows the Tonti diagram for magnetostatics when the problem is solved with the magnetic vector potential formulation. The dashed line indicates that Ampère's law is violated in this formulation.

A different approach is addressed with mixed-field solvers. Here, the variational formulation is formulated with respect to the magnetic field strength $\mathbf{H}$ and the magnetic flux density $\mathbf{B}$. The approach dates back to Rikabi et al. [104], who proposed a formulation that minimizes the error in the constitutive equation, while simultaneously fulfilling the topological equations (2.1a) and (2.1b) through constraints. The constraints can either be solved through the introduction of potentials for $\mathbf{H}$ and $\mathbf{B}$ or directly by expressing the fields in their natural function spaces [22, 3, 96, 2], that is, $\mathbf{H}_h \in \mathrm{H}_h(\mathbf{curl}; \Omega)$, known as edge-elements and $\mathbf{B}_h \in \mathrm{H}_h(\mathrm{div}; \Omega)$, known as face-elements. Irrespectively of introducing potentials to fulfill the topological equations or expressing the fields in their natural

function spaces, the solution that is obtained with the mixed-field solver exactly fulfills Ampère's and Gauss's law, while shifting the error entirely into the constitutive equation. A detailed overview regarding the different mixed-field solver approaches can be found in [103].

The proposed data-driven solver belongs to the class of mixed-field solvers. However, it treats the material relationship even more stringently by relying exclusively on measured data, rather than on an empirical material model. By that, the error is entirely shifted into the measured data, and the accuracy of the simulation is directly related to the quality and quantity of the measurement data. Note that in the presented approach, we introduced a vector potential to fulfill Gauss's law. A data-driven solver that solves directly for **H** and **B** is also possible and aligns well with the premise of the data-driven framework that treats field equations as exactly known. Figure 3.1b shows the Tonti diagram for magnetostatics when the problem is solved with a mixed-field solver, respectively the data-driven solver. The dashed line indicates that the approximation error is shifted into the constitutive relation.

3.2.1 Spatial and space discretization

The computational domain Ω is discretized into non-overlapping triangles (2D), respectively tetrahedra (3D). For a polyhedral domain Ω, it holds that $\bigcup_i \bar{T}_i = \bar{\Omega}$, where T_i refers to the corresponding element, depending on the spatial dimension.

- **2D:** In the 2D case, we solve for the scalar potentials A_z and η_z. Therefore, continuous Lagrange elements are considered, which are defined on the triangular element domain T_i with a finite-dimensional function space $\mathrm{H}_h(\mathbf{grad}; \Omega)$. Throughout this work, we consider linear Lagrange elements, that is, $\mathrm{H}_h(\mathbf{grad}; \Omega)$ is the span of first-order polynomials, also known as hat functions. The degrees of freedom (DoFs) are thus found on the vertices of the triangles T_i.
- **3D:** In the 3D case, we solve for the vector potentials **A** and $\boldsymbol{\eta}$. Consequently, Nédélec elements, also referred to as edge elements, are employed. The FE is then defined on a tetrahedra T_i, with function space $\mathrm{H}_h(\mathbf{curl}; \Omega)$. Throughout this work, we consider first kind, first order Nédélec basis functions. The DoFs then live on the edges of the tetrahedra.

For a detailed and rigorous definition of the *finite element*, the interested reader is referred to [26, 21]. Given the choice of the FE, the finite-dimensional subspace $\mathcal{D}_h$ is determined by

$$\mathcal{D}_h = \{\zeta_h \in L_h^2(\Omega)^3 \times L_h^2(\Omega)^3 : \zeta_h(\mathbf{x}) \in \tilde{\mathcal{D}}_{\Omega_i}, \forall \mathbf{x} \in \Omega_i, \forall i, \text{ a.e. in } \Omega\} \subset \mathcal{D}. \tag{3.16}$$

As we will see later, the data-driven algorithm demands for the field solution at the quadrature points of the FE assembly procedure. Therefore, we briefly want to derive a connection between the DoFs of the considered FE and the quadrature points. To keep things simple, we consider two scalar functions $u_h, v_h \in V_h \subset \mathrm{H}_h(\mathbf{grad}; \Omega)$. Following loosely [90], the L^2-projection reads

$$(u_h - v_h, w_h)_\Omega = 0 \quad \forall w_h \in V_h. \tag{3.17}$$

Note that since u_h and v_h belong to the same function space, with (3.17) both functions are identical in the L^2-sense. Let $u_h(\mathbf{x}) = \sum_{i=1}^{N} \phi_i \Phi_i(\mathbf{x})$, then

$$\sum_{i=1}^{N} \phi_i (\Phi_i, w_h)_\Omega = (v_h, w_h)_\Omega \quad \forall w_h \in V_h. \tag{3.18}$$

Let $V_h = \mathrm{span}\{\psi_j\}_{j=1}^{N}$, then

$$\sum_{i=1}^{N} \phi_i (\Phi_i, \psi_j)_\Omega = (v_h, \psi_j)_\Omega \quad j = 1, \ldots, N. \tag{3.19}$$

Computing the RHS (3.19) with numerical quadrature, we obtain

$$(v_h, \psi_j)_\Omega = \sum_{k=1}^{N_{\text{elements}}} \sum_{p=1}^{P} w_{p,k} v_h(\mathbf{x}_{p,k}) \psi_j(\mathbf{x}_{p,k}), \quad j = 1, \ldots, N, \tag{3.20}$$

where w_p denote the weights of the quadrature scheme. Furthermore, we assume that the quadrature scheme has a degree of precision equal or higher $2q$, where q is the polynomial degree of u_h, respectively v_h. Combining (3.19) with (3.20) yields

$$\sum_{i=1}^{N} \phi_i (\Phi_i, \psi_j)_\Omega = \sum_{k=1}^{N_{\text{elements}}} \sum_{p=1}^{P} w_{p,k} u_h(\mathbf{x}_{p,k}) \psi_j(\mathbf{x}_{p,k}), \quad j = 1, \ldots, N. \tag{3.21}$$

The last equation establishes a connection between the DoFs of a function in a finite-dimensional function space and the function values at the quadrature points. In turn, this means that given the basis functions of the employed function space V_h and the function values at the quadrature points, a function $u_h \in V_h$ can be reconstructed. This equivalence allows us to solve (2.41) at the quadrature points instead of actually constructing the functions $(\mathbf{H}_h, \mathbf{B}_h) \in \mathcal{D}_h$. The number of necessary quadrature points depends on the

employed quadrature scheme in combination with the considered element. For triangles and tetrahedra, there exists a vast literature on different schemes with different degrees of precision [119, 92, 62]. For all numerical examples considered in this work, first order trial and test functions have been employed. Therefore, employing for example the centroid rule, i.e., one quadrature point in the center of the element, polynomials up to a degree of 1 are integrated exactly, which is sufficient in our case. Note that by confining the FEs to linear elements, we effectively employ constant polynomials in $\mathcal{D}_h$.

3.2.2 Revisiting the data-driven problem

Now that the discrete spaces have been defined, we can revisit the two data-driven minimization problems, namely, (3.10), (3.12), and (2.41).

1. Regarding the minimization problem towards the equations for magnetostatics, the FE formulation is achieved by replacing the function spaces utilized in (3.10) with their discrete counterparts. The FE formulation then reads: Find $\mathbf{A}_h, \boldsymbol{\eta}_h \in V_h \subset V$ and $\lambda_{A,h}, \lambda_{\eta.h} \in \mathrm{H}_{h,0}(\mathbf{grad}; \Omega) \subset \mathrm{H}_0(\mathbf{grad}; \Omega)$, such that

$$
\begin{aligned}
a(\mathbf{A}_h, \mathbf{w}_h) + b(\mathbf{grad}\, \lambda_{A,h}, \mathbf{w}_h) &= l_A^{\times}(\mathbf{w}_h), \quad && \forall \mathbf{w}_h \in V_h, && \text{(3.22a)}\\
b(\mathbf{A}_h, \mathbf{grad}\, \Psi_h) &= 0, && \forall \Psi_h \in \mathrm{H}_{h,0}(\mathbf{grad}; \Omega), && \text{(3.22b)}\\
a(\boldsymbol{\eta}_h, \mathbf{w}_h) + b(\mathbf{grad}\, \lambda_{\eta,h}, \mathbf{w}_h) &= l_\eta^{\times}(\mathbf{w}_h), && \forall \mathbf{w}_h \in V_h, && \text{(3.22c)}\\
b(\boldsymbol{\eta}_h, \mathbf{grad}\, \Psi_h) &= 0, && \forall \Psi_h \in \mathrm{H}_{h,0}(\mathbf{grad}; \Omega). && \text{(3.22d)}
\end{aligned}
$$

   The field state $(\mathbf{H}_h^{\circ}, \mathbf{B}_h^{\circ}) \in \mathcal{M}_h$, with $\mathcal{M}_h$ to be determined, is then obtained through

$$
\begin{aligned}
\mathbf{B}_h^{\circ} &= \mathbf{curl}\, \mathbf{A}_h,\\
\mathbf{H}_h^{\circ} &= \mathbf{H}_h^{\times} + \tilde{\boldsymbol{\nu}} \mathbf{curl}\, \boldsymbol{\eta}_h.
\end{aligned}
\tag{3.23}
$$

   The finite-dimensional subspace $\mathcal{M}_h$ comprising the states that fulfill (3.22) is thus determined by

$$
\mathcal{M}_h = \{\zeta_h \in \mathrm{H}_h(\mathbf{curl}; \Omega) \times \mathrm{H}_h(\mathrm{div}; \Omega) : \text{(3.22) and (3.23)}\} \subset \mathcal{M}. \tag{3.24}
$$

2. Given $\zeta_h^\circ \in \mathcal{M}_h$, the minimization towards the measurement data now reads

$$\zeta_h^\times = \underset{\zeta_h \in \mathcal{D}_h}{\operatorname{argmin}} \, \|\zeta_h^\circ - \zeta_h\|^2_{L^2_{\tilde{\boldsymbol{\mu}},\tilde{\boldsymbol{\nu}}}(\Omega)} \,, \tag{3.25a}$$

$$\begin{aligned} &= \underset{\zeta_h \in \mathcal{D}_h}{\operatorname{argmin}} \int_\Omega \frac{1}{2}\tilde{\boldsymbol{\mu}}(\mathbf{H}_h^\circ - \mathbf{H}_h) \cdot (\mathbf{H}_h^\circ - \mathbf{H}_h) \, \mathrm{d}\Omega \\ &\qquad + \int_\Omega \frac{1}{2}\tilde{\boldsymbol{\nu}}(\mathbf{B}_h^\circ - \mathbf{B}_h) \cdot (\mathbf{B}_h^\circ - \mathbf{B}_h) \, \mathrm{d}\Omega, \end{aligned} \tag{3.25b}$$

$$\begin{aligned} &= \underset{\zeta_h \in \mathcal{D}_h}{\operatorname{argmin}} \sum_i^{N_\text{elements}} \int_{T_i} \frac{1}{2}\tilde{\boldsymbol{\mu}}(\mathbf{H}_h^\circ - \mathbf{H}_h) \cdot (\mathbf{H}_h^\circ - \mathbf{H}_h) \, \mathrm{d}T_i \\ &\qquad + \int_{T_i} \frac{1}{2}\tilde{\boldsymbol{\nu}}(\mathbf{B}_h^\circ - \mathbf{B}_h) \cdot (\mathbf{B}_h^\circ - \mathbf{B}_h) \, \mathrm{d}T_i. \end{aligned} \tag{3.25c}$$

The last equation shows that the minimization is carried out for each element individually. Furthermore, since only decoupled fields are considered, each dimension can be minimized separately, thus further simplifying the minimization problem. Taking this into account and considering a single element T_i located in the domain Ω_j, we find

$$\left(H_{h,r,i}^\times, B_{h,r,i}^\times\right) = \underset{(H_{h,r},B_{h,r}) \in \mathcal{D}_{h,r}}{\operatorname{argmin}} \int_{T_i} \left[\frac{1}{2}\tilde{\mu}_r (H_{h,r}^\circ - H_{h,r})^2 + \frac{1}{2}\tilde{\nu}_r (B_{h,r}^\circ - B_{h,r})^2\right] \mathrm{d}T_i, \tag{3.26}$$

with $\mathcal{D}_{h,r} = \{\zeta_h \in \mathcal{D}_h : (\mathbf{H}_h \cdot \mathbf{e}_r, \mathbf{B}_h \cdot \mathbf{e}_r)\}$, where $\mathbf{e}_r$ denotes the unit vector and $r \in \{x, y, z\}$. With the established connection between DoFs and quadrature nodes, we can solve (3.26) effectively on the quadrature nodes, that is

$$\begin{aligned} \left(H_{h,r,i}^\times, B_{h,r,i}^\times\right) = \underset{(H_{h,r},B_{h,r}) \in \mathcal{D}_{h,r}}{\operatorname{argmin}} \; & w_{p,i}\frac{1}{2}\tilde{\nu}_r(\mathbf{x}_{p,i}) \left(H_{h,r}^\circ(\mathbf{x}_{p,i}) - H_{h,r}(\mathbf{x}_{p,i})\right)^2 \\ & + w_{p,i}\frac{1}{2}\tilde{\mu}_r(\mathbf{x}_{p,i}) \left(B_{h,r}^\circ(\mathbf{x}_{p,i}) - B_{h,r}(\mathbf{x}_{p,i})\right)^2, \end{aligned} \tag{3.27}$$

where $w_{p,i}$ denotes the quadrature weight and $\mathbf{x}_{p,i}$ the quadrature node of element T_i. Now, considering the definition of the set $\mathcal{D}_h$, particularly $(H_{h,r}, B_{h,r})(\Omega_j) \in \tilde{D}_{\Omega_j,r}$, the minimization problem can be carried out on a discrete level with respect to the

data sets $\tilde{D}_{\Omega_j,r}$, that is,

$$(h^{\times}_{r,i}, b^{\times}_{r,i}) = \underset{(h,b)\in\tilde{\mathcal{D}}_{\Omega_j,r}}{\operatorname{argmin}} \; w_{p,i}\frac{1}{2}\tilde{\nu}_r(\mathbf{x}_{p,i})\left(H^{\circ}_{h,r}(\mathbf{x}_{p,i}) - h\right)^2 + w_{p,i}\frac{1}{2}\tilde{\mu}_r(\mathbf{x}_{p,i})\left(B^{\circ}_{h,r}(\mathbf{x}_{p,i}) - b\right)^2. \tag{3.28}$$

After solving (3.28) for every element and in each dimension, the global measurement state at the quadrature points is collected in the vector $(\mathbf{h}^{\times}, \mathbf{b}^{\times}) \in \mathbb{R}^{3N_{\text{elements}}} \times \mathbb{R}^{3N_{\text{elements}}}$ and, if necessary, can be projected onto the appropriate function space, that is, $L^2_h(\Omega)^3 \times L^2_h(\Omega)^3$. Note also that the discrete solution at the quadrature points lies in the global measurement set containing the discrete data (2.20), i.e., $(\mathbf{h}^{\times}, \mathbf{b}^{\times}) \in \tilde{D}$. The minimization problem (3.28) is essentially a nearest neighbor problem. There are several strategies to solve such problems efficiently. Considering large measurement data sets and/or a fine triangulation of Ω, the computationally most expensive approach is the brute force approach, where for each element, the distance to the entire data set needs to be calculated. On the plus side, this approach is straightforward to implement. Binary search trees like KD-trees [11] are a viable alternative to the brute force approach. There, the data are organized in a hierarchical manner, which allows for partitioning the data into smaller subspaces. KD-trees are computationally efficient in low dimensions, but their performance deteriorates as the dimension increases. Other approaches are for example locality-sensitive hashing [50] and metric trees [112], to name but a few.

3.2.3 System of equations

The weak formulations (3.22), respectively their 2D approximations, are equivalent to systems of linear equations. Let $(\boldsymbol{\varphi}_j)_{j=1}^{N_{\text{edges}}} \subset V_h$, respectively $(\psi_j)_{j=1}^{N_{\text{vertices}}} \subset V_{2\text{D},h}$, denote the set of shape functions, then

2D

$$A_{z,h} = \sum_{j=1}^{N_{\text{vertices}}} a_j \psi_j(\mathbf{x}), \tag{3.29a}$$

$$\eta_{z,h} = \sum_{j=1}^{N_{\text{vertices}}} \eta_j \psi_j(\mathbf{x}), \tag{3.29b}$$

3D

$$\mathbf{A}_h = \sum_{j=1}^{N_{\text{edges}}} a_j \boldsymbol{\varphi}_j(\mathbf{x}), \tag{3.29c}$$

$$\boldsymbol{\eta}_h = \sum_{j=1}^{N_{\text{edges}}} \eta_j \boldsymbol{\varphi}_j(\mathbf{x}), \tag{3.29d}$$

where N_{edges} and N_{vertices} denotes the number of edges and vertices respectively. Furthermore, a_j and η_j refer to the DoFs. Following the Ritz-Galerkin approach, the test and trial functions are chosen to be identical, which leads to the linear systems

2D

$$\mathbf{K}_{\tilde{\nu}}\mathbf{a}_z = \mathbf{l}_A^{\times}, \tag{3.30a}$$

$$\mathbf{K}_{\tilde{\nu}}\boldsymbol{\eta}_z = \mathbf{l}_{\eta}^{\times}, \tag{3.30b}$$

3D

$$\begin{bmatrix} \mathbf{K}_{\tilde{\nu}} & \mathbf{B}^{\top} \\ \mathbf{B} & \mathbf{0} \end{bmatrix} \begin{bmatrix} \mathbf{a} \\ \boldsymbol{\lambda}_A \end{bmatrix} = \begin{bmatrix} \mathbf{l}_A^{\times} \\ \mathbf{0} \end{bmatrix}, \tag{3.30c}$$

$$\begin{bmatrix} \mathbf{K}_{\tilde{\nu}} & \mathbf{B}^{\top} \\ \mathbf{B} & \mathbf{0} \end{bmatrix} \begin{bmatrix} \boldsymbol{\eta} \\ \boldsymbol{\lambda}_{\eta} \end{bmatrix} = \begin{bmatrix} \mathbf{l}_{\eta}^{\times} \\ \mathbf{0} \end{bmatrix}, \tag{3.30d}$$

with

2D

$$\mathbf{K}_{\tilde{\nu},ij} = (\tilde{\boldsymbol{\nu}}\mathbf{grad}^{\perp}\psi_j, \mathbf{grad}^{\perp}\psi_i)_{\Omega}, \tag{3.31a}$$

$$\mathbf{l}_{A,i} = -(\tilde{\boldsymbol{\nu}}\mathbf{B}^{\times}, \mathbf{grad}^{\perp}\psi_i)_{\Omega}, \tag{3.31b}$$

$$\mathbf{l}_{\eta,i} = (J, \psi_i)_{\Omega} + (\mathbf{H}^{\times}, \mathbf{grad}^{\perp}\psi_i)_{\Omega}, \tag{3.31c}$$

3D

$$\mathbf{K}_{\tilde{\nu},ij} = (\tilde{\boldsymbol{\nu}}\mathbf{curl}\,\boldsymbol{\varphi}_j, \mathbf{curl}\,\boldsymbol{\varphi}_i)_{\Omega}, \tag{3.31d}$$

$$\mathbf{B}_{ij} = (\boldsymbol{\varphi}_j, \mathbf{grad}\,\theta_i)_{\Omega}, \tag{3.31e}$$

$$\mathbf{l}_{A,i} = (\tilde{\boldsymbol{\nu}}\mathbf{B}^{\times}, \mathbf{curl}\,\boldsymbol{\varphi}_i)_{\Omega}, \tag{3.31f}$$

$$\mathbf{l}_{\eta,i} = (\mathbf{J}, \boldsymbol{\varphi}_i)_{\Omega} - (\mathbf{H}^{\times}, \mathbf{curl}\,\boldsymbol{\varphi}_i)_{\Omega}, \tag{3.31g}$$

where $(\theta_i)_{i=1}^{N_{\text{vertices}}} \subset \mathrm{H}_{h,0}(\mathbf{grad};\Omega)$ are nodal shape functions and $\lambda_{A,h} = \sum_{j=1}^{N_{\text{vertices}}} \lambda_{A,j}\theta_j(\mathbf{x})$, respectively $\lambda_{\eta,h} = \sum_{j=1}^{N_{\text{vertices}}} \lambda_{\eta,j}\theta_j(\mathbf{x})$. For further details on the properties of the saddle point problem and appropriate algorithms for its solution, we refer to [12] and the references therein.

3.2.4 Practical considerations

The L^2-projection from one function space onto another results on a discrete level in a system of equation that requires solving. This projection is necessary for $\mathbf{H}_h^{\times}$ and $\mathbf{B}_h^{\times}$, once per data-driven iteration. However, to circumvent the need for projection, both field states, i.e., $(\mathbf{h}^{\circ}, \mathbf{b}^{\circ})$ and $(\mathbf{h}^{\times}, \mathbf{b}^{\times})$ are retained at the quadrature points. In turn, that means that the update equations are evaluated solely at the quadrature nodes, i.e.,

$$\mathbf{b}^{\circ} = \left[(\mathbf{curl}\,\mathbf{A}_h(\mathbf{x}_1))^{\top}, \ldots, (\mathbf{curl}\,\mathbf{A}_h(\mathbf{x}_{N_{\text{elements}}}))^{\top}\right]^{\top}, \tag{3.32a}$$

$$\mathbf{h}^{\circ} = \mathbf{h}^{\times} + \left[(\tilde{\boldsymbol{\nu}}(\mathbf{x}_1)\mathbf{curl}\,\boldsymbol{\eta}_h(\mathbf{x}_1))^{\top}, \ldots, (\tilde{\boldsymbol{\nu}}(\mathbf{x}_{N_{\text{elements}}})\mathbf{curl}\,\boldsymbol{\eta}_h(\mathbf{x}_{N_{\text{elements}}}))^{\top}\right]^{\top}, \tag{3.32b}$$

with $\mathbf{b}^{\circ}, \mathbf{h}^{\circ} \in \mathbb{R}^{3N_{\text{elements}}}$. Once the data-driven solver has converged, the fields can be projected onto their natural function spaces.

3.2.5 Algorithm

The data-driven algorithm can be compactly presented in the Algorithm 1.

Algorithm 1 Iterative scheme for the data-driven FE field solver for magnetostatic problems. The algorithm employs a global weighting factor.

initialize $(\mathbf{h}^{\times}, \mathbf{b}^{\times})$ randomly on measurement data
while $(\mathbf{h}^{\circ}, \mathbf{b}^{\circ})_i \neq (\mathbf{h}^{\circ}, \mathbf{b}^{\circ})_{i-1}$ and $|\Delta_{\text{em},i} - \Delta_{\text{em},i-1}| > \delta_{\Delta_{\text{em}}}$ **do**

Solve

$$\mathbf{K}_{\boldsymbol{\nu}}\mathbf{a} = \mathbf{l}_A^{\times}$$
$$\mathbf{K}_{\boldsymbol{\nu}}\boldsymbol{\eta} = \mathbf{l}_{\eta}^{\times}$$

Update

$$\mathbf{b}^{\circ} = \left[(\mathbf{curl}\,\mathbf{A}_h(\mathbf{x}_1))^{\top}, \ldots, (\mathbf{curl}\,\mathbf{A}_h(\mathbf{x}_{N_{\text{elements}}}))^{\top}\right]^{\top}$$
$$\mathbf{h}^{\circ} = \mathbf{h}^{\times} + \left[(\tilde{\boldsymbol{\nu}}(\mathbf{x}_1)\mathbf{curl}\,\boldsymbol{\eta}_h(\mathbf{x}_1))^{\top}, \ldots, (\tilde{\boldsymbol{\nu}}(\mathbf{x}_{N_{\text{elements}}})\mathbf{curl}\,\boldsymbol{\eta}_h(\mathbf{x}_{N_{\text{elements}}}))^{\top}\right]^{\top}$$

Find $(\mathbf{h}^{\times}, \mathbf{b}^{\times})$ in $\tilde{\mathcal{D}}$ adjacent to $(\mathbf{h}^{\circ}, \mathbf{b}^{\circ})$ with (3.28).
Compute energy mismatch $|\Delta_{\text{em},i}|$ with (2.31).
end while

4 Hybrid data-driven simulation

Electromagnetic problems often involve heterogeneous domains with materials of different properties. For instance, an already simplified model of an inductor typically comprises three distinct domains, namely, a domain filled with air, a domain where the wiring is arranged, and the iron part. The material relations in the air and coil domains are often assumed to be well-known and only a negligible error is attributed to the modeling assumptions. However, the iron yoke is often made out of electrical steel, which exhibits a strongly nonlinear material response. Therefore, following the famous quote of George Box, "*Essentially, all models are wrong, but some are useful*", the hybrid solver incorporates prescribed material relations alongside to data-defined material relations. The hybrid solver is not limited to simple materials like vacuum. Nonlinear material relations that have been painstakingly established and have been found reliable and trustworthy over the years can be integrated in addition. However, throughout this work, if not explicitly stated differently, solely data are employed in the nonlinear regions instead of constructing a material model therefrom.

In the following, three distinct approaches are proposed, which utilize the known material relation in the domain where the material is known in combination with the proposed data-driven solver that exclusively employs measurement data. These ideas closely follow the own publication [36], but instead of utilizing the discrete linear systems to derive the data-driven problem, we derive the data-driven problem in the continuous form by utilizing the Euler-Lagrange equations as discussed in Section 2.2.2. For simplicity, we consider only linear known material relations, i.e., in the form $\mathbf{B} = \boldsymbol{\mu}\mathbf{H}$, where $\boldsymbol{\mu}$ is a tensor with known, linear permeability. Furthermore, the domain is split into separate parts, such that $\Omega = \Omega_{\mathrm{dd}} \cup \Omega_{\mathrm{ex}}$, where Ω_{dd} refers to the purely data-driven region, that is, only measurement data are employed, and Ω_{ex} to the region where the material relation

is exactly known. Therefore, we define the indicator functions

$$\mathbb{1}_{\Omega_{\text{ex}}}(\mathbf{x}) = \begin{cases} 1, & \mathbf{x} \in \Omega_{\text{ex}} \\ 0, & \text{otherwise} \end{cases}, \tag{4.1a}$$

$$\mathbb{1}_{\Omega_{\text{dd}}}(\mathbf{x}) = \begin{cases} 1, & \mathbf{x} \in \Omega_{\text{dd}} \\ 0, & \text{otherwise} \end{cases}. \tag{4.1b}$$

4.1 Exact material relation minimized by the nearest neighbor algorithm

In the first approach, the known material relation corresponds to an infinite number of synthetic measurement points in the HB phase space. Following this line of thought, the minimization with respect to the (infinite) measurement data is still performed in the context of the nearest neighbor problem. Consequently, the Lagrangian (2.33) remains unchanged. However, the weighting factors $\tilde{\boldsymbol{\mu}}$ and $\tilde{\boldsymbol{\nu}}$ in (2.39) within the domain characterized by the known material relation are assigned to their exact counterparts $\boldsymbol{\mu}$ and $\boldsymbol{\nu}$. The minimization problem is then carried out with the known material relation, that is,

$$(\mathbf{H}_h^{\times}, \mathbf{B}_h^{\times}) = \underset{\substack{(\mathbf{H}_h, \mathbf{B}_h) \in \{(\mathbf{H},\mathbf{B}) \in \\ L_h^2(\Omega)^3 \times L_h^2(\Omega)^3 : \\ \mathbf{B} = \boldsymbol{\mu}(\mathbf{H})\mathbf{H}\}}}{\operatorname{argmin}} \|\mathbf{H}_h^{\circ} - \mathbf{H}_h\|^2_{L^2_{\boldsymbol{\mu}}(\Omega_{\text{ex}})} + \|\mathbf{B}_h^{\circ} - \mathbf{B}_h\|^2_{L^2_{\boldsymbol{\nu}}(\Omega_{\text{ex}})}, \tag{4.2}$$

which can be resolved independently for each dimension due to our assumption of decoupled fields. In the subsequent discussion, we consider the case of a linear material, i.e., $\mathbf{B} = \boldsymbol{\mu}\mathbf{H}$. As shown in Section 3.2.2, the minimization problem can be solved at the quadrature points, which results in

$$\min_{\mathbf{b}} \left\{ \frac{1}{2}(\mathbf{h}^{\circ} - \boldsymbol{\nu}\mathbf{b})^{\top} \boldsymbol{\mu} (\mathbf{h}^{\circ} - \boldsymbol{\nu}\mathbf{b}) + \frac{1}{2}(\mathbf{b}^{\circ} - \mathbf{b})^{\top} \boldsymbol{\nu} (\mathbf{b}^{\circ} - \mathbf{b}) \right\}. \tag{4.3}$$

where $\boldsymbol{\nu} = \boldsymbol{\mu}^{-1}$ are diagonal matrices containing the permeability and reluctivity values at the quadrature points, respectively. Taking the derivative with respect to $\mathbf{b}$ yields

$$\mathbf{h}^{\circ} + \boldsymbol{\nu}\mathbf{b}^{\circ} - 2\boldsymbol{\nu}\mathbf{b} \overset{!}{=} 0. \tag{4.4}$$

Further solving for $\mathbf{b}$ and incorporating the known material relations, the optimal states at the quadrature points are determined as

$$\mathbf{b}^{\times} = \frac{\mathbf{b}^{\circ} + \boldsymbol{\mu}\mathbf{h}^{\circ}}{2}, \tag{4.5a}$$

$$\mathbf{h}^{\times} = \boldsymbol{\nu}\mathbf{b}^{\times}. \tag{4.5b}$$

If a material with a nonlinear BH-characteristic is considered, the optimal states can be derived analytically or, in case no closed-form solution is found, equation (4.2) is solved numerically with standard optimization tools. Once the new state $(\mathbf{h}^{\times}, \mathbf{b}^{\times})$ is determined, the weighting factors in the corresponding elements need to be updated with the permeability and reluctivity of the current operating point within the nonlinear BH-curve.

4.2 Exact material relation minimized in the distance function

Instead of minimizing the field states in the domains with known material relation with (3.28), the minimization can be included in the FE solver. We consider the known material representation $\mathbf{B} = \boldsymbol{\mu}\mathbf{H}$, with corresponding distance function

$$\|\mathbf{B} - \boldsymbol{\mu}\mathbf{H}\|^2_{L^2_{\boldsymbol{\nu}}(\Omega_{\text{ex}})}. \tag{4.6}$$

The Lagrangian thus reads

$$\begin{aligned}\mathcal{L}(\mathbf{x}, \mathbf{H}, \mathbf{curl}\,\mathbf{H}, \mathbf{curl}\,\mathbf{A}) = {} & \|\mathbf{H} - \mathbf{H}^{\times}\|^2_{L^2_{\boldsymbol{\mu}}(\Omega_{\text{dd}})} + \|\mathbf{curl}\,\mathbf{A} - \mathbf{B}^{\times}\|^2_{L^2_{\tilde{\boldsymbol{\nu}}}(\Omega_{\text{dd}})} \\ & + (\boldsymbol{\eta}, \mathbf{J} - \mathbf{curl}\,\mathbf{H})_{\Omega_{\text{dd}}} \\ & + \|\mathbf{curl}\,\mathbf{A} - \boldsymbol{\mu}\mathbf{H}\|^2_{L^2_{\boldsymbol{\nu}}(\Omega_{\text{ex}})} + (\boldsymbol{\eta}, \mathbf{J} - \mathbf{curl}\,\mathbf{H})_{\Omega_{\text{ex}}},\end{aligned} \tag{4.7}$$

which after applying Euler-Lagrange equations (2.37) yields the stationary solution

$$\mathbb{1}_{\Omega_{\text{dd}}}\mathbf{curl}\,(\tilde{\boldsymbol{\nu}}\mathbf{curl}\,\mathbf{A}) + \mathbb{1}_{\Omega_{\text{ex}}}\mathbf{curl}\,(\boldsymbol{\nu}\mathbf{curl}\,\mathbf{A}) = \mathbb{1}_{\Omega_{\text{dd}}}\mathbf{curl}\,(\tilde{\boldsymbol{\nu}}\mathbf{B}^{\times}) + \mathbb{1}_{\Omega_{\text{ex}}}\mathbf{curl}\,\mathbf{H}, \tag{4.8a}$$

$$\mathbb{1}_{\Omega_{\text{dd}}}(\mathbf{H} + \tilde{\boldsymbol{\nu}}\mathbf{curl}\,\boldsymbol{\eta}) + \mathbb{1}_{\Omega_{\text{ex}}}(\mathbf{H} + \boldsymbol{\nu}\mathbf{curl}\,(\boldsymbol{\eta} - \mathbf{A})) = \mathbb{1}_{\Omega_{\text{dd}}}\mathbf{H}^{\times}. \tag{4.8b}$$

Applying the curl operator (4.8b), imposing the constraint $\mathbf{J} = \mathbf{curl}\,\mathbf{H}$, and after a bit of calculus we arrive at

$$\mathbb{1}_{\Omega_{\text{dd}}}\mathbf{curl}\,(\tilde{\boldsymbol{\nu}}\mathbf{curl}\,\mathbf{A}) + \mathbb{1}_{\Omega_{\text{ex}}}\mathbf{curl}\,(\boldsymbol{\nu}\mathbf{curl}\,\boldsymbol{\eta}) = \mathbb{1}_{\Omega_{\text{dd}}}\mathbf{curl}\,(\tilde{\boldsymbol{\nu}}\mathbf{B}^{\times}), \tag{4.9a}$$

$$\mathbb{1}_{\Omega_{\text{ex}}}\mathbf{curl}\,(\boldsymbol{\nu}\mathbf{curl}\,\mathbf{A}) - \mathbb{1}_{\Omega_{\text{ex}}}\mathbf{curl}\,(\boldsymbol{\nu}\mathbf{curl}\,\boldsymbol{\eta}) - \mathbb{1}_{\Omega_{\text{dd}}}\mathbf{curl}\,(\tilde{\boldsymbol{\nu}}\mathbf{curl}\,\boldsymbol{\eta}) = \mathbf{J} - \mathbb{1}_{\Omega_{\text{dd}}}\mathbf{curl}\,\mathbf{H}^{\times}. \tag{4.9b}$$

A detailed derivation can be found in the appendix 9.1.1. The update terms for a new state $(\mathbf{H}, \mathbf{B})$ are given by

$$\mathbf{B} = \mathbf{curl}\,\mathbf{A}, \qquad \mathbf{x} \in \Omega, \tag{4.10a}$$

$$\mathbf{H} = \mathbf{H}^{\times} - \tilde{\boldsymbol{\nu}}\mathbf{curl}\,\boldsymbol{\eta}, \quad \mathbf{x} \in \Omega_{\text{dd}}, \tag{4.10b}$$

$$\mathbf{H} = \boldsymbol{\nu}\mathbf{curl}\,(\mathbf{A} - \boldsymbol{\eta}), \quad \mathbf{x} \in \Omega_{\text{ex}}. \tag{4.10c}$$

The corresponding FE formulation reads: Find $\mathbf{A}_h, \boldsymbol{\eta}_h \in W_h \subset W$, such that

$$(\tilde{\boldsymbol{\nu}}\mathbf{curl}\,\mathbf{A}_h, \mathbf{curl}\,\mathbf{w}_h)_{\Omega_{\text{dd}}} + (\boldsymbol{\nu}\mathbf{curl}\,\boldsymbol{\eta}_h, \mathbf{curl}\,\mathbf{w}_h)_{\Omega_{\text{ex}}} = (\tilde{\boldsymbol{\nu}}\mathbf{B}_h^{\times}, \mathbf{curl}\,\mathbf{w}_h)_{\Omega_{\text{dd}}}, \tag{4.11a}$$

$$\begin{aligned}(\boldsymbol{\nu}\mathbf{curl}\,\mathbf{A}_h, \mathbf{curl}\,\mathbf{w}_h)_{\Omega_{\text{ex}}} - (\boldsymbol{\nu}\mathbf{curl}\,\boldsymbol{\eta}_h, \mathbf{curl}\,\mathbf{w}_h)_{\Omega_{\text{ex}}} \\ -(\tilde{\boldsymbol{\nu}}\mathbf{curl}\,\boldsymbol{\eta}_h, \mathbf{curl}\,\mathbf{w}_h)_{\Omega_{\text{dd}}} = (\mathbf{J}, \mathbf{w}_h)_{\Omega} - (\mathbf{H}_h^{\times}, \mathbf{curl}\,\mathbf{w}_h)_{\Omega_{\text{dd}}},\end{aligned} \tag{4.11b}$$

for all $\mathbf{w}_h \in W_h$, where we incorporated the gauge into the function space W_h to shorten the notation. The nearest neighbor problem is confined to the region Ω_{dd}, as the states allocated in Ω_{ex} are already minimized in the FE solver. It is worth noting that energy minimization in Ω_{ex} is similar to the idea proposed by Rikabi et al. [104], see also [22]. Therein, (4.6) is minimized over the entire domain, enforcing Ampère's and Gauss's laws as constraints. As in [22], the approximation error inherent to the FE method is still shifted to the material equation and Maxwell's laws are exactly fulfilled.

4.3 Exact material relation minimized in the Lagrange multiplier

Since the material relation in the domain Ω_{ex} is known, we can directly enforce the exact material relation in the Lagrange multiplier. The Lagrangian thus reads

$$\begin{aligned}\mathcal{L}(\mathbf{x}, \mathbf{H}, \mathbf{curl}\,\mathbf{H}, \mathbf{curl}\,\mathbf{A}) = \|\mathbf{H} - \mathbf{H}^{\times}\|^2_{L^2_{\tilde{\boldsymbol{\mu}}}(\Omega_{\text{dd}})} + \|\mathbf{curl}\,\mathbf{A} - \mathbf{B}^{\times}\|^2_{L^2_{\tilde{\boldsymbol{\nu}}}(\Omega_{\text{dd}})} \\ + (\boldsymbol{\eta}, \mathbf{J} - \mathbf{curl}\,\mathbf{H})_{\Omega_{\text{dd}}} + (\boldsymbol{\eta}, \mathbf{J} - \mathbf{curl}\,(\boldsymbol{\nu}\mathbf{curl}\,\mathbf{A}))_{\Omega_{\text{ex}}}.\end{aligned} \tag{4.12}$$

Applying the Euler-Lagrange equations (2.37) yields

$$\mathbb{1}_{\Omega_{\text{dd}}}\mathbf{curl}\,(\tilde{\boldsymbol{\nu}}\mathbf{curl}\,\mathbf{A}) + \mathbb{1}_{\Omega_{\text{ex}}}\mathbf{curl}\,(\boldsymbol{\nu}\mathbf{curl}\,\boldsymbol{\eta}) = \mathbb{1}_{\Omega_{\text{dd}}}\mathbf{curl}\,(\tilde{\boldsymbol{\nu}}\mathbf{B}^{\times}), \tag{4.13a}$$

$$\mathbb{1}_{\Omega_{\text{ex}}}\mathbf{curl}\,(\boldsymbol{\nu}\mathbf{curl}\,\mathbf{A}) - \mathbb{1}_{\Omega_{\text{dd}}}\mathbf{curl}\,(\tilde{\boldsymbol{\nu}}\mathbf{curl}\,\boldsymbol{\eta}) = \mathbf{J} - \mathbb{1}_{\Omega_{\text{dd}}}\mathbf{curl}\,\mathbf{H}^{\times}, \tag{4.13b}$$

with the update terms

$$\mathbf{B} = \mathbf{curl}\,\mathbf{A}, \qquad \mathbf{x} \in \Omega, \tag{4.14a}$$

$$\mathbf{H} = \mathbf{H}^{\times} - \tilde{\boldsymbol{\nu}}\mathbf{curl}\,\boldsymbol{\eta}, \quad \mathbf{x} \in \Omega_{\text{dd}}, \tag{4.14b}$$

$$\mathbf{H} = \boldsymbol{\nu}\mathbf{curl}\,\mathbf{A}, \qquad \mathbf{x} \in \Omega_{\text{ex}}. \tag{4.14c}$$

A detailed derivation can be found in the appendix 9.1.2. The corresponding FE formulation reads: Find $\mathbf{A}_h, \boldsymbol{\eta}_h \in W_h \subset W$, such that

$$(\tilde{\boldsymbol{\nu}}\mathbf{curl}\,\mathbf{A}_h, \mathbf{curl}\,\mathbf{w}_h)_{\Omega_{\text{dd}}} + (\boldsymbol{\nu}\mathbf{curl}\,\boldsymbol{\eta}_h, \mathbf{curl}\,\mathbf{w}_h)_{\Omega_{\text{ex}}} = (\tilde{\boldsymbol{\nu}}\mathbf{B}_h^{\times}, \mathbf{curl}\,\mathbf{w}_h)_{\Omega_{\text{dd}}}, \tag{4.15a}$$

$$(\boldsymbol{\nu}\mathbf{curl}\,\mathbf{A}_h, \mathbf{curl}\,\mathbf{w}_h)_{\Omega_{\text{ex}}} - (\tilde{\boldsymbol{\nu}}\mathbf{curl}\,\boldsymbol{\eta}_h, \mathbf{curl}\,\mathbf{w}_h)_{\Omega_{\text{dd}}} = (\mathbf{J}, \mathbf{w}_h)_{\Omega} - (\mathbf{H}_h^{\times}, \mathbf{curl}\,\mathbf{w}_h)_{\Omega_{\text{dd}}}, \tag{4.15b}$$

for all $\mathbf{w}_h \in W_h$. In contrast to the second approach 4.2, (4.15) exactly fulfills Ampère's and Gauss's law in the data-driven region Ω_{dd}, however not in Ω_{ex}, where Ampère's law is violated. Instead, the material relation $\mathbf{B}_h = \boldsymbol{\mu}\mathbf{H}_h$ is fulfilled exactly.

4.4 Summary

We proposed three different approaches to integrate prescribed material relations into the data-driven solver. Two approaches modify the BVP, which leads to mixed-formulations in the FE method. Consequently, their implementation is more involved, and the matrices have a more complex structure than in the approach that minimizes using the nearest neighbor algorithm, see Section 4.1. However, the two approaches reduce the number of nearest neighbor queries in the nearest neighbor problem. Contrarily, the approach that minimizes using the nearest neighbor algorithm offers a simple way to handle nonlinear known material relations, compared to the more involved derivation of the other two approaches. A comparison in terms of accuracy and performance of the introduced methods will be provided at a later stage of this work.

5 Adaptive weighting factors

If not explicitly stated otherwise, the following is based on the work of the author, as presented in [47]. So far, the choice of the weighting factors $\widetilde{\boldsymbol{\nu}}$ in the context of data-driven solvers has not been addressed. In a conventional magnetostatic formulation, the permeability has to follow certain physical constraints. For example, it is well-known that the relation between B and H in a ferromagnetic material is monotonically increasing with a slope of at least μ_0. Contrarily, the weighting factor $\widetilde{\boldsymbol{\nu}}$ within the data-driven solver does not necessarily represent the physical behavior of the material and is instead of computational nature [69]. Nonetheless, certain constraints on the weighting factors are necessary to achieve a well-posed problem in the FE method. Considering the weak form (3.10), it is clearly visible that the weighting factors need to be bounded from below and above. Furthermore, for the weak forms (3.10) to remain coercive, a stricter criteria is necessary, i.e., $\exists \nu_{\text{min}} > 0$, such that

$$\nu_{\text{min}} \leq \tilde{\nu}_r \leq \nu_0, \tag{5.1a}$$

with $r = \{x, y, z\}$. Even when considering (5.1), the exact choice of the weighting factors remains an open question. Indeed, in the special case of linear elasticity, it has been shown that the data-driven solver asymptotically recovers the conventional solution, independently of the chosen norm (2.24) [30]. Yet, numerical tests have indicated that properly chosen weighting factors can significantly boost the convergence speed, improve the accuracy, and reduce statistical dispersion coming from the randomly chosen initial values [47]. This becomes significantly relevant in three different scenarios. First, when considering sparse data sets. Second, when examining unbalanced data sets, by which we mean data sets with areas that are densely populated and other areas that are sparse or devoid of data. Last, when utilizing materials that exhibit a strongly nonlinear response.

For the rest of this section, we consider a one-dimensional problem. The extension to two or three dimensions is straightforward as we consider only anisotropic materials without mutual interaction between the axes. To properly calculate the distance between two states in the HB phase space, the phase space needs to be weighted. This is done by the weighting factors, which effectively stretch and squeeze the axes. The most basic

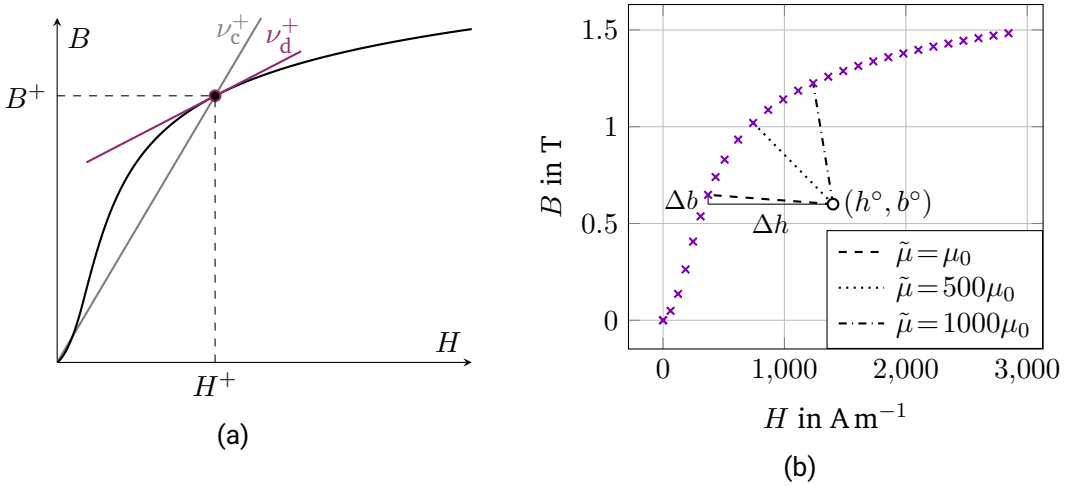

(a) (b)

Figure 5.1: (a) Nonlinear BH-curve and estimated *chord* reluctivity ν_c^+ and *differential* reluctivity ν_d^+, respectively at an operating point (H^+, B^+). (b) Distance minimization of a single state (h°, b°) (black circle) to the measurement data (purple crosses). The minimization is carried out with three different weighting factors $\tilde{\mu}$.

choice for the weighting factors would be $\tilde{\mu} = \tilde{\nu} = 1$. However, even when considering a highly permeable material, the values of H and B differ by orders of magnitude, as do the differences in $H - H^\times$ and $B - B^\times$. In such cases, the minimization process tends to prioritize either the discrepancy in H or in B. Additionally, the ratio between H and B strongly depends on the utilized material, which immediately demands for a spatially dependent weighting factor. Finally, considering materials with a nonlinear response, the current operating point in the HB phase space has a large influence on the ratio between H and B, see Figure 5.1a. This is of particular interest, since we consider soft magnetic materials in the numerical examples. The BH-curves of those ferromagnetic materials feature a steep linear part, followed by a sharp transition into saturation. In summary, a spatially and field dependent weighting factor is necessary, i.e., $\tilde{\mu} = \tilde{\mu}(x, (H, B))$, that is adaptively adjusted during the data-driven procedure. Adaptively updated local weighting factors were first proposed in [47] in the area of electromagnetic field simulation and then adapted to elasticity [88].

Subsequently, we illustrate why adaptively updated local weighting factors improve the convergence speed and additionally enhance the accuracy, especially if sparse data sets are employed. We consider a single state $(h^\circ, b^\circ) = (H_h(x_p), B_h(x_p))$ with $(H_h, B_h) \in \mathcal{M}_h$,

and where x_p denotes the quadrature point in the considered element. The state is depicted in Figure 5.1b together with its corresponding discrete measurement data. In the next step, we want to find the state $(h^\times, b^\times)$, that minimizes the distance to the measurement data, that is

$$(h^\times, b^\times) = \underset{(h,b)\in\tilde{\mathcal{D}}_\Omega}{\operatorname{argmin}} \underbrace{\frac{1}{2}\tilde{\mu}(h^\circ - h)^2}_{\Delta h} + \underbrace{\frac{1}{2}\tilde{\nu}(b^\circ - b)^2}_{\Delta b}. \tag{5.2}$$

Let us consider two distinct cases. First, we employ $\tilde{\mu} = \mu_0$, which implies that the difference in the magnetic flux densities is the main contributing factor in (5.2). This can also be observed in Figure 5.1b. Second, the weighting factor is chosen to be $\tilde{\mu} = 1000\mu_0$ and, consequently, the minimization is only performed in the magnetic field strength H. Now, assume that the optimal solution is approximately in the middle between the two recently found points. Employing one of the introduced weighting factors and keeping it fixed throughout the data-driven iterations means that in one of the two directions, only minor corrections are carried out in each iteration, which means the data-driven solver needs to iterate through the entire data set to finally reach the optimal point. This leads to a significant increase of iterations when the data sets become larger. However, by choosing the weighting factor adaptively, such that both minimization parts are well balanced, the number of data-driven iterations is substantially reduced.

The second improvement when employing adaptively chosen weighting factors is related to sparse or unevenly distributed data sets. Let us consider a global, constant weighting factor and a sparse measurement data set. Furthermore, the data-driven algorithm has converged. An illustration of the scenario is given in Figure 5.2a which shows the HB phase space in the x-direction. Herein, the purple crosses show the measurement data and the black dots the states conforming with the magnetostatic problem, that are obtained after convergence of the algorithm with a global weighting factor. We consider a single element and a state $(h_i^\times, b_i^\times)$ in iteration i that minimizes the distance to a state (h_i°, b_i°), but is distant from that state. In the next projection step, a new state $(h_{i+1}^\circ, b_{i+1}^\circ)$ which conforms with the equations for magnetostatics is found. However, we can then observe that the updated state is again distant from the measurement set and further iterations do not lead to an improvement. In those cases, the measurement data set $\mathcal{D}_h$ fails to provide a state that sufficiently conforms to the governing equations. Consequently, the global weighting factor in the system matrices (3.31) projects the updated field solution onto a fictitious material dictated by the global weighting factor. This can be observed in Figure 5.2a, where a global weighting factor was employed that suits the steep linear part of the BH-curve. Consequently, a large number of magnetostatic states are projected

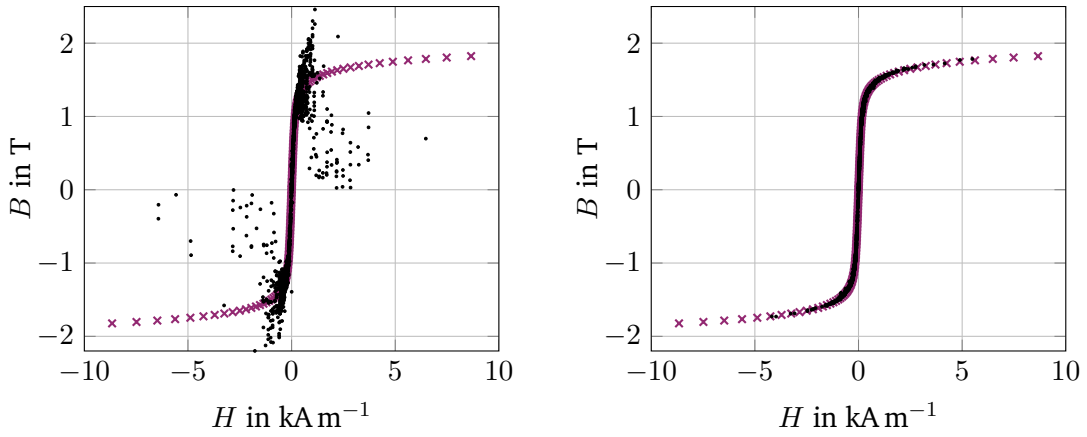

Figure 5.2: Measurement data (purple crosses) and states that are compatible with the equations for magnetostatics (black dots) in the HB phase space. The results have been obtained for $N = 100$ measurement data points, after convergence of the algorithm. (a) Global weighting factor. (b) Local, adaptively adjusted weighting factors.

in the thought extension of the steep linear part of the BH-curve. As there is only one global weighting factor, this is very likely to occur if a nonlinear material is considered as the operating points are spread entirely over the BH-curve. Again, employing the local adaptively updated weighting factor, a significant improvement in accuracy is achieved, as the fictitious material suits now the current operating point of the elements, see Figure 5.2b.

Before we illustrate the strategy to specify the weighting factor, we recall the two possible linearizations used to solve the nonlinear magnetostatic problem, that is, the successive-substitution method, also known as the fixed-point method, and the Newton method, respectively [53]. The reluctivity is then linearized at an operating point (H^+, B^+) such that

$$H - H^+ = \nu_{\mathrm{c}}^+ (B - B^+), \tag{5.3a}$$
$$H - H^+ = \nu_{\mathrm{d}}^+ (B - B^+), \tag{5.3b}$$

where ν_{c}^{+} and ν_{d}^{+} are the *chord* and *differential* reluctivity [35], respectively, defined as

$$\nu_{\mathrm{c}}^{+} = \frac{H^{+}}{B^{+}}, \tag{5.4a}$$

$$\nu_{\mathrm{d}}^{+} = \frac{\mathrm{d}H^{+}}{\mathrm{d}B^{+}}. \tag{5.4b}$$

One of the presented linearizations is then carried out for each element of the triangulation of Ω. Consequently, after each iteration the system matrix needs to reassembled. Figure 5.1a illustrates the chord and the differential reluctivity.

In the data-driven setting however, the problem formulation (3.10) is linear and thus does not inherently incorporate the treatment of nonlinear material responses. However, the data-driven iteration is a replacement thereof. Consequently, certain choices of $\tilde{\boldsymbol{\mu}}$, respectively $\tilde{\boldsymbol{\nu}}$, increase the convergence rate of the data-driven solver. Numerical tests have shown that using the differential reluctivity, that is, the tangent on the current operating point, achieves the largest gain in performance and accuracy. By that, the method mimics the conventional Newton approach to solve nonlinear PDEs. Therefore, we omit further details on the chord reluctivity and focus only on the differential reluctivity.

In the following, we want to estimate the differential reluctivity by only employing the discrete measurement data points available in our measurement set $\tilde{\mathcal{D}}$. Subsequently, the differential reluctivity is then adaptively chosen within the data-driven solver to update the weighting factors locally. Since we consider only measurement data that is not polluted by noise and other errors, we can sort the data such that

$$(H_n, B_n) < (H_{n+1}, B_{n+1}), \quad n = 1, \dots, N-1, \tag{5.5}$$

which is understood element-wise, i.e., $H_n < H_{n+1}$ and $B_n < B_{n+1}$. Utilizing the centered differences scheme yields

$$\nu_{\mathrm{d}}(B_n) = \frac{\mathrm{d}H}{\mathrm{d}B} \approx \frac{H_{n+1} - H_{n-1}}{B_{n+1} - B_{n-1}}, \quad n = 2, \dots, N-1. \tag{5.6}$$

To obtain an approximation on the differential reluctivity at $n = 1$ and $n = N$, forward and backward differences can be respectively employed,

$$\nu_{\mathrm{d}}(B_1) \approx \frac{H_2 - H_1}{B_2 - B_1}, \tag{5.7}$$

$$\nu_{\mathrm{d}}(B_N) \approx \frac{H_N - H_{N-1}}{B_N - B_{N-1}}. \tag{5.8}$$

In case of noisy measurement data, a clustering of the measurement data is performed beforehand [47]. Then, the centers of the clusters are employed to calculate an approximation on the differential reluctivity.

Remark: We motivated the use of adaptive weighting factors by mimicking the conventional Newton method and observations on the distance minimizing. A more quantitative interpretation of the possible mismatch in (5.2) is found in [88].

5.1 Global weighting factors

If a global weighting factor is employed, we need to obtain a factor that is best balanced over the entire data set. Assuming that the available data are equidistantly distributed and the range of the data set suits the problem, a global weighting factor can be obtained by averaging over the discrete reluctivity, that is,

$$\tilde{\nu} = \frac{1}{N} \sum_{n=1}^{N} \nu(B_n), \tag{5.9}$$

where $\nu(\cdot)$ refers to either the chord or the differential reluctivity. However, if the data set contains clusters or if the range is largely beyond the scope of the problem, this estimation is likely to be biased. Then, other statistical location parameter can be used, for instance, the median. If some prior knowledge is available, for example, the problem is designed such that the field solution $(\mathbf{H}, \mathbf{B})$ in most parts of the domain operates in the steep linear region of the BH-curve, a rough estimate, e.g., $\mu = 1000\mu_0$, can be employed as a global weighting factor. In summary, choosing a global weighting factor is a critical and challenging task, as it has to suit the entire range of the used measurement points. This issue is addressed by using local adaptively adjusted weighting factors.

5.2 Local weighting factors

Since we have no prior knowledge on the operating point of each element, the weighting factors need to be assigned adaptively during the data-driven iteration. At the beginning of the algorithm, the factors are initialized as in the case of a global weighting factor, see Section 5.1. A few iterations with a globally averaged weighting factor are necessary, since the states $(\mathbf{h}^\times, \mathbf{b}^\times)$ are randomly initialized in $\mathcal{D}_h$. A too early local adaptivity could estimate factors that are not optimal. After a few (≈ 4) iterations, the global weighting factor is substituted by local ones. The local weighting factors are updated with respect

to the current operating point within the material data set. Now, every time a new state $(\mathbf{H}_h^\times, \mathbf{B}_h^\times) \in \mathcal{D}_h$ is obtained, the weighting factors are updated such that

$$\tilde{\nu}_r(\mathbf{x}) = \sum_{e=1}^{N_{\text{elements}}} \nu_{\text{d},r}(b_e^\times)\mathbb{1}_e(\mathbf{x}), \tag{5.10}$$

$$\mathbb{1}_e(\mathbf{x}) = \begin{cases} 1, & \mathbf{x} \in T_e \\ 0, & \text{else} \end{cases}, \tag{5.11}$$

where T_e refers to the e-th element of the triangulation of Ω, $b_e^\times = B_{h,r}^\times(\mathbf{x}_e)$, $\mathbf{x}_e$ denotes the quadrature point in element e and $r \in \{x, y, z\}$. The newly assigned weighting factor $\tilde{\boldsymbol{\nu}}$ and its inverse $\tilde{\boldsymbol{\mu}}$ are now employed for one iteration in the weak forms (3.22) and in the distance function (3.28). Consequently, the linear system matrices in (3.31) need to be reassembled. The presented approach seems similar to the way material constants are assigned within a standard Newton solver. Still, the material is not explicitly modeled, and the data-driven solver does not attribute a physical representation to the weighting factors. The data-driven Algorithm 1 is adapted accordingly, as shown in Algorithm 2.

5.3 Summary

We discussed the influence of the weighting factors $\tilde{\boldsymbol{\mu}}, \tilde{\boldsymbol{\nu}}$ on the performance and accuracy of the data-driven algorithm. A local adaptively adjusted weighting factor was proposed, which is chosen to be the tangent on the current operating point in the HB data phase space. Therefore, each element in the triangulation of Ω obtains its own weighting factor and, as a consequence, the stiffness matrices of the FE method need to be reassembled in each data-driven iteration.

Algorithm 2 Iterative scheme for the data-driven FE magnetostatic field solver. The gray part shows the extension according to the local weighting factors.

initialize $(\mathbf{h}^{\times}, \mathbf{b}^{\times})$ randomly on measurement data
estimate $\widetilde{\boldsymbol{\nu}}$ with measurement data
while $(\mathbf{h}^{\circ}, \mathbf{b}^{\circ})_i \neq (\mathbf{h}^{\circ}, \mathbf{b}^{\circ})_{i-1}$ and $|\Delta_{\mathrm{em},i} - \Delta_{\mathrm{em},i-1}| > \delta_{\Delta_{\mathrm{em}}}$ **do**

Solve

$$\mathbf{K}_{\boldsymbol{\nu}}\mathbf{a} = \mathbf{l}_A^{\times}$$
$$\mathbf{K}_{\boldsymbol{\nu}}\boldsymbol{\eta} = \mathbf{l}_{\eta}^{\times}$$

Update

$$\mathbf{b}^{\circ} = \left[(\mathbf{curl}\,\mathbf{A}_h(\mathbf{x}_1))^{\top}, \ldots, (\mathbf{curl}\,\mathbf{A}_h(\mathbf{x}_{N_{\text{elements}}}))^{\top}\right]^{\top}$$
$$\mathbf{h}^{\circ} = \mathbf{h}^{\times} + \left[(\tilde{\boldsymbol{\nu}}(\mathbf{x}_1)\mathbf{curl}\,\boldsymbol{\eta}_h(\mathbf{x}_1))^{\top}, \ldots, (\tilde{\boldsymbol{\nu}}(\mathbf{x}_{N_{\text{elements}}})\mathbf{curl}\,\boldsymbol{\eta}_h(\mathbf{x}_{N_{\text{elements}}}))^{\top}\right]^{\top}$$

Find $(\mathbf{h}^{\times}, \mathbf{b}^{\times})$ in $\mathcal{D}_h$ adjacent to $(\mathbf{h}^{\circ}, \mathbf{b}^{\circ})$ with (3.28).
Compute energy mismatch $|\Delta_{\mathrm{em},i}|$ with (2.31).

if $i > 4$ **then**
  assign local weighting factor $\tilde{\boldsymbol{\nu}}$ to elements (5.10)
  reassemble stiffness matrix $\mathbf{K}_{\tilde{\boldsymbol{\nu}}}$ (3.31)
  update distance function with $\tilde{\boldsymbol{\nu}}$ (3.28)
end if

only for local weighting factor assignment

end while

6 Computational complexity

The computational complexity of the data-driven solver is dictated by two main factors. For each data-driven iteration, two linear systems need to be solved, followed by the evaluation of the nearest neighbor problem. Depending on the number of DoFs, the amount of measurement data, and the dimension of the phase space, the dominating costs are related to either solving the linear systems or finding the nearest neighbors.

Solving a linear system amounts to a complexity of $\mathcal{O}(N_{\text{edges}}^3)$ if a standard direct solver is used. This complexity is analogous to the one of a standard Newton solver, where the majority of the computational cost is also attributed to solving a linear system in each iteration. However, considering for instance approach 1 from Section 4.1, two linear systems of the same size as those in the Newton solver have to be solved in the data-driven case.

As the data and/or the dimension increases, the nearest neighbor problem becomes the dominating factor in computational efficiency. However, the computational costs of the nearest neighbor problem are linked to the chosen method. If a brute-force computation is carried out, finding all nearest points has a complexity $\mathcal{O}(N_{\text{elements}}N)$. Hence, brute-force computation is effective only for small data sets. However, there is no training time as all computation is done on demand. Using a KD-tree, the average complexity for finding the nearest points is $\mathcal{O}(N_{\text{elements}} \log N)$. The training of the KD-tree strongly depends on the considered algorithm. However, irrespective of the choice, if many queries are expected, i.e., N_{elements} is large, the costs for training are negligible.

There are several strategies to further decrease the computational costs. Without any claim to completeness, these are for instance:

- If a global weighting factors is employed, LU-factorization can be used, reducing the costs for solving the system to $\mathcal{O}(N_{\text{edges}}^2)$, where the cost for the factorization is $\mathcal{O}(N_{\text{edges}}^3)$ to be spent only once. Then, the data-driven solver scales (asymptotically) better than the Newton solver. However, if the weighting factors are adaptively altered, the system matrices have to be reassembled, which negates the benefit of the LU-factorization.

- Adaptively chosen weighting factors drastically reduce the number of data-driven

iterations, see [47]. However, this approach is not straightforward to apply if non-diagonal weighting factors $\tilde{\boldsymbol{\nu}}$ are employed. Furthermore, as the distance metric changes in each iteration, sophisticated nearest neighbor approaches such as binary search trees become unattractive, as a new training sequence would be necessary after each data-driven iteration.

- The computational cost of the nearest neighbor problem increases significantly if dimension and/or data density increases. A multi-level based approach was presented in [74] to tackle that issue. Here, multi-level is thought in the data sense, i.e., a hierarchical sequence of data sets of increasing cardinality is employed with $\tilde{\mathcal{D}}_0 \subset \tilde{\mathcal{D}}_1 \subset \ldots \tilde{\mathcal{D}}_N$, where $\tilde{\mathcal{D}}_0$ denotes the coarsest level. The coarse data sets are extended by data of a finer set that lies within a predefined sphere with respect to the solution converged with the coarse set. This approach is of particular interest when one is in the big data regime for high dimensional problems.

- Investigations on the efficiency of the nearest neighbor problem have been the focus in [42]. Therein, efficient data-structures have been employed together with approximate nearest neighbor algorithms, which significantly reduced the computational demand of the nearest neighbor problem.

In summary, we may conclude that the data-driven solver remains more costly than the conventional one. However, the exact costs are strongly problem dependent and are related to the amount of available data and used mesh size. Furthermore, on the side of the conventional solver, the costs for finding an appropriate model is an additional burden that does not exist in the data-driven framework.

7 Properties of the data-driven minimization problem

In this section, we discuss the properties of the data-driven optimization problem and the influence of the randomly chosen initial states on the data-driven solution. Both aspects will be analyzed on a practical level. For a rigorous mathematical analysis, we refer the reader to [30, 31]. However, we would like to summarize some key findings from these studies. In the case of linear elasticity, it has been shown that the conventional solution is recovered when the measurement data set is locally a graph, i.e., following $\mathbf{H}(\mathbf{B})$. That means that if the constitutive equation is sampled with increasing fidelity, the data-driven solution converges to the conventional solution that uses this constitutive equation. In turn, if real measurement data (excluding noise and measurement errors) is considered, the data-driven solver converges asymptotically to the underlying hidden material response. The influence of the weighting factors and the initially chosen states has further been discussed and analyzed in [69, 66, 90, 97, 10, 75].

First, we investigate the entire minimization problem, i.e., without splitting the double minimization problem into two distinct minimization problems and performing a fixed-point iteration. Therefore, we revisit the introductory example in Section 2.2.1. To illustrate the behavior of the distance function of the minimization problem, we employ (2.7) which allows us to directly incorporate the circuit constraint into the minimization problem. The minimization problem is thus given by

$$\min_{H} F(H, \tilde{\mathcal{D}}) = \min_{H} \min_{(H^\times, B^\times) \in \tilde{\mathcal{D}}} \tilde{\mu} \left(H - H^\times\right)^2 + \tilde{\nu} \left(-\frac{\ell_{\text{Fe}}}{\mathcal{R}_{\text{air}} S_{\text{Fe}}} H + \frac{N_{\text{coil I}}}{\mathcal{R}_{\text{air}} S_{\text{Fe}}} - B^\times \right)^2 . \tag{7.1}$$

The normalized variant of the distance function (7.1) is shown in Figure 7.1a over the magnetic field strength H for different weighting factors $\tilde{\mu}$. For the computation of the distance function, 20 data points have been employed. We can clearly observe that the choice of the weighting factors has a large impact on the characteristics of the minimization problem. In this case, choosing $\tilde{\mu}$ too small, results in a highly non-convex minimization problem. The function smooths out as a larger constant is considered, or if directly the

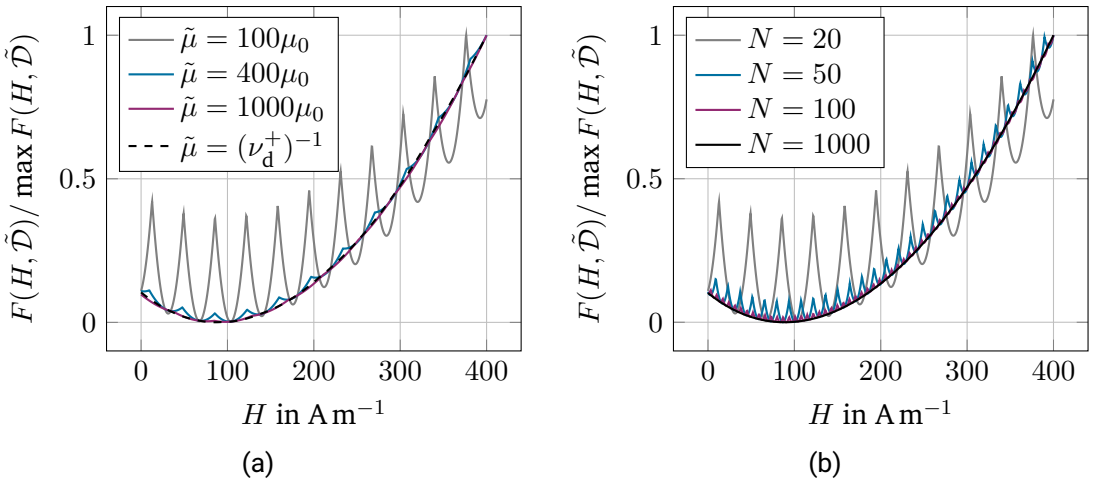

Figure 7.1: Normalized distance function over magnetic field strength H. (a) For $N = 20$ and varying weighting factor $\tilde{\mu}$. (b) For $\tilde{\mu} = 100\mu_0$ and increasing amount of measurement data.

adaptively chosen weighting factors introduced in Section 5 are employed. However, even when considering a sub-optimal choice for the weighting factor, e.g., $\tilde{\mu} = 100\mu_0$, the distance function becomes manageable as more measurements are taken into account, which is in line with the theoretical findings in [30]. The distance function for $\tilde{\mu} = 100\mu_0$ for increasing cardinality of the measurement data sets is depicted in Figure 7.1b. In conclusion, minimizing the distance function remains a non-convex optimization problem due to the finite number of data points.

Let us now return to the fixed-point iteration. Figure 7.2a shows the fixed-point iteration for $N = 20$ data points and a weighting factor $\tilde{\mu} = 400\mu_0$ (black nodes and gray arrows), respectively for $\tilde{\mu} = (\nu_\mathrm{d}^+)^{-1}$ (blue nodes, blue arrows). Both simulations have been carried out until $\zeta_i^\times = \zeta_{i+1}^\times$, i.e., the nearest neighbor problem selects the same measurement state in two consecutive iterations. The figure illustrates the issue of the non-convex optimization problem. Considering a sub-optimal choice $\tilde{\mu} = 400\mu_0$ and the sparse data set, the solver stagnates at a local minimum, distant from the optimal solution. Therefore, the initial starting point $(h^\times, b^\times)$ has a large influence on the accuracy of the solution. Contrarily, if an adaptively chosen weighting factor is considered, the solver converges with a few iterations in a close neighborhood of the optimal solution. As the amount of measurement data employed increases, the accuracy of the solver improves, bringing the solution closer to the optimal one, see Figure 7.2b for $N = 100$. However, even when not

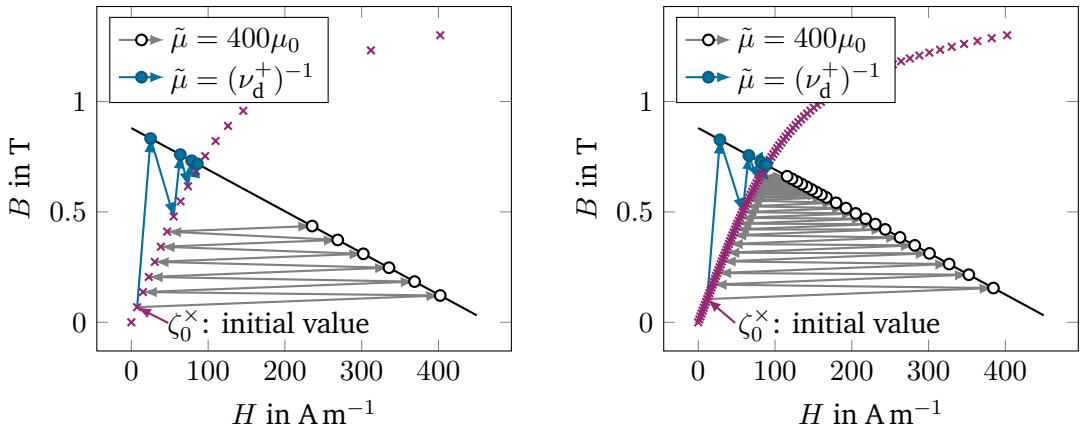

Figure 7.2: Fixed-point minimization in the HB phase space of the circuit problem from Section 2.2.1. The crosses show the available measurement data, the black line shows the states compatible with the circuit equation. The minimization has been carried out for $\tilde{\mu} = 400\mu_0$ (gray arrows, black nodes) and $\tilde{\mu} = (\nu_\mathrm{d}^+)^{-1}$ (blue arrows, blue nodes) until the solver reached convergence. (a) For $N = 20$ data points. (b) For $N = 100$ data points.

obtaining the optimal solution, numerical tests have shown that the data-driven solver provides a suitable approximation of the solution. We will strengthen this statement later when discussing the numerical results.

A different approach that does not rely on the fixed-point iteration was proposed in [66]. There, the optimization problem is solved globally through mixed-integer programming. However, this approach is unfeasible if large data sets are employed.

8 Numerical examples

Our goal is now to validate the proposed data-driven model-free FE solver. A typical approach is to compute a solution with a different solver that is accepted to produce viable results, which can then be employed as a reference. In our case, this is a conventional FE solver which either uses successive-substitution or the Newton method to solve the nonlinear PDE. The employed material relation in the reference solution is then the starting point for the data-driven solver. To show the convergence of the data-driven solver, we generate synthetic measurement data utilizing the material relation used in the conventional solver. Since the limited data set is only an approximation of the true material relation, the data-driven solution is expected to converge towards the reference solution as the accuracy of the approximation improves. This is achieved by generating sets of increasing cardinality, wherein the data points are evenly distributed in either $\mathbf{H}$ or $\mathbf{B}$. Furthermore, to focus on the error which is attributed to the finite amount of measurement data, both solutions, the data-driven and the conventional one, are computed on the same mesh. To measure the error in the field solution, we introduce the error norm

$$\epsilon_{\text{em}} = \frac{\|\zeta_h^\circ - \zeta_{h,\text{ref}}\|_{L^2_{\boldsymbol{\mu}_{\text{ref}},\boldsymbol{\nu}_{\text{ref}}}(\Omega)}}{\|\zeta_{h,\text{ref}}\|_{L^2_{\boldsymbol{\mu}_{\text{ref}},\boldsymbol{\nu}_{\text{ref}}}(\Omega)}}, \tag{8.1}$$

where $\zeta_h^\circ \in \mathcal{M}_h$, $\zeta_{h,\text{ref}}$ is the reference solution and $\boldsymbol{\mu}_{\text{ref}}, \boldsymbol{\nu}_{\text{ref}}$ are the permeability and reluctivity, respectively, of the reference solution. In case of a nonlinear material relation, $\boldsymbol{\mu}_{\text{ref}}$ and $\boldsymbol{\nu}_{\text{ref}}$ are evaluated at the resulting operating point within the BH-curve. Moreover, the error in the parts with known material relation (here only the air parts) is monitored with the relative error in the energy, that is,

$$\epsilon_{\text{air}} = \frac{\left|(\mathbf{H}_h, \mathbf{B}_h)_{\Omega_{\text{air}}} - (\mathbf{H}_{h,\text{ref}}, \mathbf{B}_{h,\text{ref}})_{\Omega_{\text{air}}}\right|}{(\mathbf{H}_{h,\text{ref}}, \mathbf{B}_{h,\text{ref}})_{\Omega_{\text{air}}}}. \tag{8.2}$$

To quantify the uncertainty in the solution due to the randomly chosen starting values $(\mathbf{h}^\times, \mathbf{b}^\times) \in \tilde{\mathcal{D}}$, we also compute the median, also known as the 50th percentile $Q_2[\boldsymbol{\epsilon}_{\text{em}}]$, the 25th percentile (first quartile $Q_1[\boldsymbol{\epsilon}_{\text{em}}]$), and the 75th percentile (third quartile $Q_3[\boldsymbol{\epsilon}_{\text{em}}]$)

[49, 63]. Here, $\boldsymbol{\epsilon}_{\text{em}}$ is a vector containing the energy mismatch for M simulation runs with randomly chosen initial values. Other statistical location parameters such as the mean can also be computed. However, the numerical results exhibit a heavily skewed probability density function (PDF), which is the reason why the percentiles $Q_1[\boldsymbol{\epsilon}_{\text{em}}]$, $Q_2[\boldsymbol{\epsilon}_{\text{em}}]$, and $Q_3[\boldsymbol{\epsilon}_{\text{em}}]$ are more reasonable metrics compared to mean and variance. If not stated differently, $M = 100$ simulations with randomly chosen initial values are carried out. Note that if the hybrid approaches are under investigation, they share the same measurement set and additionally the same random initializations. Furthermore, all numerical results have been obtained with a stopping criterion of $\delta_{\Delta_{\text{em}}} = 10^{-10}$. For the sake of brevity, we will call the hybrid approaches in the order of their introduction, that is,

- approach 1: Exact material relation minimized by the nearest neighbor algorithm, see Section 4.1;
- approach 2: Exact material relation minimized in the distance function, see Section 4.2;
- approach 3: Exact material relation minimized in the Lagrange multiplier, see Section 4.3.

8.1 Quadrupole

For our numerical investigations, we consider the model of a quadrupole magnet. Together with dipole magnets which bend the beam and sextupoles magnets which correct chromaticity, quadrupole magnets are one of the key parts in synchrotron accelerators, as the large hadron collider (LHC) at CERN [116]. Quadrupole magnets are utilized to focus the beam, such that particle beam trajectories are kept close to the design orbit. Quadrupole magnets provide a so-called gradient field, that is, the magnetic field strength increases linearly with respect to the distance of the magnet's center. Focusing only on the field in transversal direction, we neglect the fringe fields of the magnet at the front and at the back and consequently consider a two-dimensional model of reduced computational complexity. The 2D cross-section of the quadrupole is illustrated in Figure 8.1a and consists of three different domains. These are the vacuum part in white, the iron yoke in gray, and the excitation coils in purple. Assuming that the permeability of the yoke is sufficiently high, the magnetic flux is forced to stay in the yoke and fringe fields can be neglected. Then, a homogeneous Dirichlet BC is satisfactory on the outer domain of the quadrupole. Furthermore, exploiting the rotational symmetry of the model, it is sufficient to consider only one eighth of the quadrupole's geometry, shown in Figures 8.1a

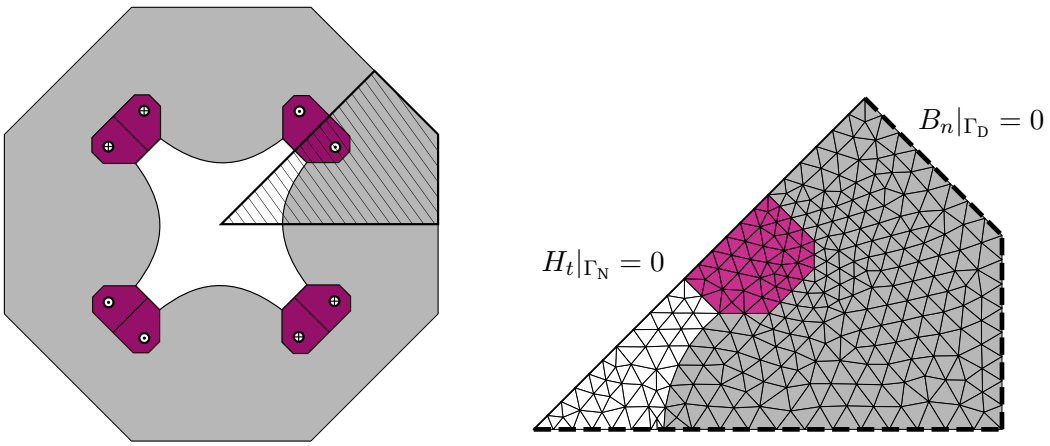

Figure 8.1: (a) 2D cross-section of a quadrupole magnet. The gray area shows the iron yoke, the purple area the coils, and the white area is vacuum. The marked area refers to the considered computational domain. (b) Illustration of a possible triangulation of the computational domain. Homogeneous Dirichlet (dashed boundary) and Neumann (solid boundary) BCs are considered.

(marked area) and 8.1b. The iron yoke is typically made out of soft magnetic materials, e.g., ARMCO® [19, 4]. Those materials exhibit a small hysteresis and are therefore frequently used in inductors, electrical machines, and other devices to reduce losses. This benefit comes at the cost of a strongly nonlinear magnetization curve, which is likely to be challenging for numerical solvers.

The validation strategy of the data-driven algorithm is now as follows. First, data convergence is shown when considering a linear material in the iron yoke. In the follow up, the algorithm's ability to handle strongly nonlinear materials is investigated. In both scenarios, the introduced hybrid approaches, see Section 4, are compared. Subsequently, an investigation is carried out on the local adaptively adjusted weighting factors. In all considered cases, the permeability in the vacuum part and the coil are considered to be exactly known with $\mu = \mu_0$. These two domains are thus handled in accordance to the chosen approaches introduced in Section 4. Moreover, we note that a convergence study with respect to the mesh size is omitted in this work, since numerical tests and theoretical considerations have already concluded that no notable difference in the data-driven solution is to be expected [69]. We can also confirm that conclusion, based on own numerical tests with the quadrupole magnet model.

8.1.1 Hybrid solver - nonlinear known material

We revisit the hybrid solver once more. However, for the following numerical experiments, we assume that the magnetization in the y-direction in the iron yoke is known. The linear response in the y-direction in the last numerical examples shall now be an approximation to the true nonlinear response. The linear approximation as well as the nonlinear model are shown in Figure 8.2a. The nonlinear BH-curve follows the Brauer model (**??**) with parameters $k_1 = 4\,\mathrm{m\,H^{-1}}, k_2 = 1.8\,\mathrm{T}^{-2}$, and $k_3 = 1000\,\mathrm{m\,H^{-1}}$. The minimization to the exact nonlinear material relation is now performed with the nearest neighbor algorithm, see Section 4.1. Thus, instead of updating the measurement states at the quadrature points with (4.5), minimization (4.2) is carried out at each quadrature point. Afterwards, the local weighting factors are updated with the known reluctivity.

For the simulation, adaptively adjusted weighting factors are employed, which allows us to compute a reliable result with a single starting value for the fixed-point iteration. To better assess the error contributions, we compute the energy mismatch error in the iron yoke separately for the x- and the y-direction with

$$\epsilon^2_{\mathrm{em},\Omega_{\mathrm{Fe}},r} = \frac{\|H^\circ_{h,r} - H_{h,r,\mathrm{ref}}\|^2_{L^2_{\mu_{r,\mathrm{ref}}}(\Omega_{\mathrm{Fe}})} + \|B^\circ_{h,r} - B_{h,r,\mathrm{ref}}\|^2_{L^2_{\nu_{r,\mathrm{ref}}}(\Omega_{\mathrm{Fe}})}}{\|H_{h,r,\mathrm{ref}}\|^2_{L^2_{\mu_{r,\mathrm{ref}}}(\Omega_{\mathrm{Fe}})} + \|B_{h,r,\mathrm{ref}}\|^2_{L^2_{\nu_{r,\mathrm{ref}}}(\Omega_{\mathrm{Fe}})}}, \tag{8.3}$$

where $r = \{x, y\}$ and Ω_{Fe} refers to the domain of the iron yoke. The global energy mismatch error ϵ_{em}, as well as the energy mismatch error in Ω_{Fe} for the x- and the y-direction are shown in Figure 8.2b over the amount of employed measurement data. We observe that all errors converge linearly with respect to the number of data points. Furthermore, the errors in x-, respectively y-direction, show only a minor difference, although the material relation in the y-direction is known. The dominating error is thus attributed to the finite measurement data that is employed in the x-direction. The number of data-driven iterations remains on the same level as in the example in Section **??**. However, if a strongly nonlinear material is utilized in the y-direction, e.g., the same relation as in the x-direction, the number of data-driven iterations increases noticeably. For instance, in the considered case, ≈ 21 iterations are necessary for convergence for $N = 10^4$. Conversely, if the material features a strongly nonlinear response, $\approx 10^3$ iterations are necessary for the same size of data set.

Summary

We may conclude that with the approach proposed in Section 4.1, nonlinear known material responses can be easily handled in the data-driven solver. However, for strongly

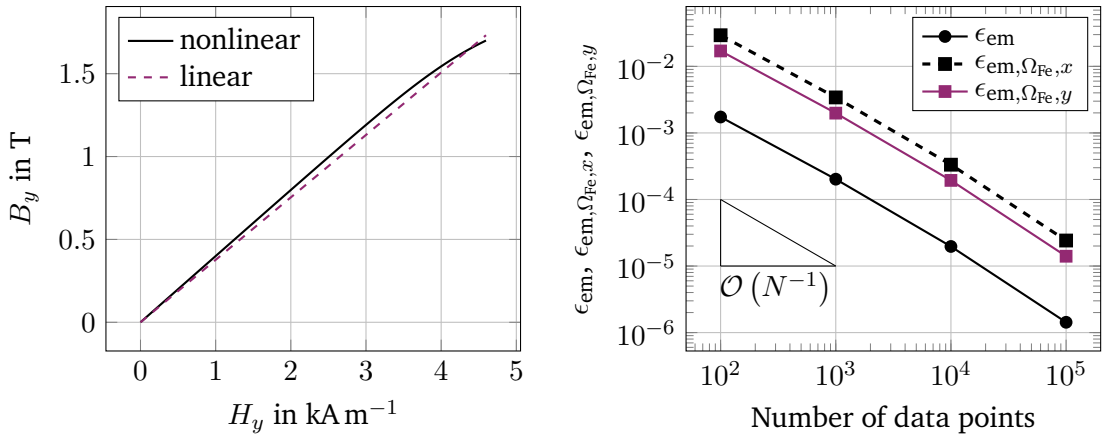

(a) (b)

Figure 8.2: (a) Nonlinear BH-curve in the y-direction and its linear approximation (dashed). (b) Convergence of the energy mismatch errors over the amount of employed data points N. The spatially dependent errors $\epsilon_{\text{em},\Omega_{\text{Fe}},x}$, respectively $\epsilon_{\text{em},\Omega_{\text{Fe}},y}$ show the energy mismatch error in the iron yoke.

nonlinear materials, the number of necessary data-driven iterations increases significantly. Furthermore, the overall costs of the data-driven solver increase since a minimization problem needs to be solved for each quadrature point, most likely with numerical methods.

8.2 DC-current electromagnet with real measurement data

With the next example, we want to address two major questions regarding the proposed data-driven solver. First, we want to analyze how the data-driven solvers scales with computationally demanding problems. Second, we will investigate the solution accuracy using real-world measurement data, which directly raises the question of whether and how a reference solution can be employed. These tasks will be carried out on a computationally demanding 3D DC-current electromagnet. This section closely follows [48]. The full 3D model of the electromagnet is depicted in Figure 8.3a, showing the iron-region in gray, the coil-region in purple, and the air-region in blue. The inductor is composed of an E-shaped iron yoke part $\Omega_{\text{Fe,E}}$, with a wire winding arranged inside. The coil region is denoted by Ω_{coil}. The magnetic circuit is closed by an I-shaped yoke part $\Omega_{\text{Fe,I}}$, but only up to an air gap of length ℓ_{air}, which defines the domain Ω_{air}. Further details about the geometrical

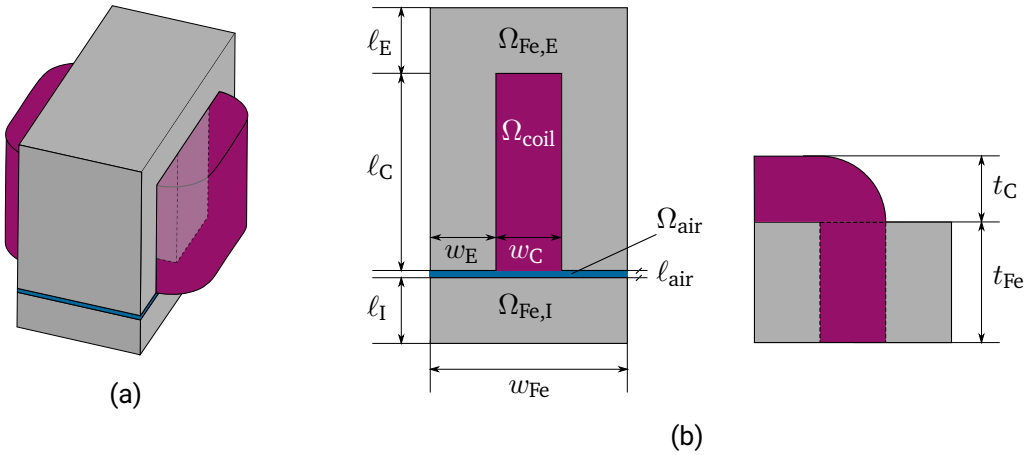

Figure 8.3: (a) Full model of the DC-current electromagnet with iron- (gray), coil- (purple) and air-region (blue) (b) 2D cross-section of the one-quarter of the electromagnet.

dimensions can be found in Table 8.1 and in Figure 8.3b. Additionally, the inductor is surrounded by a sphere filled with air, which is represented by the domain Ω_{sphere}. The sphere's radius is given by $r_s = 0.28\,\text{m}$.

By exploiting the electromagnet's symmetry, only one quarter of its geometry needs to be

Table 8.1: Geometrical dimensions of the inductor model.

quantity	value in mm
ℓ_E	30
ℓ_C	90
ℓ_I	30
ℓ_{air}	3.3
w_E	30
w_C	30
w_{Fe}	90
t_C	30
t_{Fe}	55

Table 8.2: Material properties and excitation.

quantity	value	units
k_1	10	$\text{m}\,\text{H}^{-1}$
k_2	1.8	T^{-2}
k_3	100	$\text{m}\,\text{H}^{-1}$
I	50	A
N_{coil}	66	–

simulated, which reduces the computational costs significantly. As a result, homogeneous Dirichlet BCs are applied to the symmetry-related boundaries. The 2D cross-section of the quarter is shown in Figure 8.3b. The magnetostatic problem is expressed through the vector potential **A**. Consequently, magnetic wall boundary conditions (i.e., homogeneous Dirichlet BCs) are applied to the sphere boundary. Since the radius of the sphere is approximately an order of magnitude larger than the inductor model, any introduced approximation error is negligible. After discretization, the domain contains 193311 tetrahedral elements, leading to 263627 DoFs, which can be decomposed into 230375 edges accounting for the DoFs for the vector potentials and 33252 accounting for the DoFs for the weak Coulomb gauge. Note that two systems of this size have to be solved in each data-driven iteration.

8.2.1 Artificial measurement data

The DC-electromagnet's iron part is considered to be isotropic and nonlinear. To model the nonlinearity of the iron part, we employ the already introduced Brauer model (**??**), yet for each dimension separately. The model parameters, the excitation, and the number of turns of the coil is found in Table 8.2. Drawing from the conclusion of Section 8.1, approach 1 handles the domains Ω_{coil} and Ω_{air}. Furthermore, adaptively adjusted weighting factors are employed, which allows us to simulate the problem for a single initial value. After creating measurement sets of increasing cardinality, the simulation is carried out to validate the data-driven solver for this three-dimensional problem.

The data convergence of the energy mismatch error ϵ_{em} and the relative error in the air gap ϵ_{air} are depicted in Figure 8.4a. The results unequivocally demonstrate that the data-driven solution converges towards the conventional solution as more measurement data are employed. As in the 2D case, a linear convergence rate for ϵ_{em} is achieved when adaptive weighting factors are utilized. The relative error in the air gap ϵ_{air} converges quadratically with respect to the number of data points. The convergence of the errors with respect to the necessary data-driven iterations is shown in Figure 8.4b. Again, as in the 2D case, only a moderate number of iterations is necessary until convergence is reached.

To assess the local accuracy of the data-driven solver, we examine the field solution for the magnetic flux density computed by the data-driven algorithm on a sequence of progressively larger data sets. The magnitude of the magnetic flux density $\mathbf{B}_h$ in the XY cross-section of the DC-electromagnet is depicted in Figure 8.5. From bottom to top, the amount of measurement data increases from $N = 10$ to $N = 100$. The top plot shows the field computed with the conventional solver and serves as a reference. On a qualitative level, we clearly observe that the data-driven solution becomes more accurate if the amount of measurement data is increased. For $N = 10$ a rather coarse solution is produced by

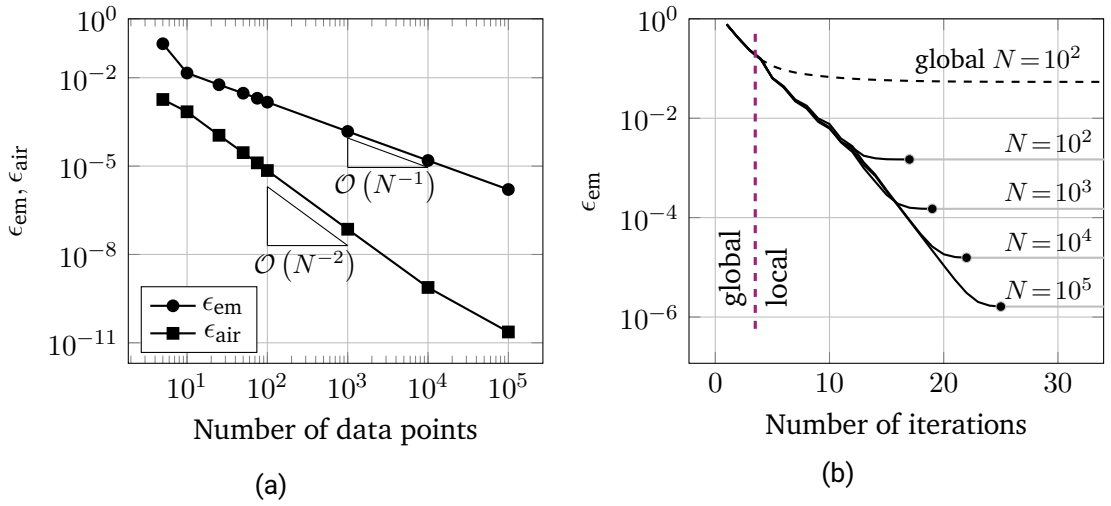

Figure 8.4: DC-electromagnet: The results have been computed with adaptively chosen weighting factors. (a) Energy mismatch error ϵ_{em} and relative error of the energy in the air gap ϵ_{air} over the number of employed measurement points. (b) Energy mismatch error ϵ_{em} over the number of data-driven iterations.

the data-driven solver, which is expected for such sparse measurement data. However, already for $N = 100$ data points, the difference between the data-driven solution and the reference solution is almost indistinguishable. We want to emphasize that the results do not show any local phenomena of the data-driven solver as sufficient measurement data are available. Figure 8.6 displays the magnitude of the difference between the magnetic flux densities. Again, the plot does not show any specific localized field error. Taking both field plots into account, for $N = 10$, the field solution is not adequately resolved, and the absolute field error is beyond standard engineering tolerances. However, depending on the requirements, the solution computed with $N \geq 50$ might already be sufficient for several problems in engineering or for a first understanding of the problem.

8.2.2 Real world measurement data

The strength of the data-driven solver lies in cases where no to little information about the material response is known. The only available information is given by discrete measurement data. Therefore, the subsequent simulation employs only a fixed amount of real-world measurement data. The iron yoke is therefore considered to be made from a

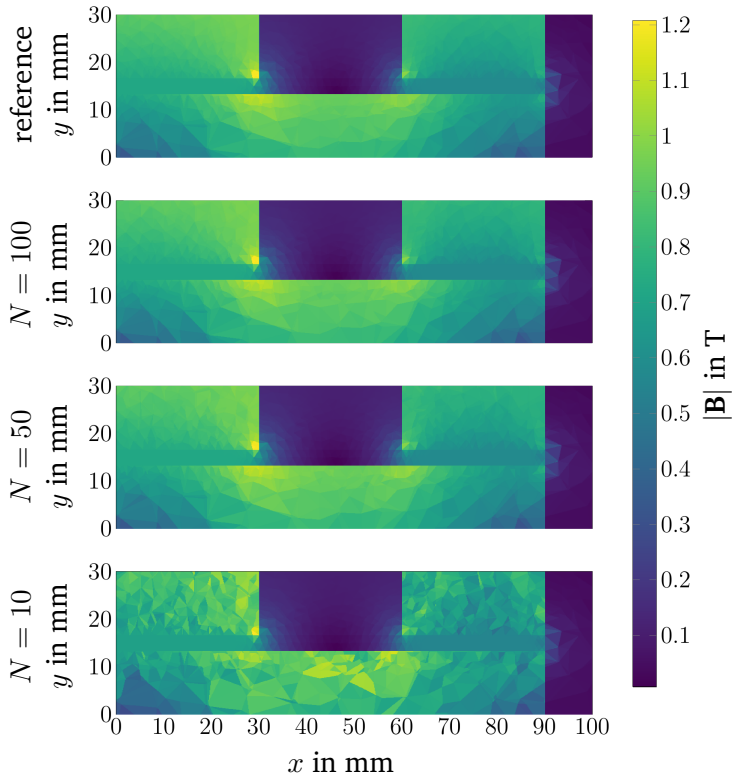

Figure 8.5: DC-electromagnet: Magnitude of the magnetic flux density $\mathbf{B}$ at the air gap. From top to bottom: reference solution and data-driven solutions computed with $N \in \{10, 50, 100\}$.

low-cost steel, called S355. The employed measurement data was gratefully supplied by [4]. In order to assess the performance of the data-driven solver, it is necessary to establish a conventional solver, i.e., a constitutive equation that suits the available data needs to be found. In general, if real world measurement data are considered, we usually have to take into account that the measurements are polluted by noise. With respect to the modeling problem, that means that standard interpolation techniques are most likely to fail. Even when regression techniques are considered, special care is necessary such that physical properties and numerical demands are satisfied. Contrarily, the distance-minimizing data-driven framework is highly sensitive to outliers in the measurement data set. Possible treatment of noisy data has been introduced in [70, 65]. However, since the available data are sparse (28 measurements) and the noise present in the data is negligible, we

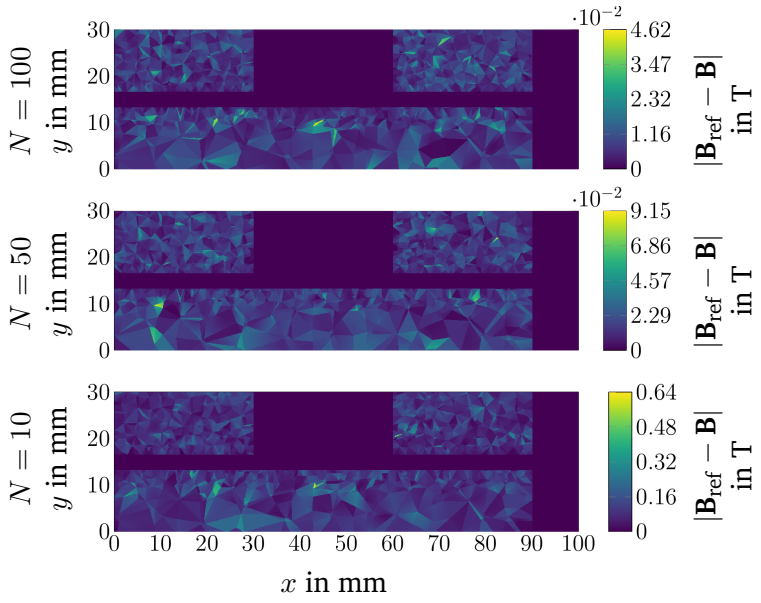

Figure 8.6

Figure 8.7: DC-electromagnet: Magnitude of the difference in the magnetic flux densities $\mathbf{B}$ between the reference solution and data-driven solutions computed with $N \in \{10, 50, 100\}$.

omit the introduction of the noisy data-driven solver. Instead we employ the standard distance-minimizing data-driven solver. Furthermore, the excitation current is set to $I = 40\,\text{A}$ such that the entire bandwidth of the available measurement data is employed.

We present two different material models which can be employed in the conventional solver. Those are the already introduced Brauer model (**??**) and an improved Brauer model [56]. The extended Brauer model improves the standard Brauer model in the Rayleigh region, as well as in the region of saturation. This is achieved by constructing a compound function for the three different areas, while enforcing differentiability at the connections. The two models as well as the available measurement data are depicted in Figure 8.8a. One clearly observes that the original Brauer model fails to model the Rayleigh part completely. Moreover, the steep linear part also shows a large difference to the measurement data, whereas the approximation is good in the saturation part. In contrast, the extended Brauer model captures the Rayleigh part and provides a better fit in the steep linear part. Judging from the plot, both approaches provide a similarly

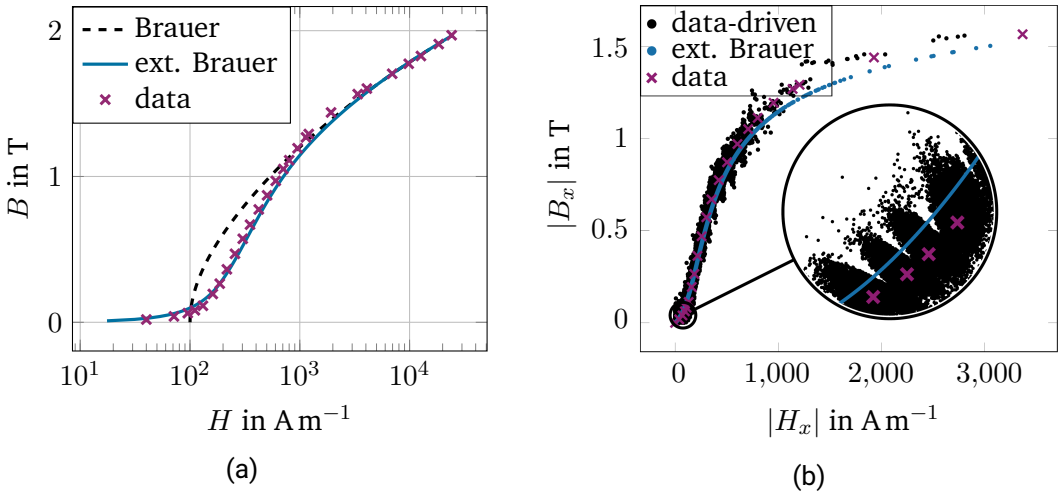

Figure 8.8: DC-electromagnet: (a) Measurement data (purple crosses) of the S355 sample, Brauer model (dashed blue line) and extended Brauer model (solid black line). (b) Solution of the data-driven solver (blue dots) and the conventional solver (black dots) at the quadrature points that are compatible with magnetostatics. The measurement data are depicted by the purple crosses.

good approximation of the saturation part. In summary, both models show approximation errors, which can be attributed to the sparse data set and the considered model choice. Unlike conventional solvers, which require a modeling procedure, the data-driven solvers bypasses this step and can be used directly.

Since we started directly from measurement data, no reference solution is available. As a first step, we analyze both methods qualitatively. Figure 8.8b shows exemplarily the magnitude of the magnetic field strength and magnetic flux density in the x-direction at the quadrature points. The available measurement data are shown by purple crosses, the solution obtained with the conventional solver utilizing the extended Brauer model by blue dots, and the data-driven solution by black dots. At first glance, we observe that the data-driven solution clusters around the sparse measurement data. This can be expected as only 28 measurement points are available. Nevertheless, the clusters are around the available measurement data in all regions of the BH-curve. While the conventional solution exhibits a good agreement in the steep linear part, it is comparatively less accurate in the Rayleigh region and in the transition region between the linear and saturation regions. We conclude that both methods suffer from the sparse data set, albeit differently.

A quantitative comparison is carried out by computing the energy mismatch from the two solutions to the available measurement data, i.e., we compute

$$\epsilon^2_{\text{em,data}} = \|\mathbf{H}_h - \mathbf{H}_h^{\times}\|^2_{L^2_{\boldsymbol{\mu}_{\text{ext.Brauer}}}(\Omega_{\text{Fe}})} + \|\mathbf{B}_h - \mathbf{B}_h^{\times}\|^2_{L^2_{\boldsymbol{\nu}_{\text{ext.Brauer}}}(\Omega_{\text{Fe}})}, \tag{8.4}$$

where the permeability and reluctivity are obtained from the extended Brauer model and $(\mathbf{H}_h^{\times}, \mathbf{B}_h^{\times})$ are the measurement states that minimize (3.25a) for the given solutions. The energy mismatch (8.4) for the data-driven solution is $\epsilon_{\text{em,data}} = 2.9 \cdot 10^{-4}\,\mathrm{W\,s}$, while the corresponding error for the conventional solution is $\epsilon_{\text{em,data}} = 3.9 \cdot 10^{-4}\,\mathrm{W\,s}$. The results indicate that both approaches exhibit comparable accuracy. The magnetic energy in the air gap amounts for $0.8755\,\mathrm{W\,s}$ for the data-driven solver and for $0.8685\,\mathrm{W\,s}$ for the conventional solver using the extended Brauer model.

Summary

Given the very sparse measurement data, the data-driven and the conventional solver deliver acceptable solutions. However, the conventional solver strongly benefits from the effort and research that has already been spent to find an appropriate model relation for the given material. Contrarily, the data-driven solver disregards the model and yields an assumption-free solution. Given these results, it is reasonable to conclude that the data-driven solver may be the superior approach in scenarios where complex materials are utilized and there is limited modeling information available.

9 Appendix

9.1 Hybrid solver - Euler-Lagrange

9.1.1 Stationary solution to the Lagrangian of Section 4.2

The Euler-Lagrange equation in the domain with data-driven material Ω_{dd} reads

$$\frac{\partial}{\partial \mathbf{A}}: \quad -\mathbf{curl}\left\{\tilde{\nu}\mathbf{curl}\,\mathbf{A}-\tilde{\nu}\mathbf{B}^{\times}\right\}=0 \qquad \text{in } \Omega_{\mathrm{dd}}, \tag{9.1a}$$

$$\Longleftrightarrow \qquad \mathbf{curl}\left(\tilde{\nu}\mathbf{curl}\,\mathbf{A}\right)=\mathbf{curl}\left(\tilde{\nu}\mathbf{B}^{\times}\right) \qquad \text{in } \Omega_{\mathrm{dd}}, \tag{9.1b}$$

$$\frac{\partial}{\partial \mathbf{H}}: \quad \tilde{\mu}\mathbf{H}-\tilde{\mu}\mathbf{H}^{\times}+\mathbf{curl}\,\boldsymbol{\eta}=0 \qquad \text{in } \Omega_{\mathrm{dd}}, \tag{9.1c}$$

$$\Longleftrightarrow \qquad \mathbf{H}+\tilde{\nu}\mathbf{curl}\,\boldsymbol{\eta}=\mathbf{H}^{\times} \qquad \text{in } \Omega_{\mathrm{dd}}. \tag{9.1d}$$

In the domains with known material relation, the stationary solution is given by

$$\frac{\partial}{\partial \mathbf{A}}: \quad -\mathbf{curl}\left\{\nu\mathbf{curl}\,\mathbf{A}-\mu\nu\mathbf{H}\right\}=0 \quad \text{in } \Omega_{\mathrm{ex}}, \tag{9.2a}$$

$$\Longleftrightarrow \qquad \mathbf{curl}\left(\nu\mathbf{curl}\,\mathbf{A}\right)-\mathbf{curl}\,\mathbf{H}=0 \quad \text{in } \Omega_{\mathrm{ex}}, \tag{9.2b}$$

$$\frac{\partial}{\partial \mathbf{H}}: \quad -\mu\nu\mathbf{curl}\,\mathbf{A}+\mu\nu\mu\mathbf{H}+\mathbf{curl}\,\boldsymbol{\eta}=0 \quad \text{in } \Omega_{\mathrm{ex}}, \tag{9.2c}$$

$$\Longleftrightarrow \qquad \mathbf{H}+\nu\mathbf{curl}\left(\boldsymbol{\eta}-\mathbf{A}\right)=0 \quad \text{in } \Omega_{\mathrm{ex}}. \tag{9.2d}$$

Applying the curl operator on (9.1d) and (9.2d) yields

$$\mathbf{curl}\,\mathbf{H}+\mathbf{curl}\left(\tilde{\nu}\mathbf{curl}\,\boldsymbol{\eta}\right)=\mathbf{curl}\,\mathbf{H}^{\times} \qquad \text{in } \Omega_{\mathrm{dd}}, \tag{9.3a}$$

$$\mathbf{curl}\left(\nu\mathbf{curl}\,\mathbf{A}\right)-\mathbf{curl}\,\mathbf{H}=\mathbf{curl}\left(\nu\mathbf{curl}\,\boldsymbol{\eta}\right) \quad \text{in } \Omega_{\mathrm{ex}}. \tag{9.3b}$$

Further inserting (9.3b) in (9.2b) leads to

$$\mathbf{curl}\left(\nu\mathbf{curl}\,\boldsymbol{\eta}\right)=0 \quad \text{in } \Omega_{\mathrm{ex}}, \tag{9.4}$$

in the domain with exactly known material relation. To obtain the solution in the entire domain, we combine (9.4) with (9.1b), which yields

$$\mathbb{1}_{\Omega_{\text{dd}}}\mathbf{curl}\,\left(\tilde{\boldsymbol{\nu}}\mathbf{curl}\,\mathbf{A}\right)+\mathbb{1}_{\Omega_{\text{ex}}}\mathbf{curl}\,\left(\boldsymbol{\nu}\mathbf{curl}\,\boldsymbol{\eta}\right)=\mathbb{1}_{\Omega_{\text{dd}}}\mathbf{curl}\,\left(\tilde{\nu}\mathbf{B}^{\times}\right) \tag{9.5}$$

Further combining (9.3a) with (9.3b) and utilizing Ampère's law $\mathbf{J}=\mathbf{curl}\,\mathbf{H}$ to replace the unknown field $\mathbf{H}$ we obtain

$$\begin{aligned}&\mathbb{1}_{\Omega_{\text{dd}}}\mathbf{J}+\mathbb{1}_{\Omega_{\text{ex}}}\mathbf{J}+\mathbb{1}_{\Omega_{\text{dd}}}\mathbf{curl}\,\left(\tilde{\boldsymbol{\nu}}\mathbf{curl}\,\boldsymbol{\eta}\right)+\mathbb{1}_{\Omega_{\text{ex}}}\mathbf{curl}\,\left(\boldsymbol{\nu}\mathbf{curl}\,\boldsymbol{\eta}\right)-\mathbb{1}_{\Omega_{\text{ex}}}\mathbf{curl}\,\left(\boldsymbol{\nu}\mathbf{curl}\,\mathbf{A}\right)=\mathbb{1}_{\Omega_{\text{dd}}}\mathbf{H}^{\times}\\ \Longleftrightarrow\;&\mathbb{1}_{\Omega_{\text{ex}}}\mathbf{curl}\,\left(\boldsymbol{\nu}\mathbf{curl}\,\mathbf{A}\right)-\mathbb{1}_{\Omega_{\text{ex}}}\mathbf{curl}\,\left(\boldsymbol{\nu}\mathbf{curl}\,\boldsymbol{\eta}\right)-\mathbb{1}_{\Omega_{\text{dd}}}\mathbf{curl}\,\left(\tilde{\boldsymbol{\nu}}\mathbf{curl}\,\boldsymbol{\eta}\right)=\mathbf{J}-\mathbb{1}_{\Omega_{\text{dd}}}\mathbf{H}^{\times}\end{aligned} \tag{9.6}$$

9.1.2 Stationary solution to the Lagrangian of Section 4.3

The Euler-Lagrange equation in the domain with data-driven material Ω_{dd} reads

$$\begin{aligned}\frac{\partial}{\partial\mathbf{A}}:\quad&-\mathbf{curl}\,\left\{\tilde{\boldsymbol{\nu}}\mathbf{curl}\,\mathbf{A}-\tilde{\nu}\mathbf{B}^{\times}\right\}=0 && \text{in }\Omega_{\text{dd}}, && \text{(9.7a)}\\ \Longleftrightarrow\quad&\mathbf{curl}\,\left(\tilde{\boldsymbol{\nu}}\mathbf{curl}\,\mathbf{A}\right)=\mathbf{curl}\,\left(\tilde{\boldsymbol{\nu}}\mathbf{B}^{\times}\right) && \text{in }\Omega_{\text{dd}}, && \text{(9.7b)}\\ \frac{\partial}{\partial\mathbf{H}}:\quad&\tilde{\boldsymbol{\mu}}\mathbf{H}-\tilde{\boldsymbol{\mu}}\mathbf{H}^{\times}+\mathbf{curl}\,\boldsymbol{\eta}=0 && \text{in }\Omega_{\text{dd}}, && \text{(9.7c)}\\ \Longleftrightarrow\quad&\mathbf{H}+\tilde{\boldsymbol{\nu}}\mathbf{curl}\,\boldsymbol{\eta}=\mathbf{H}^{\times} && \text{in }\Omega_{\text{dd}}. && \text{(9.7d)}\end{aligned}$$

In the domains with known material relation, the stationary solution is given by

$$\begin{aligned}\frac{\partial}{\partial\mathbf{A}}:\quad&-\mathbf{curl}\,\left(\boldsymbol{\nu}\mathbf{curl}\,\boldsymbol{\eta}\right)=0 \quad \text{in }\Omega_{\text{ex}}, && \text{(9.8a)}\\ \frac{\partial}{\partial\mathbf{H}}:\quad&\mathbf{curl}\,\boldsymbol{\eta}=0 \quad \text{in }\Omega_{\text{ex}}, && \text{(9.8b)}\end{aligned}$$

where we employed the Euler-Lagrange equation

$$\frac{\partial\mathcal{L}}{\partial\mathbf{A}}-\mathbf{curl}\,\left\{\frac{\partial\mathcal{L}}{\partial\mathbf{curl}\,\mathbf{A}}\right\}+\mathbf{curl}\,\mathbf{curl}\,\left\{\frac{\partial\mathcal{L}}{\partial\mathbf{curl}\,\mathbf{curl}\,\mathbf{A}}\right\}=0, \tag{9.9}$$

see, for instance, [105]. Combining (9.7b) with (9.8a) and additionally employing the constraint $\mathbf{J} = \mathbf{curl}\,(\boldsymbol{\nu}\mathbf{curl}\,\mathbf{A})$ for $\mathbf{x} \in \Omega_{\mathrm{ex}}$ together with (9.7d) we obtain

$$\mathbb{1}_{\Omega_{\mathrm{dd}}}\mathbf{curl}\,(\tilde{\boldsymbol{\nu}}\mathbf{curl}\,\mathbf{A}) + \mathbb{1}_{\Omega_{\mathrm{ex}}}\mathbf{curl}\,(\boldsymbol{\nu}\mathbf{curl}\,\boldsymbol{\nu}) = \mathbb{1}_{\Omega_{\mathrm{dd}}}\mathbf{curl}\,\left(\tilde{\boldsymbol{\nu}}\mathbf{B}^{\times}\right), \tag{9.10a}$$

$$\mathbb{1}_{\Omega_{\mathrm{ex}}}\mathbf{curl}\,(\boldsymbol{\nu}\mathbf{curl}\,\mathbf{A}) - \mathbb{1}_{\Omega_{\mathrm{dd}}}\mathbf{curl}\,(\tilde{\boldsymbol{\nu}}\mathbf{curl}\,\boldsymbol{\eta}) = \mathbf{J} - \mathbb{1}_{\Omega_{\mathrm{dd}}}\mathbf{curl}\,\mathbf{H}^{\times}. \tag{9.10b}$$

Bibliography

[1] Mark Ainsworth and J. Tinsley Oden. “A posteriori error estimation in finite element analysis”. In: *Computer methods in applied mechanics and engineering* 142.1-2 (1997), pp. 1–88.

[2] Piergiorgio Alotto and Ilaria Perugia. “A field-based finite element method for magnetostatics derived from an error minimization approach”. In: *International Journal for Numerical Methods in Engineering* 49.4 (2000), pp. 573–598.

[3] Piergiorgio Alotto et al. “A mixed face-edge finite element formulation for 3D magnetostatic problems”. In: *IEEE Transactions on Magnetics* 34.5 (1998), pp. 2445–2448. DOI: 10.1109/20.717562.

[4] Jaime R. Anglada et al. “Characterization of Magnetic Steels for the FCC-ee Magnet Prototypes”. In: *2020 IEEE International Instrumentation and Measurement Technology Conference (I2MTC)*. 2020, pp. 1–6. DOI: 10.1109/I2MTC43012.2020.9129153.

[5] Douglas N. Arnold, Richard S. Falk, and Ragnar Winther. “Finite element exterior calculus, homological techniques, and applications”. In: *Acta numerica* 15 (2006), pp. 1–155.

[6] Jacobo Ayensa–Jiménez et al. “A new reliability-based data-driven approach for noisy experimental data with physical constraints”. In: *Computer Methods in Applied Mechanics and Engineering* 328 (2018), pp. 752–774.

[7] Bahador Bahmani and WaiChing Sun. “A kd-tree-accelerated hybrid data-driven/model-based approach for poroelasticity problems with multi-fidelity multi-physics data”. In: *Computer Methods in Applied Mechanics and Engineering* 382 (2021), p. 113868.

[8] Xiaowei Bai et al. “A data-driven approach for instability analysis of thin composite structures”. In: *Computers & Structures* 273 (2022), p. 106898.

[9] Andreas Bartel et al. “Influence of measurement errors on transformer inrush currents using different material models”. In: *IEEE transactions on magnetics* 50.2 (2014), pp. 485–488.

[10] Thorsten Bartel et al. “Aspects of accuracy and uniqueness of solutions in data-driven mechanics”. In: *PAMM* 22.1 (2023), e202200206.

[11] Jon Louis Bentley. “Multidimensional Binary Search Trees Used for Associative Searching”. In: *Commun. ACM* 18.9 (Sept. 1975), pp. 509–517. DOI: 10.1145/361002.361007.

[12] Michele Benzi, Gene H. Golub, and Jörg Liesen. “Numerical solution of saddle point problems”. In: *Acta Numerica* 14 (2005), pp. 1–137. DOI: 10.1017/S0962492904000212.

[13] Alfredo Bermúdez, Rodolfo Rodríguez, and Pilar Salgado. “A finite element method for the magnetostatic problem in terms of scalar potentials”. In: *SIAM Journal on Numerical Analysis* 46.3 (2008), pp. 1338–1363.

[14] Alain Bossavit. “A rationale for ‘edge-elements’ in 3-D fields computations”. In: *IEEE Transactions on Magnetics* 24.1 (1988), pp. 74–79. DOI: 10.1109/20.43860.

[15] Alain Bossavit. “Whitney forms: a class of finite elements for three-dimensional computations in electromagnetism”. In: *IEE Proceedings A (Physical Science, Measurement and Instrumentation, Management and Education, Reviews)* 135 (8 1988), 493–500(7). ISSN: 0143-702X.

[16] Alain Bossavit. Ed. by Alain Bossavit. Electromagnetism. San Diego: Academic Press, 1998, pp. 1–30. ISBN: 978-0-12-118710-1. DOI: 10.1016/B978-012118710-1/50002-7.

[17] Alain Bossavit. “How weak is the ‘weak solution’ in finite element methods?” In: *IEEE Transactions on Magnetics* 34.5 (1998), pp. 2429–2432. DOI: 10.1109/20.717558.

[18] George E. P. Box. “Science and statistics”. In: *Journal of the American Statistical Association* 71.356 (1976), pp. 791–799.

[19] Beatriz Brañas et al. “Design and manufacturing of the combined quadrupole and corrector magnets for the LIPAc accelerator high energy beam transport line”. In: *Nuclear Fusion* 62.8 (2022), p. 086024.

[20] John R. Brauer. “Simple equations for the magnetization and reluctivity curves of steel”. In: *IEEE Transactions on Magnetics* 11.1 (1975), pp. 81–81.

[21] Susanne C. Brenner and Larkin R. Scott. *The Mathematical Theory of Finite Element Methods*. Vol. 15. Texts in Applied Mathematics. Springer, 2008. DOI: 10.1007/978-0-387-75934-0.

[22] Franco Brezzi et al. “A novel field-based mixed formulation of magnetostatics”. In: *IEEE Transactions on Magnetics* 32.3 (1996), pp. 635–638. DOI: 10.1109/20.497318.

[23] Jonas Bundschuh, M. Greta Ruppert, and Yvonne Späck-Leigsnering. “Pyrit: A Finite Element Based Field Simulation Software Written in Python”. In: *arXiv preprint arXiv:2210.11983* (2022).

[24] David Burg and Jesse H. Ausubel. “Moore’s Law revisited through Intel chip density”. In: *PloS one* 16.8 (2021), e0256245.

[25] Pietro Carrara et al. “Data-driven fracture mechanics”. In: *Computer Methods in Applied Mechanics and Engineering* 372 (2020), p. 113390. DOI: 10.1016/j.cma.2020.113390.

[26] Philippe G. Ciarlet. *The Finite Element Method for Elliptic Problems*. Society for Industrial and Applied Mathematics, 2002. DOI: 10.1137/1.9780898719208.

[27] Markus Clemens and Thomas Weiland. “Transient eddy-current calculation with the FI-method”. In: *IEEE Transactions on Magnetics* 35.3 (1999), pp. 1163–1166. DOI: 10.1109/20.767155.

[28] Jean Philippe Combe, Pierre Ladèveze, and Jean Pierre Pelle. “Constitutive relation error estimator for transient finite element analysis”. In: *Computer methods in applied mechanics and engineering* 176.1-4 (1999), pp. 165–185.

[29] Sergio Conti, Franca Hoffmann, and Michael Ortiz. “Model-Free and Prior-Free Data-Driven Inference in Mechanics”. In: *Archive for Rational Mechanics and Analysis* 247.1 (2023), p. 7.

[30] Sergio Conti, Stefan Müller, and Michael Ortiz. “Data-driven problems in elasticity”. In: *Archive for Rational Mechanics and Analysis* 229.1 (2018), pp. 79–123.

[31] Sergio Conti, Stefan Müller, and Michael Ortiz. “Data-Driven Finite Elasticity”. In: *Archive for Rational Mechanics and Analysis* (2020), pp. 1–33.

[32] Bruno Cornut, Afef Kedous-Lebouc, and Thierry Waeckerlé. “From metallurgy to modelling of electrical steels: A multiple approach to their behaviour and use based on physics and experimental investigations”. In: *Journal of Magnetism and Magnetic Materials* 160 (1996), pp. 102–108.

[33] Emmanuel Creusé, Patrick Dular, and Serge Nicaise. “About the gauge conditions arising in Finite Element magnetostatic problems”. In: *Computers & Mathematics with Applications* 77.6 (2019). 7th International Conference on Advanced Computational Methods in Engineering (ACOMEN 2017), pp. 1563–1582. DOI: 10.1016/j.camwa.2018.06.030.

[34] Laurent Daniel et al. “Reversible magneto-elastic behavior: A multiscale approach”. In: *Journal of the Mechanics and Physics of Solids* 56.3 (2008), pp. 1018–1042.

[35] Herbert De Gersem, Irina Munteanu, and Thomas Weiland. “Construction of Differential Material Matrices for the Orthogonal Finite-Integration Technique With Nonlinear Materials”. In: *IEEE Transactions on Magnetics* 44.6 (2008), pp. 710–713.

[36] Herbert De Gersem et al. “Magnetic Field Simulation with Data-Driven Material Modeling”. In: *IEEE Transactions on Magnetics* 56.8 (2020), pp. 1–6. DOI: 10.1109/TMAG.2020.3002092.

[37] E. Du Trémolet de Lacheisserie, D. Gignoux, and M. Schlenker. *Magnetism I - Fundamentals*. Springer Science+Business Media, 2002.

[38] Patrick Dular and Francis Piriou. “Static Formulations: Electrostatic, Electrokinetic, Magnetostatics”. In: *The Finite Element Method for Electromagnetic Modeling*. John Wiley & Sons, Ltd, 2008. Chap. 2, pp. 69–116. DOI: 10.1002/9780470611173.ch2.

[39] Patrick Dular et al. “A discrete sequence associated with mixed finite elements and its gauge condition for vector potentials”. In: *IEEE Transactions on Magnetics* 31.3 (May 1995), pp. 1356–1359. DOI: 10.1109/20.376278.

[40] Patrick Dular et al. “Magnetostatic and magnetodynamic mixed formulations compared with conventional formulations”. In: *IEEE Transactions on Magnetics* 33.2 (1997), pp. 1302–1305. DOI: 10.1109/20.582494.

[41] Robert Eggersmann et al. “Model-free data-driven inelasticity”. In: *Computer Methods in Applied Mechanics and Engineering* 350 (2019), pp. 81–99.

[42] Robert Eggersmann et al. “Efficient data structures for model-free data-driven computational mechanics”. In: *Computer Methods in Applied Mechanics and Engineering* 382 (2021), p. 113855.

[43] Robert Eggersmann et al. “Model-free data-driven computational mechanics enhanced by tensor voting”. In: *Computer Methods in Applied Mechanics and Engineering* 373 (2021), p. 113499.

[44] Lawrence C. Evans. *Partial differential equations*. Providence, R.I.: American Mathematical Society, 2010.

[45] Paolo Fernandes and Ilaria Perugia. “Vector potential formulation for magnetostatics and modelling of permanent magnets”. In: *IMA Journal of Applied Mathematics* 66.3 (2001), pp. 293–318. DOI: 10.1093/imamat/66.3.293.

[46] Felix Fritzen and Matthias Leuschner. “Reduced basis hybrid computational homogenization based on a mixed incremental formulation”. In: *Computer Methods in Applied Mechanics and Engineering* 260 (2013), pp. 143–154.

[47] Armin Galetzka, Dimitrios Loukrezis, and Herbert De Gersem. “Data-driven solvers for strongly nonlinear material response”. In: *International Journal for Numerical Methods in Engineering* 122.6 (2021), pp. 1538–1562. DOI: 10.1002/nme.6589.

[48] Armin Galetzka, Dimitrios Loukrezis, and Herbert De Gersem. “Three-dimensional data-driven magnetostatic field computation using real-world measurement data”. In: *COMPEL-The international journal for computation and mathematics in electrical and electronic engineering* 41.2 (2022), pp. 615–627. DOI: 10.1108/COMPEL-06-2021-0219.

[49] Hans-Otto Georgii. *Stochastics: introduction to probability theory and statistics*. de Gruyter Lehrbuch, 2nd edn. Walter de Gruyter, Berlin, 2012.

[50] Aristides Gionis, Piotr Indyk, and Rajeev Motwani. “Similarity Search in High Dimensions via Hashing”. In: *Proceedings of the 25th International Conference on Very Large Data Bases*. VLDB ’99. San Francisco, CA, USA: Morgan Kaufmann Publishers Inc., 1999, pp. 518–529. ISBN: 1558606157.

[51] David González et al. “kPCA-based parametric solutions within the PGD framework”. In: *Archives of Computational Methods in Engineering* 25 (2018), pp. 69–86.

[52] Philip J Hasnip et al. “Density functional theory in the solid state”. In: *Philosophical Transactions of the Royal Society A: Mathematical, Physical and Engineering Sciences* 372.2011 (2014), p. 20130270.

[53] John R. Hauser. *Numerical Methods for Nonlinear Engineering Models*. Springer Netherlands, 2009.

[54] Bodo Heise. “Analysis of a Fully Discrete Finite Element Method for a Nonlinear Magnetic Field Problem”. In: *SIAM Journal on Numerical Analysis* 31.3 (1994), pp. 745–759. DOI: 10.1137/0731040.

[55] Thomas J.R. Hughes, John A. Cottrell, and Yuri Bazilevs. “Isogeometric analysis: CAD, finite elements, NURBS, exact geometry and mesh refinement”. In: *Computer methods in applied mechanics and engineering* 194.39-41 (2005), pp. 4135–4195.

[56] Timo Hülsmann et al. “Extended Brauer Model for Ferromagnetic Materials: Analysis and Computation”. In: *COMPEL: The International Journal for Computation and Mathematics in Electrical and Electronic Engineering* 4 (2014), pp. 1251–1263. ISSN: 0332-1649.

[57] Rubén Ibanez et al. “A manifold learning approach to data-driven computational elasticity and inelasticity”. In: *Archives of Computational Methods in Engineering* 25.1 (2018), pp. 47–57.

[58] Ruben Ibañez et al. “Data-driven non-linear elasticity: constitutive manifold construction and problem discretization”. In: *Computational Mechanics* 60 (2017), pp. 813–826.

[59] Rubén Ibáñez et al. “Hybrid constitutive modeling: data-driven learning of corrections to plasticity models”. In: *International Journal of Material Forming* 12 (2019), pp. 717–725.

[60] John David Jackson. *Classical Electrodynamics*. 3rd ed. New York, NY: Wiley, 1998. ISBN: 978-0-471-30932-1.

[61] Radoslav Jankoski, Ulrich Römer, and Sebastian Schöps. “Modeling of spatial uncertainties in the magnetic reluctivity”. In: *COMPEL - The international journal for computation and mathematics in electrical and electronic engineering* 36.4 (2017), pp. 1151–1167. DOI: 10.1108/COMPEL-10-2016-0438.

[62] Jan Jaśkowiec and Natarajan Sukumar. “High-order cubature rules for tetrahedra”. In: *International Journal for Numerical Methods in Engineering* 121.11 (2020), pp. 2418–2436. DOI: 10.1002/nme.6313.

[63] Alan R. Jones. *Probability, statistics and other frightening stuff*. Routledge, 2018.

[64] Akihisa Kameari and Koichi Koganezawa. “Convergence of ICCG method in FEM using edge elements without gauge condition”. In: *IEEE Transactions on Magnetics* 33.2 (1997), pp. 1223–1226. DOI: 10.1109/20.582474.

[65] Yoshihiro Kanno. “Simple heuristic for data-driven computational elasticity with material data involving noise and outliers: a local robust regression approach”. In: *Japan Journal of Industrial and Applied Mathematics* 35.3 (2018), pp. 1085–1101.

[66] Yoshihiro Kanno. “Mixed-integer programming formulation of a data-driven solver in computational elasticity”. In: *Optimization Letters* 13 (2019), pp. 1505–1514.

[67] Yoshihiro Kanno. “A kernel method for learning constitutive relation in data-driven computational elasticity”. In: *Japan Journal of Industrial and Applied Mathematics* 38 (2021), pp. 39–77.

[68] Robert C. Kirby et al. “Common and unusual finite elements”. In: *Automated Solution of Differential Equations by the Finite Element Method: The FEniCS Book*. Ed. by Anders Logg, Kent-Andre Mardal, and Garth Wells. Berlin, Heidelberg: Springer Berlin Heidelberg, 2012, pp. 95–119. DOI: 10.1007/978-3-642-23099-8_3.

[69] Trenton Kirchdoerfer and Michael Ortiz. “Data-driven computational mechanics”. In: *Computer Methods in Applied Mechanics and Engineering* 304 (2016), pp. 81–101. DOI: 10.1016/j.cma.2016.02.001.

[70] Trenton Kirchdoerfer and Michael Ortiz. “Data Driven Computing with noisy material data sets”. In: *Computer Methods in Applied Mechanics and Engineering* 326 (2017), pp. 622–641. DOI: 10.1016/j.cma.2017.07.039.

[71] Trenton Kirchdoerfer and Michael Ortiz. “Data-driven computing in dynamics”. In: *International Journal for Numerical Methods in Engineering* 113.11 (2018), pp. 1697–1710.

[72] Dominik K. Klein et al. “Finite electro-elasticity with physics-augmented neural networks”. In: *Computer Methods in Applied Mechanics and Engineering* 400 (2022), p. 115501. DOI: 10.1016/j.cma.2022.115501.

[73] Louis Komzsik. *Applied calculus of variations for engineers*. CRC Press, 2019.

[74] Tim Fabian Korzeniowski and Kerstin Weinberg. “A multi-level method for data-driven finite element computations”. In: *Computer Methods in Applied Mechanics and Engineering* 379 (2021). DOI: 10.1016/j.cma.2021.113740.

[75] Zengtao Kuang et al. “Data-driven computational framework for snap-through problems”. In: *International Journal of Solids and Structures* (2023), p. 112226.

[76] Stefan Kurz et al. “Hybrid modeling: towards the next level of scientific computing in engineering”. In: *Journal of Mathematics in Industry* 12.1 (2022), p. 8. DOI: 10.1186/s13362-022-00123-0.

[77] Pierre Ladeveze and Dominique Leguillon. “Error estimate procedure in the finite element method and applications”. In: *SIAM Journal on Numerical Analysis* 20.3 (1983), pp. 485–509.

[78] Adrien Leygue et al. “Data-based derivation of material response”. In: *Computer Methods in Applied Mechanics and Engineering* 331 (2018), pp. 184–196.

[79] Daniel Liberzon. *Calculus of variations and optimal control theory: a concise introduction*. Princeton university press, 2011.

[80] Dennis A. Lindholm. “Notes on boundary integral equations for three-dimensional magnetostatics”. In: *IEEE Transactions on Magnetics* 16.6 (1980), pp. 1409–1413. DOI: 10.1109/TMAG.1980.1060887.

[81] Wing Kam Liu, Shaofan Li, and Harold S Park. “Eighty years of the finite element method: Birth, evolution, and future”. In: *Archives of Computational Methods in Engineering* 29.6 (2022), pp. 4431–4453.

[82] Eduard Marenić, Guillem Seychal, and Jean-Charles Passieux. “Data driven approach in multiphysics framework: application to coupled electro-mechanical problems”. In: *Computer Methods in Applied Mechanics and Engineering* 395 (2022), p. 114959.

[83] Isaak D. Mayergoyz. “Boundary integral equations of minimum order for the calculation of three-dimensional eddy current problems”. In: *IEEE Transactions on Magnetics* 18.2 (1982), pp. 536–539. DOI: 10.1109/TMAG.1982.1061855.

[84] Isaak D. Mayergoyz, Madabushi V. K. Chari, and Judy D’Angelo. “A new scalar potential formulation for three-dimensional magnetostatic problems”. In: *IEEE transactions on magnetics* 23.6 (1987), pp. 3889–3894.

[85] Christian Meyer and Annika Müller. “Finite Element approximation of data-driven problems in conductivity”. In: *arXiv preprint arXiv:2303.05840* (2023).

[86] Peter Monk et al. *Finite element methods for Maxwell’s equations*. Oxford University Press, 2003.

[87] Jean-Claude Nédélec. “Mixed finite elements in $\mathbb{R}^3$”. In: *Numerische Mathematik* 35.3 (1980), pp. 315–341. DOI: 10.1007/BF01396415.

[88] Lu Trong Khiem Nguyen, Roland Can Aydin, and Christian Johannes Cyron. “Accelerating the distance-minimizing method for data-driven elasticity with adaptive hyperparameters”. In: *Computational Mechanics* 70.3 (Sept. 2022), pp. 621–638. DOI: 10.1007/s00466-022-02183-w.

[89] Lu Trong Khiem Nguyen and Marc-André Keip. “A data-driven approach to nonlinear elasticity”. In: *Computers & Structures* 194 (2018), pp. 97–115.

[90] Lu Trong Khiem Nguyen, Matthias Rambausek, and Marc-André Keip. “Variational framework for distance-minimizing method in data-driven computational mechanics”. In: *Computer Methods in Applied Mechanics and Engineering* 365 (2020), p. 112898. DOI: 10.1016/j.cma.2020.112898.

[91] John Frederick Nye et al. *Physical properties of crystals: their representation by tensors and matrices*. Oxford university press, 1985.

[92] Stefanos-Aldo Papanicolopulos. “Computation of moderate-degree fully-symmetric cubature rules on the triangle using symmetric polynomials and algebraic solving”. In: *Computers & Mathematics with Applications* 69.7 (2015), pp. 650–666. DOI: 10.1016/j.camwa.2015.02.014.

[93] Clemens Pechstein and Bert Jüttler. “Monotonicity-preserving interproximation of B-H-curves”. In: *Journal of Computational and Applied Mathematics* 196.1 (2006), pp. 45–57. DOI: 10.1016/j.cam.2005.08.021.

[94] James Penman and J. Fraser. “Dual and complementary energy methods in electromagnetism”. In: *IEEE Transactions on Magnetics* 19.6 (1983), pp. 2311–2316.

[95] James Penman and J. Fraser. “Error bounded formulations in electromagnetism”. In: *Industrial Electromagnetics Modelling: Proceedings of the POLYMODEL 6, the Sixth Annual Conference of the North East Polytechnics Mathematical Modelling and Computer Simulation Group, held at the Moat House Hotel, Newcastle upon Tyne, May 1983*. Springer. 1983, pp. 53–62.

[96] Ilaria Perugia. “A mixed formulation for 3D magnetostatic problems: theoretical analysis and face-edge finite element approximation”. In: *Numerische mathematik* 84 (1999), pp. 305–326.

[97] Auriane Platzer et al. “Finite element solver for data-driven finite strain elasticity”. In: *Computer Methods in Applied Mechanics and Engineering* 379 (2021), p. 113756.

[98] Erik Prume, Stefanie Reese, and Michael Ortiz. “Model-free Data-Driven inference in computational mechanics”. In: *Computer Methods in Applied Mechanics and Engineering* 403 (2023), p. 115704.

[99] Rindra Ramarotafika, Abdelkader Benabou, and Stéphane Clenet. “Stochastic modeling of soft magnetic properties of electrical steels: Application to stators of electrical machines”. In: *IEEE Transactions on Magnetics* 48.10 (2012), pp. 2573–2584.

[100] Rindra Ramarotafika, Abdelkader Benabou, and Stéphane Clenet. “Stochastic modeling of anhysteretic magnetic curve using random inter-dependant coefficients”. In: *International Journal of Applied Electromagnetics and Mechanics* 43.1-2 (2013), pp. 151–159.

[101] Stefan Reitzinger, Barbara Kaltenbacher, and Manfred Kaltenbacher. “A note on the approximation of BH curves for nonlinear computations”. In: *Technical SFB-Report, Johannes Kepler Universitat Linz, Austria* (2002).

[102] Zhuoxiang Ren and Nathan Ida. “Influence of the RHS on the convergence behaviour of the curl-curl equation”. In: *IEEE Transactions on Magnetics* 32.3 (1996), pp. 655–658.

[103] Zhuoxiang Ren and Nathan Ida. “Derivation of various dual formulations in magnetostatics via error based energy approach”. In: *IEEE transactions on magnetics* 35.3 (1999), pp. 1167–1170. DOI: 10.1109/20.767156.

[104] Ja'far A.H. Rikabi, Clive F. Bryant, and Ernest M. Freeman. "An error-based approach to complementary formulations of static field solutions". In: *International Journal for Numerical Methods in Engineering* 26.9 (1988), pp. 1963–1987. DOI: 10.1002/nme.1620260906.

[105] Filip Rindler. *Calculus of variations*. Springer, 2018.

[106] Hossein Salahshoor and Michael Ortiz. "Model-free Data-Driven viscoelasticity in the frequency domain". In: *Computer Methods in Applied Mechanics and Engineering* 403 (2023), p. 115657.

[107] Hans Vande Sande et al. "Simulation of a three-phase transformer using an improved anisotropy model". In: *IEEE Transactions on Magnetics* 40.2 (2004), pp. 850–855.

[108] Thomas Schrefl et al. "Numerical methods in micromagnetics (finite element method)". In: *Handbook of magnetism and advanced magnetic materials* (2007).

[109] Gholamhossein H. Shirkoohi and M. A. M. Arikat. "Anisotropic properties of high permeability grain-oriented 3.25% Si-Fe electrical steel". In: *IEEE transactions on magnetics* 30.2 (1994), pp. 928–930.

[110] Laurent Stainier, Adrien Leygue, and Michael Ortiz. "Model-free data-driven methods in mechanics: material data identification and solvers". In: *Computational Mechanics* 64.2 (2019), pp. 381–393.

[111] Enzo Tonti. *The mathematical structure of classical and relativistic physics*. Vol. 10. Springer, 2013.

[112] Jeffrey K. Uhlmann. "Satisfying general proximity / similarity queries with metric trees". In: *Information Processing Letters* 40.4 (1991), pp. 175–179. DOI: 10.1016/0020-0190(91)90074-R.

[113] Tanja Van Mourik, Michael Bühl, and Marie-Pierre Gaigeot. *Density functional theory across chemistry, physics and biology*. 2014.

[114] Dries Vanoost et al. "Magnetic hysteresis at the domain scale of a multi-scale material model for magneto-elastic behaviour". In: *Journal of Magnetism and Magnetic Materials* 414 (2016), pp. 168–179.

[115] Arun S. Veeramani, John H. Crews, and Gregory D. Buckner. "Hysteretic recurrent neural networks: a tool for modeling hysteretic materials and systems". In: *Smart Materials and Structures* 18 (2009), 075004 (15pp). DOI: 10.1088/0964-1726/18/7/075004.

[116] Manuel Vogel. “Handbook of accelerator physics and engineering, by A.W. Chao, K.H. Mess, M. Tigner and F. Zimmermann”. In: *Contemporary Physics* 57.2 (2016), pp. 263–263. DOI: 10.1080/00107514.2015.1133708.

[117] Yan Wang and David L McDowell. “Uncertainty quantification in materials modeling”. In: *Uncertainty Quantification in Multiscale Materials Modeling*. Elsevier, 2020, pp. 1–40.

[118] Sacha Wattel et al. “Mesh d-refinement: a data-based computational framework to account for complex material response”. In: *Mechanics of Materials* 180 (2023), p. 104630.

[119] David M. Williams, Lee P. Shunn, and Antony Jameson. “Symmetric quadrature rules for simplexes based on sphere close packed lattice arrangements”. In: *Journal of Computational and Applied Mathematics* 266 (2014), pp. 18–38. DOI: 10.1016/j.cam.2014.01.007.

[120] Zdzisław Włodarski. “Analytical description of magnetization curves”. In: *Physica B: Condensed Matter* 373.2 (2006), pp. 323–327. DOI: 10.1016/j.physb.2005.12.242.

[121] Zhaosuo Xia, Yonglin Kang, and Quanli Wang. “Developments in the production of grain-oriented electrical steel”. In: *Journal of Magnetism and Magnetic Materials* 320.23 (2008), pp. 3229–3233.

Acknowledgements

For the support during my doctoral phase and the writing of this thesis, I would like to express my sincere gratitude to:

- Prof. Dr.-Ing. Herbert De Gersem for the opportunity to work at the Institute for Accelerator Science and Electromagnetic Fields (TEMF) as a doctoral student, the supervision of my research activities, and always being willing to lend an ear to my ideas and questions.
- Dr.-Ing. Dimitrios Loukrezis for his mentorship, excellent supervision even during challenging times such as the COVID-19 pandemic, enriching scientific and non-scientific discussions, and lastly, for sharing intense and laid-back music.
- Prof. Dr.-Ing. Ulrich Römer for the scientific discussions and collaboration during my internship at TU Braunschweig, as well as for providing a comfortable and familiar environment. Moreover, I am grateful for his guidance during my Bachelor's studies and for raising my interest in numerical methods and uncertainty quantification in the first place.
- Moritz von Tresckow and Dr. Ion Gabriel Ion for being great office mates, always willing to engage in scientific discussions and share a good laugh. Additionally, I am grateful to Moritz von Tresckow for, respectively, diligently proofreading of this thesis and providing valuable critical comments, respectively, pointing out mistakes.
- Heike Koch and Achim Wagner for their valuable assistance and help with organizational issues.
- My current and former colleagues at TEMF, for providing such a comfortable working environment, for the (virtual) discussions in the coffee kitchen, the jokes, the hikes in Kleinwalsertal, and in general for the great company over the past years.
- All my friends, for their support and sometimes necessary distraction.

- My mother, Bernadette, my sister, Christina, my two brothers, Wolfgang and Manfred, for their support and encouragement. In particular, I would like to thank Wolfgang for patiently listening to my scientific problems and providing mathematical support.

Finally, I am very grateful to my wife Désirée for her unwavering support, watching my back in tough times, encouraging words and unconditional love. Additionally, I feel so thankful for my son Clemens, whose good mood and uplifting nature has always brought me joy.

This work has been supported by the DFG, Research Training Group 2128 "Accelerator Science and Technology for Energy Recovery Linacs".